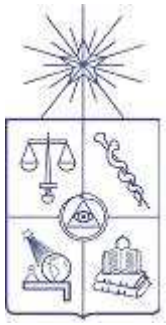

UNIVERSIDAD DE CHILE
FACULTAD DE CIENCAS FÍSICAS Y MATEMÁTICAS
DEPARTAMENTO DE INGENIERÍA CIVIL

INTERNAL DYNAMICS OF GRAVITATIONAL DENSE GRANULAR FLOWS. EXPERIMENTAL STUDY AND NUMERICAL MODELING.

TESIS PARA OPTAR AL GRADO DE DOCTOR EN
CIENCIAS DE LA INGENIERÍA
MENCIÓN FLUIDODINÁMICA

SANTIAGO RAFAEL MONTSERRAT MICHELINI

PROFESOR GUIA:
ALDO TAMBURRINO TAVANTZIS

MIEMBROS DE LA COMISIÓN:
YARKO NIÑO CAMPOS
OLIVIER ROCHE
BRIAN MCARDELL
PATRICIO CORDERO SIMUNOVIC

SANTIAGO DE CHILE
JULIO 2012

RESUMEN DE TESIS
PARA OPTAR AL GRADO DE DOCTOR EN
CIENCIAS DE LA INGENIERÍA
MENCIÓN FLUIDODINÁMICA
POR. SANTIAGO MONTSERRAT MICHELINI
FECHA: 20 DE JULIO DE 2012
PROF. GUIA: ALDO TAMBURRINO

El estudio de flujos granulares resulta importante en distintas aplicaciones industriales, como también para lograr una mejor comprensión de fenómenos naturales. Los flujos granulares que ocurren en la naturaleza muchas veces presentan un gran poder destructivo. Por ello, la predicción de la ocurrencia y comportamiento de éstos a escalas geofísicas resulta de gran interés para el ordenamiento territorial y evaluación del riesgo en asentamientos humanos y numerosas faenas industriales. Ejemplos de flujos granulares a escalas geofísicas son: flujos detríticos (aluviones), flujos piroclásticos, avalanchas de nieve y avalanchas de roca. Esta tesis está estructurada en base a una serie de artículos de investigación originales autocontenidos en la que se aborda el estudio de la dinámica interna de flujos granulares densos. En el presente trabajo se presenta una serie de resultados experimentales sobre flujos granulares compuestos por mezclas aire-partículas, con diferentes grados de fluidización inicial, inducidos sobre un canal rectangular (experimentos tipo "rompimiento de presa"). También se presentan resultados experimentales y numéricos respecto del proceso de defluidización de mezclas aire-partículas en columnas estáticas. Los resultados obtenidos aportan nuevos conocimientos respecto de la física de los flujos granulares densos. Diversos estudios coinciden en que el fluido intersticial, incluso cuando es aire, resulta de gran importancia en la dinámica de los flujos granulares. Las partículas utilizadas en el estudio experimental pertenecen al grupo A según la clasificación del Geldart. Ensayos experimentales han mostrado que mezclas de partículas obtenidas en depósitos de flujos piroclásticos ricos en cenizas presentan un comportamiento del tipo A cuando son sometidas a fluidización por gas. Por ello, los resultados obtenidos en este trabajo tienen especial relevancia para entender la mecánica de flujos piroclásticos densos ricos en cenizas. Además, comportamientos similares a los esperados en mezclas aire-partículas del tipo A han sido observados en mezclas detríticas (agua-partículas) durante procesos de defluidización producto de la autoconsolidación de las mezclas debido a su propio peso. Para llevar acabo esta tesis, en primer lugar se realizaron experimentos tipo rompimiento de presa de mezclas granulares fluidizadas en distintas proporciones. Los resultados obtenidos fueron comparados con flujos derivados de mezclas no fluidizadas y flujos de agua pura, todos ensayados en la misma instalación experimental. La evolución espaciotemporal de la presión de poros en el fondo de los flujos granulares generados y a lo largo del canal experimental fue estudiada mediante un segundo conjunto de experimentos. Técnicas de análisis de imágenes de video permitieron correlacionar la estructura observada del flujo con las señales de presión obtenidas. En particular, con imágenes de video obtenidas a lo largo del canal se estudió los patrones de depositación del flujo. Nuevos experimentos, consistentes en medir la evolución de la presión de poros en mezclas estáticas (columnas) previamente fluidizadas, permitieron estudiar los mecanismos que controlan la difusión de la presión de poros en éstas. Este estudio fue complementado con un modelo numérico capaz de representar de buena forma los resultados experimentales obtenidos. A pesar de que en flujos granulares la difusión de la presión de poros puede ser controlada por otros procesos más complejos que aquellos presentes en el caso estático, este simple experimento aporta nuevas ideas respecto al proceso de difusión de la presión de poros en mezclas inicialmente fluidizadas. Finalmente, se estudió experimentalmente el alcance de los flujos granulares, para todo el rango de fluidización (desde nula a completamente fluidizado) en canales con distintas pendientes. En resumen, nuestros resultados enfatizan la capacidad de la presión de poros en aumentar la movilidad de mezclas fluido-partículas. El incremento en las escalas de tiempo de difusión de la presión de poros debido a la consolidación de mezclas fluidizadas y expandidas causan un notable incremento en el alcance de los flujos, cuando se comparan con mezclas no fluidizadas y no expandidas.

Abstract

Granular flows are a commonly found in nature and are important to many industrial applications. Some natural granular flows, including debris flows, pyroclastic flows, snow avalanches and rock avalanches may be extremely hazardous. Predicting their occurrence and behavior at geophysical scales is crucial for land-use management and risk assessment in human settlements as well as many industrial operations. This thesis, consisting of a series of self-contained research articles, is devoted to study the internal dynamics of gravitational dense granular flows. The present work compiled results of a series of dam-break experiments of initially fluidized granular mixtures at different degrees, as well as experiments and numerical modeling of the pore pressure diffusion process in static fluidized columns. Numerous studies have shown that the interstitial fluid, even when it is air, plays an important role in granular flows dynamics. For the experiments, we used air-particles mixtures, with particles belonging to group A according to Geldart's classification that describes the behavior of gas particle fluidization. Group A-type behavior has been experimentally observed for ash-rich pyroclastic flows deposits, and thus our results have direct implications on the understanding of the mechanics of such flows. First, we performed dam-break type experiments of initially fluidized granular mixtures at different degrees, and compared the obtained results with those of non-fluidized and water flows. To this purpose, a variable-slope experimental flume was designed and constructed as part of the present research work. In a second set of experiments, the pore pressure time-evolution at the bottom of dam-break induced granular flows along the experimental flume was studied. In addition, analyses of high-speed videos allowed for the correlation of the pressure signal with the flow structure. In particular, granular flows deposition patterns were analyzed using video imaging techniques. The mechanism controlling pore pressure diffusion was then studied in static fluidized granular columns by means of experiments and numerical modeling. Although pore pressure diffusion in sheared flows is governed by local particle-particle and particle-fluid interactions, whose mechanics are inherently complex compared to the static case, despite their simplicity, our experiments bring insights regarding pore fluid pressure diffusion in a wide range of fluidization conditions. Finally, experimental results of flow run-outs, over the whole range of fluidization degrees (from none to complete fluidization) and different flume slopes, were obtained. These final results properly linked the observed flow run-outs with our previous observations regarding flow behavior and pore pressure diffusion due to changes in the initial degree of fluidization. In summary, our results highlight the ability of pore fluid pressure in contributing to granular flows mobility, showing long-lived high pore fluid pressure during most of the flow emplacements. Complex behavior during mixture consolidation of initially expanded columns increases pore pressure diffusion time scales, causing significantly larger run-outs when compared with non-expanded mixtures.

Acknowledgements

I would like to thank my advisor and co-advisor, Aldo Tamburrino and Yarko Niño, for their valuable guidance, support and constant encouragement in this long process. Thanks to Olivier Roche for his tutelage and guidance, especially during my stay in his laboratory in Clermont-Ferrand, where most of my experiments were done. I would like to extend my acknowledgment to people from Laboratoire Magmas et Volcans, Université Blaise Pascal, for their hospitality. Thanks to Brian McArdell for receiving me in the Swiss federal research institute, WSL. Thanks for your hospitality and for showing me real debris flows in the field. I would also like to thank people from the WSL – SLF, especially Christoph Graf and Perry Bartelt.

I gratefully acknowledge the financial support from Mecesup UCH 310 8 (PhD fellowship), Departamento de Postgrado y Postítulo de la Vicerrectoría de Asuntos Académicos, Universidad de Chile (Foreign residence fellowship), ECOS-CONICYT Projects C06U01 and C11U01, Departamento de Ingeniería Civil, Universidad de Chile, Advanced Mining Technology Center (AMTC), Laboratoire Magmas et Volcans, Unversite Blaise Pascal, and Swiss Federal Research Institute, WSL.

Quiero agradecer a todas las personas de la División de Recursos Hídricos y Medio Ambiente que de alguna u otra forma hicieron posible este trabajo de tesis. En particular quiero agradecer a Jessica Valenzuela, Manuel Cáceres, Juan Donoso y Geovani Arredondo. También Quiero agradecer a mis compañeros y amigos con quienes compartí durante mi paso por el programa: Cristián Godoy, Carlos Reiher, Wernher Brevis, Sergio Quijada, Javier González, Alexandra Cuellar y Eduardo Rubio. Gracias a James McPhee por la oportunidad de trabajar con él durante estos últimos años y así explorar nuevas áreas de desarrollo. En forma especial quiero agradecer a Christian Ihle por todo el apoyo y ayuda brindada en la última etapa de este trabajo. Gracias a mis padres y hermanos por su compañía, apoyo y paciencia.

Muchas gracias Negrita por el apoyo, paciencia y amor que me entregaste durante este periodo. Muchas gracias también por la ayuda en el trabajo experimental que juntos realizamos en Francia. Y muchas gracias por nuestras hijas. A ustedes va dedicado este largo trabajo.

Contents

Chapter 1

1 Introduction

After water, granular matter is the second-most manipulated material in industry [Richard *et al.* 2005] and is ubiquitous in nature. In particular, the ability to predict the occurrence and behavior of granular flows at geophysical scale is crucial for land-use management and risk assessment in human settlements and numerous industrials operations. Geophysical granular flows consist of solid-fluid mixtures driven by gravity in natural sloping terrains. The solid phase is comprised by soils of different sizes available in the catchments, while the fluid phase can be water, gas or a mixture of both. Also, the mixture of water with fine soils can act as an equivalent fluid changing reological properties with respect to that of pure water [*Iverson*, 1997; *Major*, 2000; *Ancey & Jorrot* 2001]. Examples of geophysical granular flows are debris flows, pyroclastic flows, snow avalanches and rock avalanches [*Iverson,* 1997; *Freundt et al.,* 2000; *Iverson and Denlinger*, 2001; *Jain et al.*, 2004].

Although important advances have been made in the topic, to predict the behavior of geophysical granular flows still remain a challenging issue. In a seminal contribution, *Bagnold* [1954] introduced the concept of dispersive stress, which accounts for the stress generated by inter-particle collisions. In his experiments, *Bagnold* neglected inter-particle friction and buoyancy effects as he used neutrally buoyant particles. For diluted and strongly agitated flows, inter-particle collisions dominate over the energy dissipation due to friction. In this case, constitutive relations derived from the kinetic theory of gases have provided good results [*Campbell*, 1990; *Azanza* et al., 1999; *Goldhirsch*, 2003]. On the other hand, in dense particle mixtures subject to slight shear deformation, particles maintain long-lasting contacts, thus dissipating energy by inter-particle friction. In this, so-called "quasi-static" regime, constitutive laws are derived from soil-mechanics considerations, mainly through Coulomb plasticity models. The Coulomb law has provided good results representing the energy dissipation by inter-particle friction in this type of granular flows [*Ancey*, 2006; *Iverson*, 1997, *Savage and Hutter*, 1989; *Iverson and Denlinger*, 2001; *Iverson et al*., 2004; *Pudasaini et al*., 2005]. In most natural granular flows, as well as in industrial applications, these two limiting regimes coexist [*Ancey and Evesque*, 2000; *Armanini et al*., 2005; *Ancey*, 2006]. Two-dimensional numerical simulations of sheared granular layers have shown the existence of force chains, formed by long-lasting contact networks (frictional forces), which transmit most of the stress within the flow [*Aharonov and Sparks*, 1999]. In particular, chute flows featuring vertical rheological stratifications have been experimentally observed by *Armanini et al*., [2005, 2008], where distinct sub-layers have been identified to dip into either frictional or collisional regimes.

It has been shown not only grains, but also the interstitial fluid plays an important role in bulk flow dynamics, even when the fluid-phase is air [*Major*, 2000; *Roche et al*., 2004, 2008, 2010; *Druitt*; *Iverson*, 1997; *Iverson and Denlinger*, 2001; *Goren et al*., 2010], where viscous stresses associated to the fluid phase contributes to the total stress of the granular flow. Fluid flow

stress are commonly modeled following Bingham or Herschel-Buckley type rheologies, depending on the nature of the effective fluid phase, as fine particles affect rheologies in comparison to pure fluids [*Einstein*, 1906; *Krieger & Dougherty*, 1959; *Iverson*, 1997; *Naef et al*., 2006; *Iverson et al*., 2010]. Furthermore, the interstitial fluid reduces inter-particle friction following to the Terzaghi effective-stress principle [*Iverson*, 1997; *Iverson and Denlinger*, 2001; *Savage and Iverson*, 2003; *Goren et al*., 2010, *Iverson et al*., 2010]. Excess pore fluid pressure (with respect to hydrostatic), high enough to maintain mixtures fluidized, has been measured at the bottom of natural and experimental granular flows [Iverson, 1997; *Major and Iverson*, 1999; *McArdell et al*., 2007; *Iverson et al*., 2010], supporting the idea that pore fluid pressure can be long-lived, thus explaining their unusual mobility even in low slope terrains. A rapid rise in pore pressure, high enough to liquefy debris flow mixtures, has been experimentally observed at the onset of flow initiation [*Iverson et al.*, 2000]. For the flow following the liquefaction of mixtures, many authors hypothesize that pore fluid pressure diffuses and vary owing to particles rearrangement (contractive - dilative particles motion) [*Iverson et al*., 1989; *Iverson*, 1997, *Iverson and Denlinger*, 2001; *Gubet and Mudd*, 2005; *Goren et al*., 2010]. Although pore fluid pressure variation due to particles contractive - dilative motion has been observed both, experimentally and in numerical models [*Iverson et al*., 1989; *Goren et al*., 2010], the origin of the long-lasting excess of pore fluid pressure, sustaining a high degree of fluidization far away from flow initiation, is still poorly understood.

The objective of this thesis work is to study the main features of initially fluidized granular flows, including run-out, flow velocity, deposition characteristics, flow height, basal pore fluid pressure and degree of fluidization. A series of dam-break type experiments in initially fluidized air-particle mixture flows reveals distinct flow behaviors depending on the initial degree of fluidization. In the experiments, glass beads of grain size ranging from 60 to 90 μm and density of 2500 kg/m³ were used (Ballotini, Potters Industries). These particles belong to group A following *Geldart's* [1973] classification that describes the behavior of gas particle fluidization. Different degrees of fluidization were introduced by varying the vertical air flux at the bottom of the column. Fluidization occurs for a certain air velocity, typically known as the minimum fluidization velocity, *Umf*. For air velocities grater than *Umf*, the mixture linearly expands until bubbles appear at a second critical velocity known as the minimum fluidization velocity, *Umb*. In practice, fluidization may not be fully homogeneous throughout the granular column, due to the presence of some degree of airflow channeling. Thus, bed expansion normally occurs before complete fluidization is achieved [*Gilbertson et al*., 2008]. This behavior is observed in many industrial materials and, in a geophysical context, in ash-rich pyroclastic flow deposits [*Druitt et al*., 2007

Dam-break experiments where conducted on a 300 cm long, 20 cm wide flume, with a head reservoir of variable length (5 cm - 20 cm) and 20 cm wide, where particles were fluidized. Flows were generated by the sudden release of a gate (< 0.01 s) separating the reservoir with the flume. The flume can be tilted at different slopes. The reservoir maintains always horizontal due to fluidization purpose. A detailed description of the experimental set-up appears in Figure 3.1 [Roche et al., 2010].

The present document is the compilation of a series of related research papers. The first of them (Chapter 2) compares the behavior of fluidized granular flows with water flows, using an experimental flume designed to meet the required parameter range. Results show a water-like behavior of little expanded fluidized granular flows for most of their emplacement. Basal pore fluid pressure measurements along the flow are investigated in Chapter 3, showing long-lived pore fluid pressure in the body of little expanded fluidized flows for most of their emplacement. In Chapter 4, a detailed analysis of pore pressure diffusion in static columns is performed. Marked differences in the pore pressure diffusion process are observed between initially expanded and not expanded mixtures. Finally, Chapter 5 shows that flow run-out mainly depends in the initial degree of fluidization. In addition, an important increase in the flow run-out is observed for fluidization degrees above the onset of bed expansion, coinciding with the changes in pore pressure diffusion observed in Chapter 4.

Chapter 2

2 Experimental observations of water-like behavior of initially fluidized, dam break granular flows and their relevance for the propagation of ash-rich pyroclastic flows.

This chapter corresponds to the paper authored by Olivier Roche, Santiago Montserrat, Yarko Niño and Aldo Tamburrino, published in *Journal of Geophysical Research*, volume 113 (2008), B12203, 15 pp.

Abstract

The physics of ash-rich pyroclastic flows were investigated through laboratory dam-break experiments using both granular material and water. Flows of glass beads of 60-90 µm in diameter generated from the release of initially fluidized, slightly expanded (2.5-4.5%) columns behave as their inertial water counterparts for most of their emplacement. For a range of initial column height to length ratios of 0.5-3, both types of flows propagate in three stages, controlled by the timescale of column free fall $\sim(h_0/g)^{1/2}$, where h_0 denotes column height and g gravitational acceleration. Flows first accelerate as the column collapses. Transition to a second, constant velocity phase occurs at a time $t/(h_0/g)^{1/2}\sim1.5$. The flow velocity is then $U\sim\sqrt{2}(gh_0)^{1/2}$, larger than that for dry (non-initially fluidized) granular flows. Transition to a last, third phase occurs at $t/(h_0/g)^{1/2}\sim4$. Granular flow behavior then departs from that of water flows as the former steadily decelerate and the front position varies as $t^{1/3}$, as in dry flows. Motion ceases at $t/(h_0/g)^{1/2}\sim6.5$ with normalized run-out $x/h_0\sim5.5$-6. The equivalent behavior of water and highly concentrated granular flows up to the end of the second phase indicates a similar overall bulk resistance, although mechanisms of energy dissipation in both cases would be different. Interstitial air-particle viscous interactions can be dominant and generate pore-fluid pressure sufficient to confer a fluid-inertial behavior to the dense granular flows before they enter a granular-frictional regime at late stages. Efficient gas-particle interactions in dense, ash-rich pyroclastic flows may promote a water-like behavior during most of their propagation.

Keywords: Pyroclastic flows, Granular flows, Open channel hydraulics, Dam break, Fluidization, Avalanche.

2.1 Introduction

Geophysical granular flows commonly occur in various environments and prediction of their behavior is crucial for hazard assessment. Pyroclastic density currents represent major threats for populations and infrastructure [*Druitt*, 1998; *Freundt and Bursik*, 1998; *Branney and Kokelaar*, 2002]. They are commonly generated during volcanic eruptions by the collapse of lava domes [*Cole et al.*, 2002] or explosive eruption columns [*Sparks and Wilson*, 1976], as well as by sedimentation of dilute ash clouds when these interact with topography [*Druitt et al.*, 2002] (Figure 2.1). These density currents consist of hot mixtures of particles and volcanic gas, and can propagate from their vent over distances of several kilometers on very gentle slopes. Analyses of the characteristics of their deposits led to the identification of two end-member conceptual models, possibly delimiting a continuum, as the parent currents are thought to be dilute, turbulent pyroclastic surges [e.g., *Fisher*, 1966; *Branney and Kokelaar*, 1992] or dense granular flows [e.g., *Sparks*, 1976; *Wilson*, 1986]. Our study focuses on dense flows, being in most cases a rapidly moving basal dense granular avalanche overridden by a dilute ash cloud [*Denlinger*, 1987; *Fisher*, 1995].

Information on the processes governing pyroclastic flows can be obtained from extensive works on the physics of granular flows. However, despite intensive research, the fundamental mechanisms of these flows are still controversial and the nature of the constitutive equations represents a matter of debate, particularly when interstitial fluid effects can become important [*GDR MiDi*, 2004; *Forterre and Pouliquen*, 2008]. Dense flows with particle concentrations close to maximum packing of the static material have been the focus of several studies, as summarized for instance by *GDR MiDi* [2004]. Inertia is recognized as important within those flows, but more important are interparticle collisional and frictional contacts that resist motion and dissipate energy. Seminal experimental and theoretical works commonly considered the steady regime on inclines at angles close to the angle of repose (~30°) of the granular material. The analysis assumes a frictional rate-independent Coulomb-type friction law [*Savage*, 1984; *Savage and Hutter*, 1989] or that energy dissipation results from both frictional and collisional contacts [*Johnson and Jackson*, 1987; *Johnson et al.*, 1990]. Later works revealed a complex form of energy dissipation, as friction is depth-dependant [*Pouliquen*, 1999] and flow rheology is of visco-plastic nature characterized by a yield shear stress and a complex dependence on shear rate [*Jop et al.*, 2006; *Forterre and Pouliquen*, 2008].

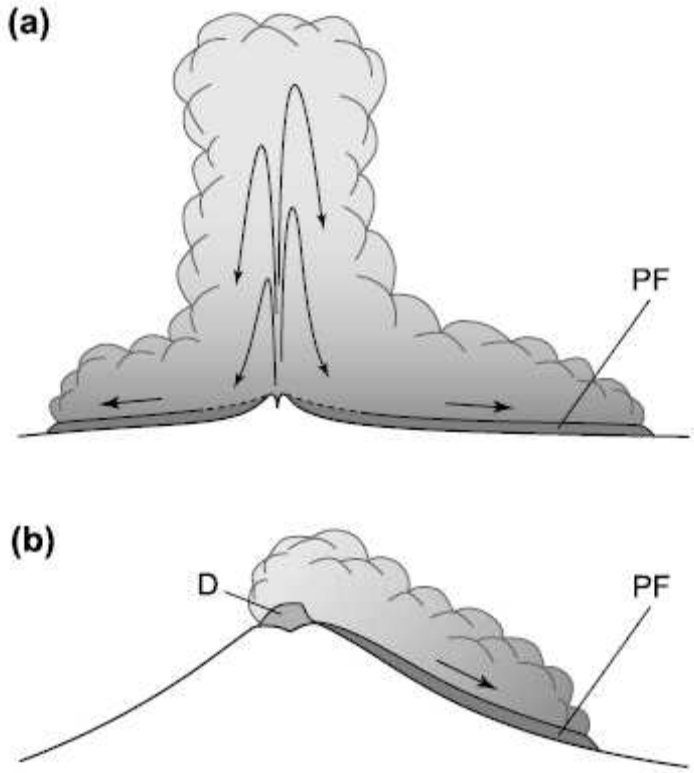

Figure 2.1. Schematic representation of pyroclastic flows generation mechanisms. Gravitational collapse of (a) a large eruptive column, and (b) a lava dome. *PF* and *D* denote pyroclastic flow and dome, respectively.

Prediction of the behavior of pyroclastic flows can be achieved through analytical and numerical simulations provided the physics and derived constitutive relationship for flow motion are known, and this represents a challenging issue. Insights into the general flow behavior are obtained from analytical calculations [*Denlinger*, 1987; *Beget and Limke*, 1988; *Levine and Kieffer*, 1991], and accurate mode of emplacement can be investigated from numerical simulations. As for other types of geophysical flows, the aim of the numerical simulations is to solve the equations of conservation of mass and momentum introducing a closure for the resistance of the flow. Pyroclastic flows have been the focus of several studies based on more or less sophisticated methods, including kinetic [*McEwen and Malin*, 1989; *Saucedo et al.*, 2005; *Wadge et al.*, 1998], depth-average [*Sheridan et al.*, 2005; *Kelfoun et al.*, 2007; *Mangeney et al.*, 2007], and multiphase [*Valentine and Wohletz*, 1989; *Neri et al.*, 2007] approaches. One of the major limitations of these models is the nature of the resistance stress, which is assumed to be either frictional Coulomb-type or constant, viscous (proportional to the flow velocity, U), inertial-turbulent (proportional to U^2), or a combination of these (see for instance the related analysis for two-phase flows by *Ancey* [2007]).

In pyroclastic flows, fluidization of the granular mass by an upward flow of gases of internal sources or air ingested is assumed to be a major mechanism that controls the dynamics of emplacement and adds complexity to their understanding [*Sparks*, 1978; *Wilson*; 1980, 1984; *Druitt et al.*, 2007]. For instance, experimental studies on continuously fluidized flows on an inclined or horizontal substrate, for which basal and internal friction are considerably reduced,

revealed that the internal velocity profiles and segregation processes can be different from those of non-fluidized cases [*Ishida et al.*, 1980; *Takahashi and Tsujimoto*, 2000; *Eames and Gilbertson*, 2000]. The aim of the present experimental study was to investigate unsteady granular flows generated from the quasi-instantaneous release of a static gas-fluidized column. No subsequent source of gas is provided during flow emplacement. The purpose of initial fluidization of the granular column is to weaken the contact forces in the particles' chain network in order to investigate how this imposed initial condition influences the subsequent flow dynamics. This extends earlier works by *Roche et al.* [2002, 2004, 2005], which revealed that initially fluidized granular flows share some similarity with buoyancy-driven gravity currents of pure Newtonian fluid. Similar experiments were also carried out recently by *Girolami et al.* [2008] with pyroclastic material. The reader may refer to *Fan and Zhu* [1998] and *Rhodes* [1998] for the fundamentals of gas fluidization, and to *Wilson* [1980, 1984], and *Druitt et al.* [2007] for aspects more specific to pyroclastic materials.

In the present study, we carried out dam-break type experiments with granular material and investigated a range of different initial column aspect ratios in a rectangular reservoir, as considered in experiments with flows in which the interstitial fluid has no effect [*Balmforth and Kerswell*, 2005; *Lajeunesse et al.*, 2005; *Lube et al.*, 2005]. In order to determine to what extent the behavior of a dense granular flow, initially fluidized or not, is comparable to that of a pure fluid under dam-break conditions, we also carried out experiments using water in the same flume. For this, we studied the flow kinematics quantitatively using appropriate time and length scales. Our results reveal that the interstitial air within dense granular flows can have a fundamental influence as these behave like their water counterparts for most of their emplacement. This is what we mean by *water-like* behavior throughout this paper.

2.2 Principles of dam-breaking

We investigated unsteady flows of dense granular matter based on the dam-break concept, which is a classical issue in the context of engineering applications dealing with catastrophic flows of water or mixtures of water and particles [*Chow*, 1959; *Graf and Altinakar*, 2000]. The seminal analysis by *Ritter* [1892] considers a 2D open channel flow, propagating on a horizontal surface, generated from the quasi-instantaneous release of a material initially at rest in a reservoir of height h_0, which is considered as semi-infinite (Figure 2.2). Ritter's depth-averaged analysis neglects frictional and turbulent resistive effects, and assumes hydrostatic pressure conditions and negligible vertical acceleration. The flow depth is predicted to decrease monotonically as the consequence of the formation of two waves, one retreating backwards in the reservoir at a speed $U=(gh_0)^{1/2}$, and the second propagating into the channel at a higher speed $U=2(gh_0)^{1/2}$. Since this earlier work, the dam-break issue has received much attention, and subsequent studies developed more sophisticated analyses and particularly addressed flow resistance by introducing a hydraulic resistance term [*Dressler*, 1954; *Whitham*, 1955]. Following these classical approaches, experiments on dam-break flows of water commonly dealt with reservoirs having a height much smaller than their length [*Dressler*, 1954; *Bell et al.*, 1992; *Lauber and Hager*, 1998; *Jánosi et al., 2004*; *Leal et al.*, 2006]. *Leal et al*. [2006], in particular, reviewed several experimental studies that reveal that water flows propagate into the channel at a speed of $U\sim\sqrt{2}(gh_0)^{1/2}$, lower than that predicted by *Ritter* [1892]. Recently, *Hogg and Woods* [2001] and *Hogg and Pritchard* [2004] presented theoretical analyses of the dam-break problem, specifically addressing flow

resistance in these unsteady flows and providing reasonable interpretation of experimental observations. This is further discussed in Section 5.1 in connection with our experimental results.

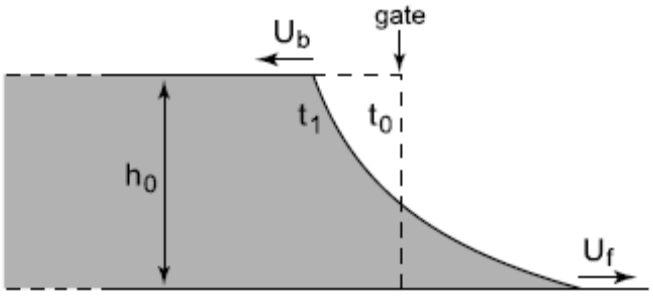

Figure 2.2. The concept of dam-breaking [*Ritter*, 1892]. The case of an ideal frictionless fluid propagating on a dry substrate is shown, before (t_0) and after (t_1) opening of the sluice gate. Two waves propagate, one forward in the channel at speed $U_f=2(gh_0)^{1/2}$ and the second backwards in the reservoir at $U_b=(gh_0)^{1/2}$.

2.3 Experimental device and procedure

Dam-break experiments with granular matter or water were conducted in an experimental apparatus consisting of a reservoir and a horizontal channel separated by a vertical sluice gate (Figure 2.3). The apparatus is made of smooth Perspex plates. For experiments on granular flows, the reservoir is equipped with a basal porous plate through which air is introduced vertically from a wind-box to generate a fluidized granular column [*Roche et al.*, 2002]. Air is dried by means of filters and its flux is controlled by a series of manometers. The channel is 3 m long, and both the reservoir and channel have a width of 10 cm. Transparent lateral walls allow for video analysis of the emptying reservoir and propagation of the flow in the channel. The initial column height in the reservoir (h_0) and reservoir length (x_0) were varied so that h_0 is in the range from 10 to 40 cm and x_0 is in the range from 10 to 20 cm, and we considered aspect-ratios

$$r = \frac{h_0}{x_0} \tag{2.1}$$

of 0.5 to 3.

For granular flows, we used glass beads of grain size d in the range from 60 to 90 µm (d_{50}=75 µm) and density ρ_s=2500 kg m^{-3}, with a loose packing volume fraction c_0=0.58±0.02 so that the bulk density of a granular column is ρ_b=1450±50 kg m^{-3}. Before each experimental run, the particles were subjected to an intense flux of dry air in a fluidization rig in order to reduce as much as possible cohesion effects caused by ambient moisture. Then, particles were poured into the reservoir, and the granular column could be fluidized by means of a flux of dry air passing through the basal porous plate. As air ascends into the granular pile, the drag force generated counterbalances the weight of the grains, thus reducing substantially the intensity of the

interparticle contacts in the force-chain network. The particles used belong to group A of *Geldart*'s [1973] classification that describes the behavior of gas-particle fluidization. This means that particulate (homogeneous) fluidization is possible over a range of gas flow velocity, which is observed for many industrial materials but also for samples of ash-rich pyroclastic flow deposits [*Druitt et al.*, 2007]. The granular column was fluidized at the following velocities, defined as the mean flow rate divided by the cross sectional area of the reservoir, (1) the minimum fluidization velocity (U_{mf}=7.5 mm s^{-1}) at which the bed is fully supported and pore-fluid pressure is maximum, as the weight of the particles is balanced by the drag force caused by air motion, but the packing volume fraction is not modified, or (2) at a larger velocity (U_{mb}=1.6-1.7U_{mf}) just before gas bubbles form and at which the maximum expansion of the column in the present case is only e=2.5-4.5% [*Rhodes*, 1998]. It is important to note that no air flux is provided in the channel during flow propagation, so that the dynamics of emplacement is partially affected by the diffusion of the pore-fluid pressure generated in the initially fluidized granular column. For comparison, flows were also generated from granular columns with no air flux in the reservoir and these are called *dry* hereafter. For experiments with water, we used a reservoir with an impermeable base. Great care was taken to ensure that no filtration occurred at the sluice gate and that the channel was perfectly dry before release of the static liquid column. Flows of water always reached the open end of the channel and were collected in a tank. Water spread until surface tension forces dominate, thus leaving a thin liquid layer of about 2 mm. In order to facilitate video-analysis, water in the reservoir was dyed with natural pigments, and the rear part of both the reservoir and the channel was covered with tracing paper in order to provide uniform illumination when lighted from behind. Experiments were recorded at 30-90 frames s^{-1} and a mark adapted to the sluice gate allowed for accurate determination of the moment at which opening began. Videos were analyzed to determine kinematic parameters describing flow motion, such as the column height in the reservoir (h_c), the mean height of the flow in the channel (h_f), and the flow front position from the gate (x) (Figure 2.3). The mean flow height was estimated as the average height of the central third of the current for convenience. This provides a good estimate of the mean height of the entire flow as it is thicker near the gate and thins at the front in the same proportion. We did not detect significant wall effects on the flow height and it was rather constant in the cross section.

2.4 Experimental results

2.4.1 Characteristics of flow kinematics

Under the range of initial configurations, all types of granular flows formed a deposit whose longitudinal extent was lower than the channel length. Flow duration and run-out were respectively 0.66-1.28 s and 0.60-2.20 m for initial granular columns fluidized at U_{mb}, 0.56-1.04 s and 0.43-1.55 m for columns fluidized at U_{mf} , and 0.46-0.92 s and 0.23-1.01 m for *dry* columns. Flows of water and granular material resulting from fluidized columns have a very similar morphology for most of their emplacement (Figure 2.4). The drag exerted by the sluice gate when it is suddenly removed affects only a very thin layer of the column and has a negligible influence on the bulk flow behavior. Once the gate is open, flows are generated from the bottom of the column and material is evacuated from the reservoir. A surface dam-break wave propagates backwards in the reservoir at $r \leq 1.5$ as predicted by *Ritter*'s [1892] analysis. In contrast, the

column drops vertically with little deformation of the top at r>1.5 (Figure 2.5). Then, flows propagate at almost constant height for a while. This contrasts with *dry* flows that are generated from flank avalanches and propagate as wedges as described already [*Roche et al.*, 2002 and 2004; *Balmforth and Kerswell*, 2005; *Lajeunesse et al.*, 2005; *Lube et al.*, 2005]. Finally, flows spread into the channel, and granular flows finally come to halt whereas water flows continue past the channel end. Deposits of the granular flows resulting from fluidized columns have a horizontal upper surface in the reservoir, where the material thickness is slightly less than that at the entrance of the channel. Within the channel, their upper surface dips gently towards the front at an angle of about 1-2 degrees. This contrasts with deposits resulting from *dry* granular columns as the slope angle of their upper surface in the reservoir is close to the angle of repose of the material (~30°) and the thickness steadily decreases downstream.

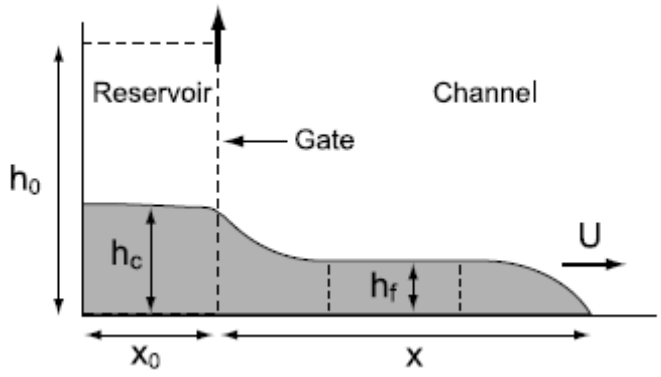

Figure 2.3. Sketch of the experimental device used for dam-break experiments with both granular matter and water. Material is released from the reservoir into the channel by means of a vertical sluice gate (vertical arrow). For granular flows, the initial column can be fluidized by means of an air flux introduced at the base of the reservoir through a porous plate. Initial conditions are the initial column height in the reservoir (h_0) and reservoir length (x_0). Kinematic parameters are the collapsing column height in the reservoir (h_c), the mean height of the flow in the channel estimated as the average height of the central third (h_f), the flow front position from the gate (x), and the flow front velocity (U).

Flows emplace in three distinct stages, and *dry* flows depart significantly from the others (Figure 2.6). During the first, collapse phase, flows generated from granular columns fluidized at U_{mf} or U_{mb} and from water columns steadily accelerate at low h_0 (≤ 20 cm) or enter almost immediately into a first constant velocity phase at high h_0 (>20 cm). The flow height in the channel steadily increases while the column height decreases as the reservoir empties at a nearly constant rate. *Dry* flows propagate at slower velocities, and at a given time their height in the channel is significantly higher than that of the other types of flows. Then, water and initially fluidized granular flows enter into a second, constant velocity phase. Transition between the first and second phase occurs when the flow height in the channel has a maximum value (h_f ~0.2h_0), whereas the column height is about half its initial value. In the case of high initial reservoir height, this transition corresponds to a sudden acceleration of the front (Figure 2.6b). During most of the second phase, the flow height in the channel is approximately constant, except at the entrance of the channel and at the flow front (Figure 2.4). A notable result is that granular flows

resulting from initially fluidized, slightly expanded columns (at U_{mb}) and water flows propagate at almost the same velocity. Water flows are inertial at that stage as the Reynolds number

$$Re = \frac{\rho_w U h_f}{\mu_w} \tag{2.2}$$

is $3x10^4$-$2x10^5$, where ρ_w and μ_w are the density and dynamic viscosity of water, respectively, and U is the flow front velocity. Granular flows generated from non-expanded fluidized columns (at U_{mf}) propagate less rapidly, whereas the column height in the reservoir and flow height in the channel are similar to that of flows of water and those resulting from slightly expanded fluidized columns (at U_{mb}). Compared to other cases, *dry* flows are significantly slower during this stage although their height in the channel has acquired about the same value, and the column height in the reservoir is now much larger. Transition to a last, third phase is identified from the data of water flows and that of granular flows generated from columns fluidized at U_{mb}. This occurs when the column height has dropped to almost that of the flow in the channel, that is, when the driving pressure between the material in the reservoir and the channel has reduced significantly. The behavior of the initially fluidized (at U_{mb}) granular flows only departs from that of water flows at that stage. Although data of flow and column heights are similar, those of the flow front position clearly deviate from each other. During this third phase, water flows propagate at a velocity slightly smaller than that in the second phase, whereas the granular flows steadily decelerate. It is worth noting that our first (acceleration) and second (constant velocity) phases correspond to the slumping phase described for fluid gravity currents [*Huppert*, 2006].

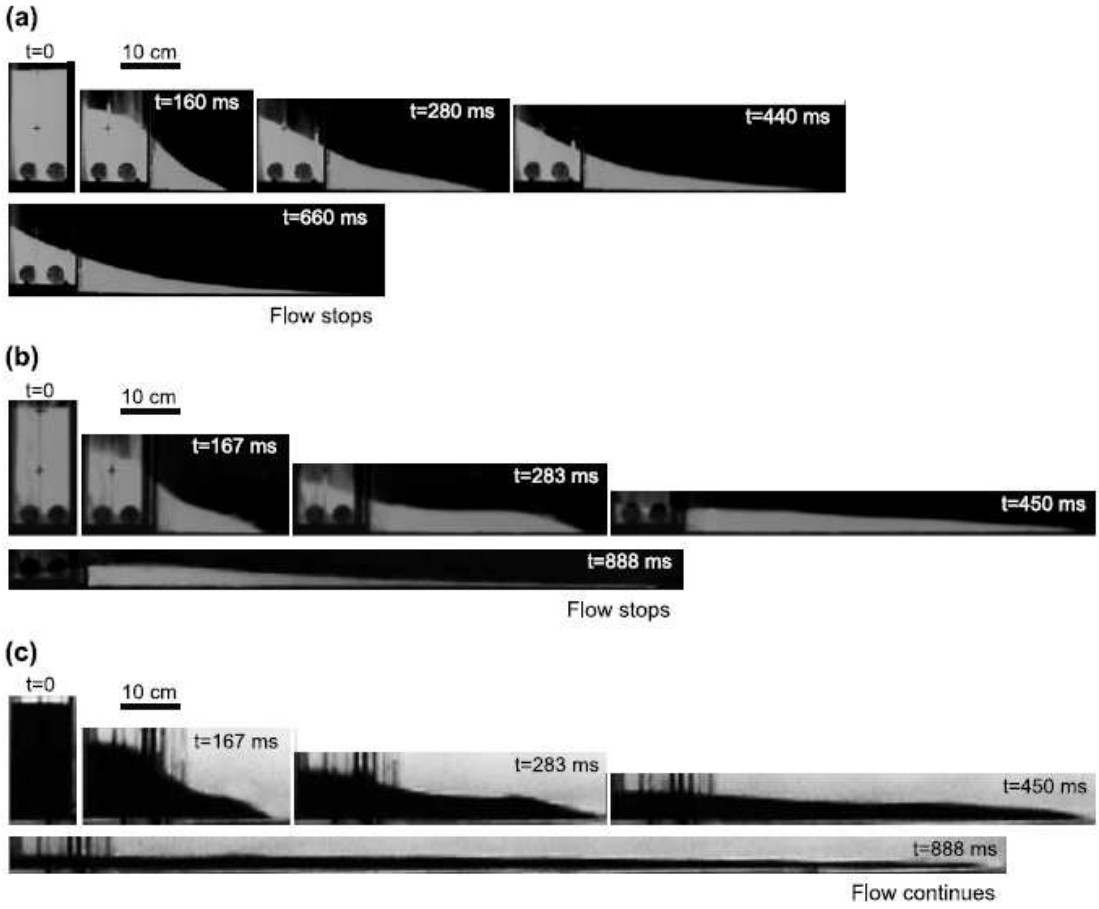

Figure 2.4. Snapshots of dam-break flows (time in milliseconds). Flows generated from columns (h_0=20 cm, x_0=10 cm, r=2) of (a) *dry* granular material, (b) fluidized, slightly expanded (e=2.5-4.5%) granular material with air velocity U_{mb} in the reservoir, and (c) water (dyed). After release, (b) and (c) propagate at almost constant height and velocity (e.g., t=283 ms), and water flows are inertial at that stage. Initially fluidized granular flows behavior departs from that of water flows only when the column height has decreased to almost the flow height at the entrance of the channel (t>450 ms).

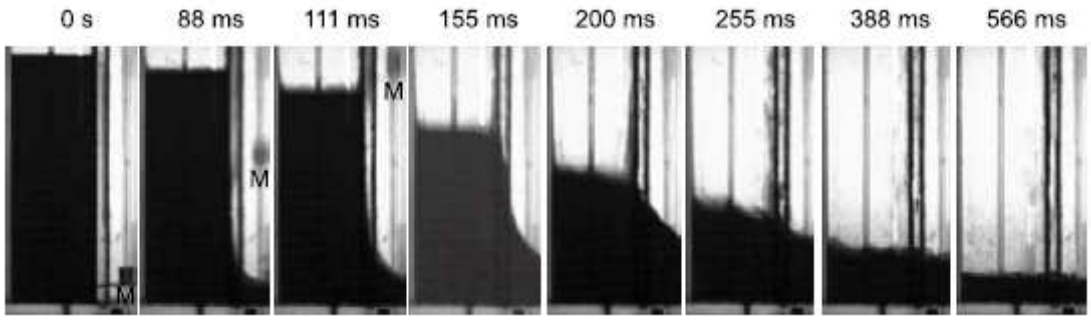

Figure 2.5. Vertical descent of the water column within the reservoir (h_0=30 cm, x_0=10, r=3). M indicates the mark on the sluice gate and numbers indicate time in milliseconds.

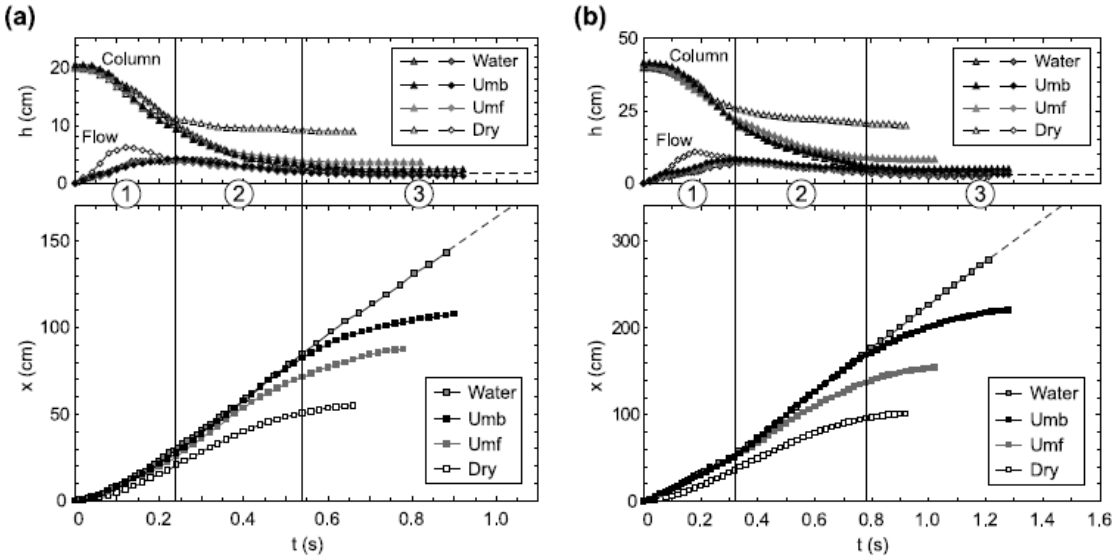

Figure 2.6. Kinematic data of dam-break flows. Flow kinematics for reservoir aspect-ratio r=2, with flow front position (x), and column and flow height (h) as a function of time (t). (a) h_0=20 cm, x_0=10 cm, and (b) h_0=40 cm, x_0=20 cm. Numbers in circles correspond to phases 1 (column collapse), 2 (constant velocity), and 3 (stopping phase of granular flows). Granular flows generated from columns fluidized at U_{mb} behave as water flows until transition between phases 2 and 3. Dashed lines indicate that water flows continue. *Dry* flow behavior clearly departs from that of other types.

2.4.2 Collapse of the kinematic data

The behavior of the dam-break flows investigated in our study can be characterized quantitatively through scaling considerations. For this, we determined appropriate time and length scales in order to collapse the kinematic data of the experiments over a range of initial column aspect ratios in the reservoir (r=0.5-3). We considered length scales x_0, h_0, or $(x_0 h_0)^{1/2}$, and time scales $(x_0/g)^{1/2}$, $(h_0/g)^{1/2}$, or $x_0/(gh_0)^{1/2}$ and tested all possible combinations to plot normalized data of length as a function of time. We conclude that the appropriate time scale is $(h_0/g)^{1/2}$, which is proportional to the characteristic time of free fall of the column $(2h_0/g)^{1/2}$, whereas the relevant length scale is h_0, the initial column height in the reservoir. Other time and length scales do not lead to collapse of the data for the range of reservoir aspect-ratios considered. The characteristic time and length scales we used were proposed already to describe the motion of dam-break-flows of water with reservoirs having a very low aspect-ratio (r<<1) [*Leal et al.*, 2006], and our experiments offer the opportunity to test the relevance of those characteristic scales for reservoirs with a higher aspect-ratio. We note that the length scale chosen by earlier works to describe the motion of *dry* granular flows is the reservoir length x_0 [*Lube et al.*, 2004; *Lajeunesse et al.*, 2005], and this issue is addressed hereafter.

Figure 2.7 shows collapse of the data for water and initially fluidized granular flows over the range of reservoir aspect-ratios investigated, and emplacement in three distinct phases is controlled by the time scale $(h_0/g)^{1/2}$. Transition between the first (collapse) and the second (constant velocity) phase occurs at dimensionless time $t/(h_0/g)^{1/2}$~1.5, with h_c/h_0~0.5 and maximum flow height h_f/h_0~0.2. At that stage, data collapse of the flow front position for each

flow type is very good, whereas the normalized flow or column height slightly decreases when the reservoir aspect-ratio increases. It is worth noting that gate opening is rapid as its base is above the top of the collapsing column at times $t/(h_0/g)^{1/2}$ less than about 0.3-0.5 (see also Figure 2.5). Transition to the last, third (stopping) phase as the column height in the reservoir has dropped to almost that of the flow in the channel occurs at $t/(h_0/g)^{1/2}$~4. During this phase, normalized flow and column height both tend to 0.07-0.15. There is a tendency for the normalized flow front position to slightly decrease as the reservoir aspect-ratio increases. However, initially fluidized granular flows have similar relative durations, t_f, so that $t_f/(h_0/g)^{1/2}$~5.5-6 and ~6-6.5 at initial air flow velocity in the reservoir U_{mf} and U_{mb}, respectively. On the other hand, motion ceases at normalized distance x/h_0~4.5-5 (at U_{mf}) and ~5.5-6 (at U_{mb}). Compared to *dry* cases, initial fluidization of the granular column in the reservoir enhances the relative flow duration and run-out by a factor of ~1.2-1.4 and ~1.8-2.2, respectively. *Dry* granular flows depart from others, as they propagate at lower front velocity with transition between the first and the second phase occurring earlier and with greater maximum flow height. The data of the column height in the reservoir do not collapse under this normalization. However, the data of the flow front position do collapse, both in space and time.

The relative duration and distance of propagation of the three phases of emplacement are the same for the three types of granular flows investigated. Figure 2.8 reveals very good collapse of the front position (x) data as a function of time, when using the run-out, x_f, and t_f as length and time scales, except maybe for *dry* flows during the first phase. The transition between the first and the second phase occurs at ~25% of the flow duration and run-out, whereas that between the second and the third phase occurs at ~65% of the flow duration and ~80% of the run-out. During the third, stopping phase, granular flows generated from fluidized columns behave as their *dry* counterparts. When kinematic data (x vs. t) are plotted in logarithmic scales, the best fit of the values when flows decelerate and before their motion ceases (third phase) gives slopes of 0.30-0.35, and we assume that the normalized flow front position varies with time to the power 1/3 (Figure 2.9).

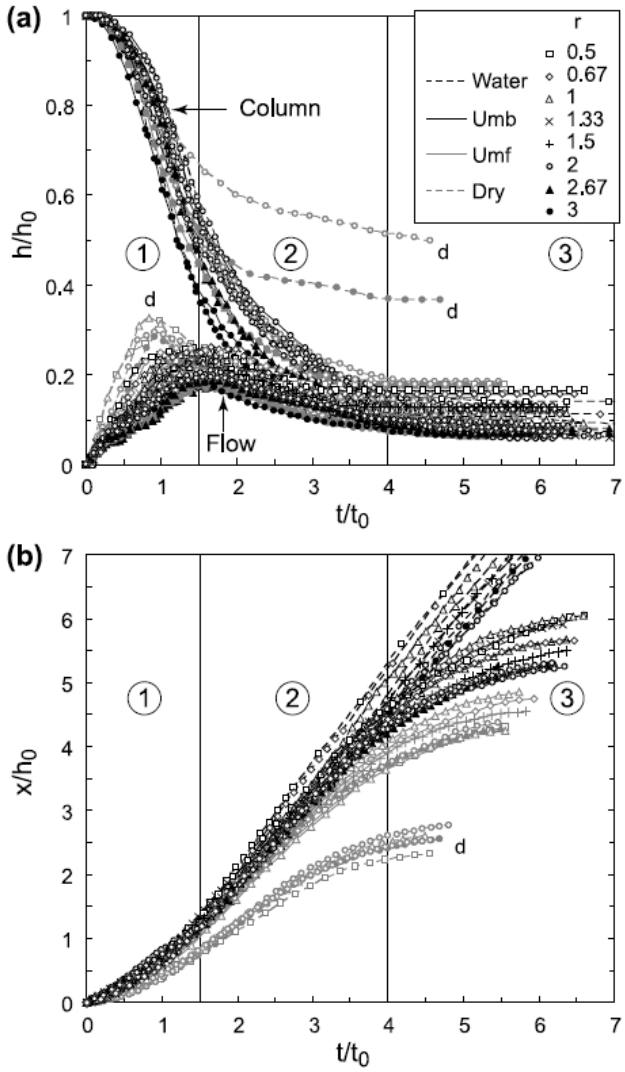

Figure 2.7. Non dimensional kinematic data of dam-break flows. Data are shown for various reservoir aspect-ratios r with normalized (a) column and flow height h/h_0 and (b) flow distance x/h_0 as a function of time t/t_0, with $t_0=(h_0/g)^{1/2}$. Data for the column height are shown when the column collapses with little deformation of the top (r>1.5). Numbers in circles correspond to phases 1 (column collapse), 2 (constant velocity), and 3 (stopping phase of granular flows). *Dry* granular flows are marked with a *d* in the plot.

Analysis of the kinematic data of our dam-break experiments shows that the characteristic time and length scales, $(h_0/g)^{1/2}$ and h_0, respectively, used previously to describe the kinematics of dam-break flows of water generated from reservoirs having very low aspect-ratios [*Leal et al.*, 2006], are also relevant in the case of reservoirs of high aspect-ratios (at least up to 3) for which no backward wave in the reservoir occurs, and the column rather collapses vertically as gravitational acceleration is preponderant. We emphasize that the length scale x_0 used in previous studies on dry granular flows [*Lube et al.*, 2004; *Lajeunesse et al.*, 2005] is less appropriate to collapse the kinematic data over the range of initial column aspect-ratios tested (r=0.5-3). Figure 2.10 shows the flow front position normalized using x_0 instead of h_0, x/x_0. In that case, collapse of the data is possible only for same values of the initial aspect-ratio, and this applies to all types of flows considered in this study, i.e., water flows as well as initially fluidized and *dry* granular

flows. We note that collapse of the data for all aspect ratios is readily obtained if x/x_0 is renormalized as $(x/x_0)/r=x/h_0$, as shown in Figures 2.7 and 2.9.

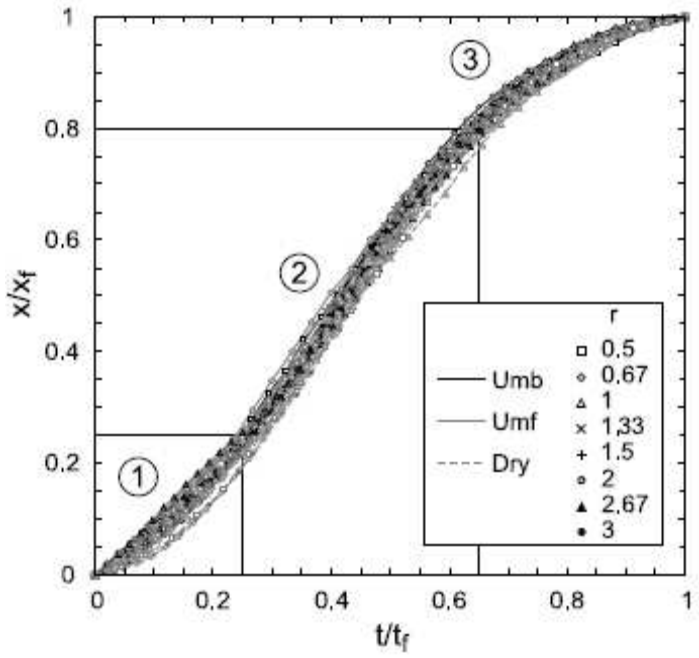

Figure 2.8. Kinematic data of the granular flows normalized with the run-out distance (x_f) and the flow duration (t_f) for the whole range of reservoir aspect-ratios investigated (r=0.5-3). All flows have same relative duration and distance of propagation for the three phases of emplacement.

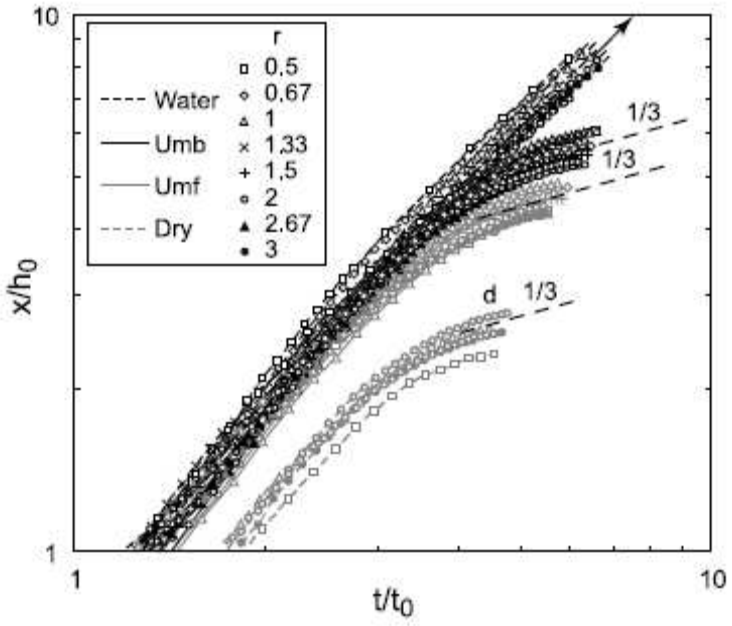

Figure 2.9. Stopping phase of the granular flows. Flow kinematics shown for various reservoir aspect-ratios r with normalized flow distance x/h_0 and time t/t_0, with $t_0=(h_0/g)^{1/2}$ in a log-log plot. The arrow indicates that water flows continue. Granular flows, including *dry* ones (noted *d*), steadily decelerate during the third, stopping phase
as the front position varies as $t^{1/3}$ before they come to halt (dashed lines).

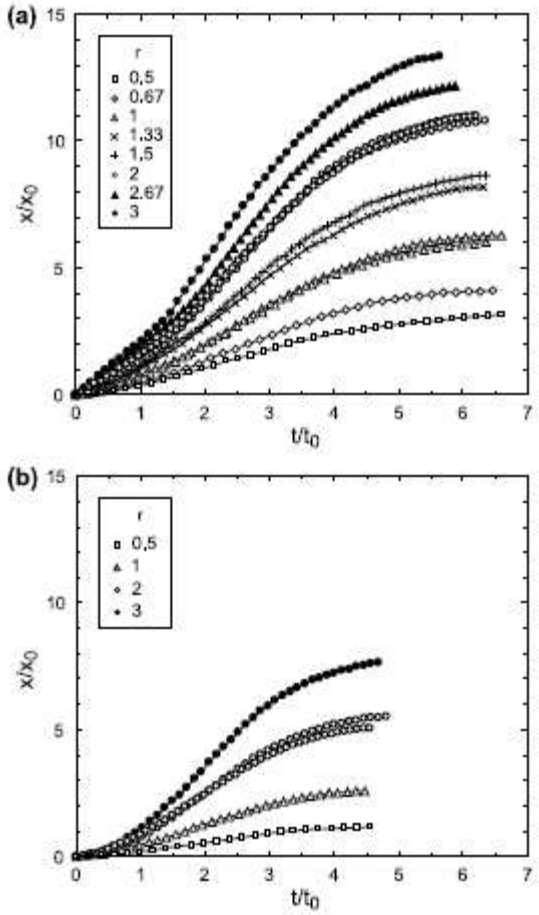

Figure 2.10. Kinematic data of the granular flows generated from columns (a) fluidized at U_{mb} or (b) with no air flux (*dry*), shown for various reservoir aspect-ratios r, with normalized flow distance x/x_0 and time t/t_0, with $t_0=(h_0/g)^{1/2}$. The data collapse only for experiments at same r (i.e., 1 and 2).

2.4.3 Flow dynamics

The dynamics of the flows can be investigated through analysis of the Froude number (i.e., the normalized flow velocity) during the first and/or the second phase as the front velocity is nearly constant. We calculated the source Froude number, defined as

$$Fr_0 = \frac{U}{(gh_0)^{1/2}} \qquad (2.3)$$

and we note that this is also the slope in Figure 2.7b. Values of Fr_0 in the first phase can be determined for flows of water and those generated from fluidized granular columns and propagating at almost constant velocity at that stage, that is for cases at sufficiently high initial reservoir height (h_0>20 cm). The calculation can be made in all cases for the second phase. The results in Figure 2.11 reveal that, for the first phase, values of Fr_0 decrease from about 1.2 to 0.7 as the reservoir aspect-ratio increases from 1 to 3, but are independent of the type of flow. In the second phase, the source Froude number is independent of the reservoir aspect-ratio. In flows of water and those generated from slightly expanded granular columns fluidized at U_{mb}, Fr_0 has a

similar value, as a matter of fact close to the theoretical value $\sqrt{2}$ for a steady orifice flow [*White*, 2003]; and this issue is addressed hereafter. In non-expanded granular flows initially fluidized at U_{mf}, values of Fr_0 are lower, in the range from about 1 to $\sqrt{2}$. *Dry* granular flows have even lower values as Fr_0~0.9-0.95.

Further insights into the flow dynamics are obtained through analysis of the flow Froude number, defined as

$$Fr = \frac{U}{(gh_f)^{1/2}} \tag{2.4}$$

The results are shown in Figure 2.12 as a function of the normalized time, and we note that $Fr=Fr_0/(h_f/h_0)^{1/2}$. Once again, the data for *dry* flows are clearly distinguishable from the others. During the first phase, of approximately constant front velocity (at h_0>20 cm), the flow Froude number decreases with time as the flow height in the channel increases. Values for the initially fluidized granular flows tend to be slightly lower than those of water flows. We observe a sudden acceleration between the first and second phase, thus explaining a sharp transition at $t/(h_0/g)^{1/2}$~1.5 in Figure 2.12, as mentioned already for data in Figure 2.7. Thus, *Fr* increases as flows enter the second phase and propagate at a larger (also approximately constant) front velocity. For flows of water and of granular matter initially fluidized at U_{mb}, *Fr* is approximately constant and in the range 2.8-3.2 during a time interval $t/(h_0/g)^{1/2}$~0.5. Then, it increases gradually to about 3.5-4 as the flow height decreases. Granular flows generated from columns fluidized at U_{mf} propagate in the second phase at lower *Fr* values of about 2.5-3.

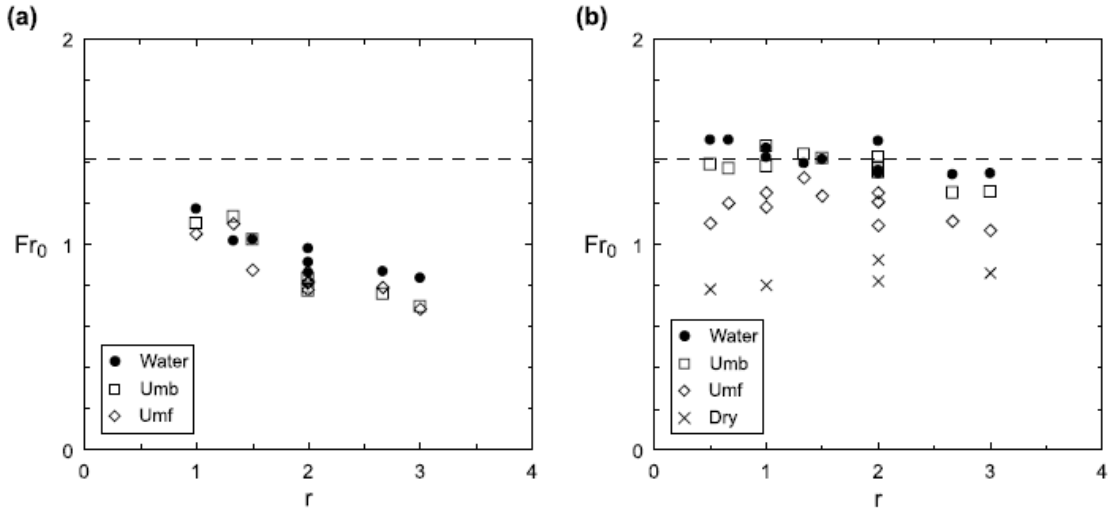

Figure 2.11. Source Froude numbers of the flows $Fr_0=U/(gh_0)^{1/2}$, as a function of the reservoir aspect-ratio *r*, for (a) the first and (b) the second phase of emplacement. The dashed line indicates the theoretical value $Fr_0=\sqrt{2}$ for a steady orifice flow. In (a), data correspond to experiments with water and initially fluidized granular flows and of initial column height h_0>20 cm, that is, to flows that propagate at constant velocity.

2.5 Discussion

2.5.1 The mechanisms of dam-breaking

The results of our experiments on dam-break flows are now compared with those of similar works carried out with water or dry granular material. Our experiments on flows resulting from the release of water or fluidized granular columns reveal notable differences from *Ritter*'s [1892] simple model. At reservoir aspect-ratios larger than about 1.5, no wave propagates backwards in the reservoir, and the column rather collapses vertically with its upper surface remaining almost flat and horizontal (Figure 2.5). This shows that gravitational acceleration cannot be neglected to describe dam-break flows generated from reservoirs of high aspect-ratios. The flow in the channel propagates at a front velocity $U \sim \sqrt{2}(gh_0)^{1/2}$, independent of the initial reservoir aspect-ratio for r=0.5-3. This velocity is lower than the value predicted for the ideal frictionless case for which $U=2(gh_0)^{1/2}$ [*Ritter*, 1892]. This means that resistance introduces important retardation of flow motion. We emphasize that the flow front velocity we determined in our study is consistent with observations made in water dam-break experiments, as reviewed by *Leal et al.* [2006; their Figure 2.3]. Their water flows are generated from reservoirs having low aspect-ratios (r<<1), and their front velocity is given by $U \sim \sqrt{2}(gh_0)^{1/2}$ over normalized time $t/(h_0/g)^{1/2}$ and distances x/h_0 of about 5 and 6, respectively, and subsequently decreases slowly. Interestingly, our data show that this flow front velocity is the same for a large range of reservoir aspect-ratios.

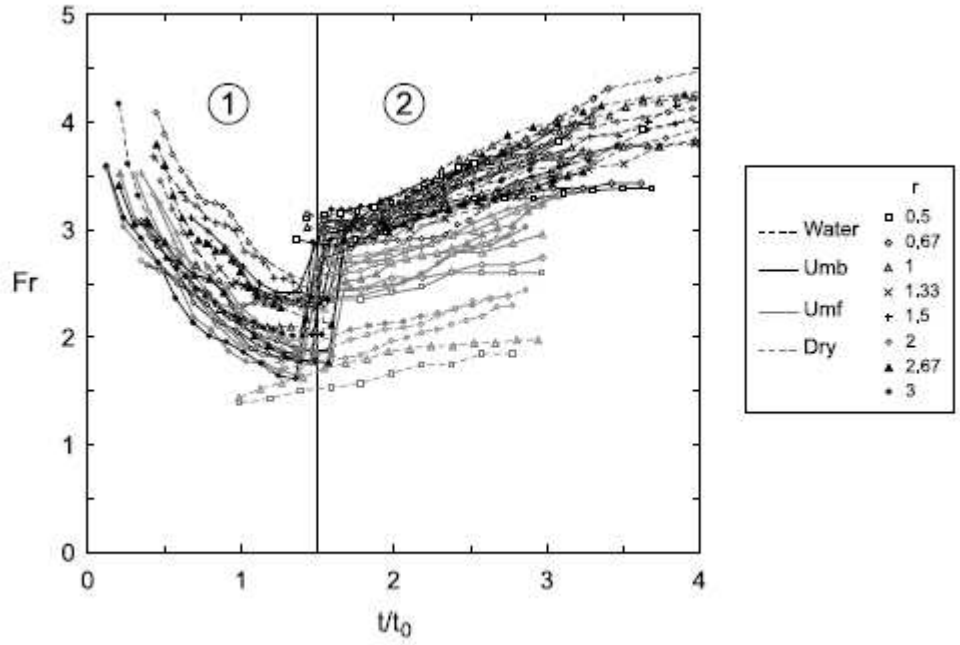

Figure 2.12. Flow Froude number $Fr=U/(gh_f)^{1/2}$ as a function of normalized time t/t_0, with $t_0=(h_0/g)^{1/2}$, for the first and second phase of emplacement of all types of flows. A sharp transition occurs at $t/t_0 \sim 1.5$ as a sudden acceleration between the two phases is observed.

In recent theoretical analyses of dam-break flows of a pure fluid, *Hogg and Woods* [2001] and *Hogg and Pritchard* [2004] showed that in the inertial regime, with negligible internal viscous forces, motion results from a balance between the streamwise gradient of hydrostatic pressure (buoyancy), fluid inertia, and resistance (presumably dominated by drag at boundaries). *Hogg and Pritchard* [2004] tested various resistance terms in their depth-average models, assuming that resistance at boundaries derives either from, (1) viscous effects ($\xi \sim \mu(U/h)^{\alpha}$), where ξ is the resistance stress, μ is dynamic viscosity, h the flow depth, and α some exponent, (2) Coulomb-like friction (ξ proportional to ρgh) that is uniform throughout the fluid domain, where ρ is the fluid density, or (3) shear drag associated with turbulent fluid motion (ξ proportional to ρU^2). They compared their results to those of some experimental studies and concluded that models with a turbulent, Chezy-type drag term having the form $\xi=\rho C_d U^2$, where C_d is a drag coefficient with a value 0.01-0.001, best describes the motion of dam-break flows of a pure Newtonian fluid. They showed that drag, which is applied on the whole extent of the flow, has a greater effect at the flow front where the local driving pressure is small because of small height, and in consequence the fluid builds up and the front steepens to increase the pressure gradient, which counters the flow resistance. The distance over which drag at boundaries has a significant influence is expected to increase with time. The calculated front velocity is smaller than that predicted if drag at boundaries is neglected, so that $U/(gh_0)^{1/2}=Fr_0=2$ [i.e., *Ritter*, 1892], and $U/(gh_0)^{1/2}=Fr_0$ is slightly less than about $\sqrt{2}$ [*Hogg and Pritchard*, 2004; their Figures 2.9 and 2.11]. This latter value depends on the drag coefficient. We note that the value $\sim\sqrt{2}$ is also the one we determine in our experiments, which suggests that the processes that generate resistance acting in the laboratory flows we tested could be comparable to those described by *Hogg and Pritchard* [2004], and that the drag coefficient in our experiments (with water and initially fluidized granular flows) would be similar.

Flows generated in dam-break conditions result basically from the collapse of the initial column under the influence of gravity once the sluice gate is removed. In consequence, it is interesting to find that the source Froude number (Fr_0) has a value close to that corresponding to a steady frictionless orifice flow, which is somewhat paradoxical as the material is progressively evacuated from the reservoir in our experiments and the flows are dissipating energy as they propagate along the channel (Figure 2.13). Nonetheless, as already discussed, this can be theoretically explained from *Hogg and Pritchard* [2004] analysis.

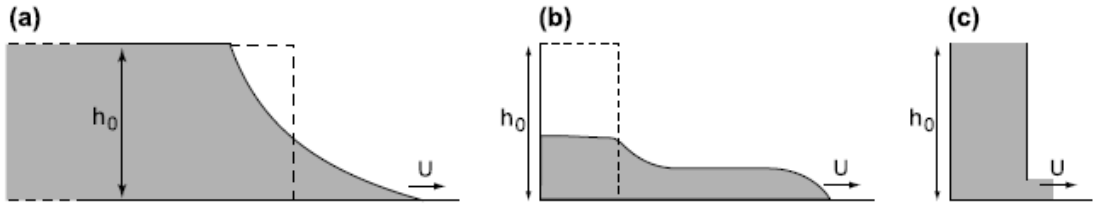

Figure 2.13. Schematic representation of flows propagating at front velocity U, (a) in case of ideal frictionless dam-breaking, $U=2(gh_0)^{1/2}$ [*Ritter*, 1892]; (b) in this study, $U\sim\sqrt{2}(gh_0)^{1/2}$; and (c) for a steady orifice flow, $U=\sqrt{2}(gh_0)^{1/2}$.

2.5.2 Water-like behavior of initially fluidized, dense granular flows

Our experiments show that, under dam-break conditions, granular flows generated from slightly expanded columns (fluidized at U_{mb}) have the same kinematics as inertial water flows, as long as motion is driven by a pressure gradient between the reservoir and the channel. According to our description, this occurs during the first (collapse) and the second (constant velocity) phase, until normalized time $t/(h_0/g)^{1/2}$~4 and distance x/h_0~4.5. This suggests that, at those stages, the overall balance between inertia, hydrostatic pressure gradient (buoyancy) and resistance, typical of inertial fluid gravitational flows [*Hogg and Pritchard*, 2004] is, in these dense granular flows, similar to that of flows observed in water dam-break experiments. Furthermore, based on *Hogg and Pritchard* [2004] analysis, the fact that the value of the source Froude number observed in the initially fluidized (at U_{mb}) granular flows is about the same as that of water flows (observed in our and previous experiments, so that Fr_0~$\sqrt{2}$) suggests that the drag coefficient in both types of flows would be (1) of the inertial turbulent form and (2) possibly of the same value. This represents the main result of our study and provides new insights into the physics of dense granular flows.

The overall energy dissipation derives from interactions between the flow and its boundaries, and also from internal processes in the case of the granular flows. *Iverson* [1997] showed that for fluid-particle flows internal energy dissipation can result from particle contact interactions such as friction and collisions, viscous shear and turbulent velocity variation of the interstitial fluid, and drag (of viscous or inertial origin) between the particles and the interstitial fluid. He proposed a series of dimensionless numbers aimed to assess the relative magnitude of the different stresses, and we refer to some of them hereafter. In our *dry* granular flows, particle interactions are a dominant source of energy dissipation as shown by their slow velocity of propagation and small run-out (Figures 2.6 and 7). Under dam-break conditions, these flows have been modeled following different approaches including discrete element and shallow-water methods [*Kerswell*, 2005; *Zenit*, 2005; *Larrieu et al.*, 2006; *Doyle et al.*, 2007], and at least qualitative agreement with experimental data [*Balmforth and Kerswell*, 2005; *Lajeunesse et al.*, 2005; *Lube et al.*, 2005] has been achieved. Our results suggest that friction and collisions are very much reduced in initially fluidized granular flows, although these emplace at almost maximum concentration, and this serves as a base for the following discussion. These flows propagate at the same velocity as that of water flows when the initial column expansion is only 2.5-4.5%, and it is interesting to note that this velocity is only slightly smaller when the initial column is not expanded, if fluidized at U_{mf}. This suggests that once contact forces in the chain network of the initial granular column are dramatically weakened, reversal to a frictional and collisional regime during flow emplacement is very much delayed.

Buffering of particle interactions resulting from slow diffusion of the initial pore pressure caused by air flux in the reservoir is very unlikely, as discussed earlier by *Roche et al.* [2004]. The pore pressure diffusion timescale is t_d~h_f^2/D [*Iverson*, 1997], where D is the pore pressure diffusivity of the granular material. *Montserrat et al.* [2007] have shown that D~0.02 m^2 s^{-1} for the granular material used in experiments reported here. This means that if we consider a typical mean flow height in the channel of 0.02-0.08 m, then the initial excess pressure is eliminated in only 3-6% of the flow duration once the flow enters the channel.

On the other hand, flow dynamics is not governed by the interstitial air dynamic viscosity (μ_a) in our experiments, as shown by corresponding values of the Bagnold number [*Bagnold*, 1954; *Iverson*, 1997]

$$Ba = c^* \frac{\rho_s \gamma d^2}{\mu_a}, \tag{2.5}$$

where $c^*=[c^{1/3}/(c_0^{1/3}-c^{1/3})]^{1/2}$, with c denoting concentration of the material during flow propagation, c_0 the maximum concentration at loose packing, and γ is the shear rate, which is typically considered to be equal to U/h_f for the computation and analysis of *Ba* and other relevant dimensionless parameters [e.g., *Iverson*, 1997]. The Bagnold number represents a measure of the ratio of particle collisional stresses to fluid viscous shear stresses. For the range of experiments investigated, *Ba*~280-970, which is above the upper limit value of ~45 for a macro-viscous regime [*Bagnold*, 1954]. Alternatively, the highest *Ba* values (>~450) could suggest significant interparticle collisions. This interpretation, however, has been challenged by *Hunt et al.* [2002] who showed that if a collisional regime probably exists at lower particle concentrations and higher shear rates, the limit proposed by *Bagnold* [1954] is not valid and derives from a misinterpretation of his experimental results. *Iverson* [1997] proposed an alternative Bagnold number, *Ba'*, with $c^*=c/(1-c)$, such that a fluid-particle flow is then dominated by collisional contacts at *Ba'*>~200. In our experiments *Ba'*~150, below the limit value proposed by *Iverson* [1997], suggesting that energy dissipation through interparticle collisions, if present, would not be a dominant process. Furthermore, large values of *Ba'* may not necessarily imply occurrence of a collisional regime, as the interstitial fluid dynamics coupled to unsteady particle motion can damp particle contact interactions under certain conditions [*Iverson*, 1997; *Iverson and LaHusen*, 1989], as discussed hereafter.

Significant fluctuating energy has been observed in fluidized beds of particles of group A [*Cody et al.*, 1996; *Biggs et al.*, 2008], such as those of our experiments, indicating that unsteady particle motion can be relevant in our flows at least during the initial stages of emplacement. Because of this, our dense granular flows could be dominated by interactions between the particles and the interstitial air, as shown for continuously fluidized slow flows or vibrated beds [*Eames and Gilbertson*, 2000; *Burtally et al.*, 2002]. Air-particle interactions, along with drag at boundaries, could confer to these highly concentrated granular media a behavior similar to that of inertial water flows. The intensity of these interactions can be estimated using the Darcy number [*Iverson*, 1997], which represents the ratio of viscous fluid-particle interactions stresses to particle inertial stresses, so that

$$Da = \frac{\mu_a}{kc\rho_s \gamma}, \tag{2.6}$$

where k is the permeability of the granular medium (~10^{-12} m^2 in this study). In this definition Darcy's law for viscous stresses in the interstitial fluid is assumed to be valid. It is well known that for flow in a porous medium Darcy's law is valid for particle Reynolds number, defined as

$$Re_p = \frac{v\delta\rho_a}{\mu_a}, \tag{2.7}$$

where v is the bulk velocity of the interstitial fluid flow, δ is a characteristic size of the interstices, and ρ_a the air density, lower than about 1-10 [*Rhodes*, 1998]. In the case of a granular flow, we are interested in describing the motion of the fluid relative to the particles. Following *Iverson* [1997], we can estimate $v\delta \sim \gamma d^2$, where d is the particle diameter representative of the granular medium. Using this result and replacing (7) in (6) we obtain

$$Da = \frac{\rho_a}{\rho_s} \frac{d^2}{Re_p kc}. \qquad (2.8)$$

Imposing the limit Re_p<1-10, we conclude that in our experiments for Darcy's law to be valid, Da needs to be larger than about 2 to 20. Estimating Da in our experiments, we obtain values in the range ~170-370. This implies two things, first that the fluid-particle interactions in our flows are purely viscous (no inertial coupling, that is, Darcy's law is valid) and second, that viscous fluid-particle interactions stresses are dominant over particle inertial stresses because of the large values of Da obtained. A similar conclusion is reached if one considers the ratio of viscous fluid-particle interactions stresses to particle (frictional) shear stresses, which, based on *Iverson*'s [1997] analysis, would be proportional to $\gamma\mu_a d/[c(\rho_s-\rho_a)gk]$. In our experiments, this ratio is two to three orders of magnitude smaller than the maximum value required for Darcy's law to be valid (i.e., Re_p<1-10), thus showing that viscous fluid-particle interactions stresses are also dominant over particle shear stresses.

Iverson [1997] suggested, probably based on the experimental study reported by *Iverson and LaHusen* [1989], that the Darcy number also describes the tendency for pore fluid pressure developing between moving grains to buffer particle interactions. According to *Iverson and LaHusen* [1989] unsteady motion of grains can produce pore pressure that is able to locally support normal and shear stresses, while grain contacts transiently vanish. The pore pressure generated can then propagate to adjacent areas, which, in turn, can generate shear zone growth. As viscous fluid-particle interactions stresses are dominant over both particle inertial and shear stresses in the present initially fluidized granular flows (i.e., high values of Da, for instance), we may infer that pore pressure is likely to be generated in the moving granular mass, which would promote buffering of grain interactions. Additionally, air may act as a thin cushion between the particles and damp interparticle contacts as the grains are agitated during flow emplacement. The fluctuating energy (i.e., granular temperature) initially imposed to the particles when they are fluidized in the reservoir could additionally participate in the enhanced mobility of the flows. As a matter of fact, significant granular temperature was observed in fluidized beds of particles of group A [*Cody et al.*, 1996] and it is maximum for conditions close to U_{mb} [*Biggs et al.*, 2008], which coincide with those that create the granular flows with the longest run-out in our experiments.

We note that in initially slightly expanded granular flows (fluidized at U_{mb}), a return to a compacted state is likely to be achieved during the (first) collapse phase. Assuming that the sedimentation timescale is $t_s \sim eh_f/U_s$, where U_s~8 mm s^{-1} is the fall velocity of the top of the static granular bed in the reservoir determined from collapse tests, this represents only 5-12% of the flow duration. This contrasts with experiments of *Girolami et al.* [2008] carried out with initially highly expanded material (e up to ~50%), which revealed that the flow run-out is controlled by

the sedimentation timescale of the flowing mixture. However, this conclusion was not valid for initial expansion less than 7 %, as it is the case in our experiments. Besides, as already discussed, the time scale of initial pore pressure diffusion is also small compared with the flow duration (3-6%). Thus, air-particle differential motion and associated pore pressure generation during flow emplacement are expected to derive mainly from continuous rearrangement of the granular network, as shown for water-particle flows [*Iverson and LaHusen*, 1989]. Indeed, self-fluidization has been observed in recent experiments by *Bareschino et al.* [2008] on granular flows in a rotating tank using group A particles. These experiments show that a fluid-like behavior can be obtained at sufficiently high shear rates. The authors argue that air, which in their experiments is assumed to be entrained at the flow front through small scale avalanches, is the key factor to confer the fluid-like behavior to these flows.

When the pressure gradient between the material in the reservoir and in the channel has decreased ($h_c \sim h_f$), then the flow velocity, and thus the shear rate (cf. *Da*), is not sufficient to confer a fluid-inertial (water-like) behavior to the granular material. In consequence, air-particle interactions are less efficient and the behavior of the initially fluidized granular flows returns rapidly to that of their *dry* counterparts, which are dominated by interparticle friction. The associated Savage number, which represents the ratio of particle collisional stresses to frictional stresses, defined as

$$Sa = \frac{\rho_s \gamma^2 d^2}{(\rho_s - \rho_a) g h_f} \qquad (2.9)$$

is about 10^{-6}, much less than the upper limit value of 0.1 for the frictional regime [*Savage and Hutter*, 1989]. During the third, stopping phase of emplacement, the flow front position of both types of flows then varies as $t^{1/3}$ until motion ceases (Figure 2.9).

Recent research has suggested a viscoplastic constitutive law to describe the rheology of dry, dense frictional granular flows [*Forterre and Pouliquen*, 2008]. This law is basically of Coulomb type, where the local shear stress is proportional to the normal stress. The proportionality factor, or friction coefficient, would not be a constant but would depend on a dimensionless parameter, the Inertial number, which is a ratio of a microscopic time scale representing the time scale for a particle to fall in the interstices of the granular medium and a macroscopic time scale related to the mean shear rate. The inertial number is equivalent to the square root of the Savage number defined above. In the case where the interstitial fluid becomes important for the behavior of the flow, *Courrech du Pont et al*. [2003] and later *Cassar et al*. [2005] have proposed a modified version of the Inertial number to account for the effects of the interstitial fluid as particles move into the granular network. *Naef et al*. [2006] have also supported the use of viscoplastic constitutive laws for granular flows, such as Bingham. However, in the inertial regime, typical of high velocity flows such as debris flows or snow avalanches, other relationships combining turbulence closures and Coulomb-type friction lead to better results when simulations are compared to natural data [see also *Bartelt*, 1999]. Our results support the concept of a constitutive law that is strongly dependent on the shear rate. Furthermore, the present observations suggest the existence of a combined effect of fluid-particle interactions, that confer the flow an inertial behavior, and shear rate-dependent Coulomb friction as described by *Forterre and Pouliquen* [2008]. Even though the dependence of the Coulomb

friction on shear rate has been proposed in the model described by *Forterre and Pouliquen* [2008], we note that in our flows the effect is of a different nature. Indeed, we observed that as the shear rate decreases, the transition from an inertial to a frictional regime occurs, such that Coulomb friction becomes dominant only at late stages of flow emplacement. Before that, the inertial component is dominant and this leads to a resistance law that is similar to that typical for turbulent fluid flows. Interestingly, *Naef et al*. [2006] pointed out that although an inertial type of resistance can lead to adequate simulations of debris flow motion, it is insufficient to describe cessation of motion, for which a yield stress or Coulomb friction must be taken into account.

2.5.3 Insights into the physics of pyroclastic flows

Our dam-break experiments reveal that a slight expansion of an initial granular column is sufficient to confer on the resulting flow a behavior similar to that of an inertial fluid flow for most of its emplacement, because strong viscous fluid-particle interactions can develop. In this context, a continuous source of gas is not required to maintain the mixture in a fluidized state. In nature, granular expansion at least equal to that in experiments is readily achieved in case of sedimentation from an eruptive column or a dilute ash cloud and can also be obtained when a dense basal avalanche is agitated while propagating down a rough substratum (e.g., Figure 2.1). In experiments, the condition required for a water-like behavior is a pressure gradient derived from a difference in height, even very small, between the reservoir and the channel material. In nature, the driving pressure may derive from the height difference between the top of a large eruptive column and the resulting flow in case of propagation on rather flat areas (Figure 2.1a; and our experiments may be considered as simple analogues of this), or from the gradient of the free surface of the flow as this propagates down a steep slope, in the case of small columns or collapsing domes (Figure 2.1b).

Our results support the pyroclastic flow modeling approach by *Levine and Kieffer* [1991], based on open-channel hydraulic theory. In their model, the flow is assumed to be confined, fully turbulent (inertial) and incompressible with uniform density. The simulation of *Levine and Kieffer* [1991] successfully reproduced the observed velocity (~5-30 m s^{-1}) of the pyroclastic flows produced at Mount St. Helens on August 7, 1980, that propagated on slopes of ~15° in the upper parts and of ~2° in distal areas. This approach is appealing in the context of hazard assessment, as it requires only topographic data, a volumetric flow rate, and a Manning resistance coefficient. Accurate topographic data can be obtained for most volcanoes, and volumetric flow rates can be estimated considering a given eruption style (i.e., column or dome collapse). Even though our results suggest that the drag coefficient in our initially fluidized granular flows would be similar to that of our laboratory water flows, we would not recommend the use of typical values of the Manning or other friction coefficients for water flows in rivers to simulate the motion of pyroclastic flows. The issue of determining appropriate resistance coefficients for pyroclastic flows deserves further research.

Our experiments are applicable to natural cases provided dynamic similarity applies. In this context, we stress that the results we obtain in our experiments with initially slightly expanded granular flows that emplace as water flows are possible because we used group A particles [*Geldart*, 1973]. These particles allow for homogeneous dense phase expansion, though

very small, which provides conditions for efficient viscous fluid-particle interactions to develop throughout the granular network. Previous similar experiments with coarser group B and D particles have shown that initially fluidized granular flows return to a frictional granular regime immediately after release [*Roche et al.*, 2002 and 2004]. Laboratory investigations have shown that, in fact, ash-rich pyroclastic material behaves as group A particles when gas fluidized [*Druitt et al.*, 2007] and this suggests that the type of fluid-particle interactions inferred to act in our experimental flows could likely occur in highly-concentrated, ash-rich pyroclastic flows. Furthermore, the inertial behavior of the laboratory flows suggests that the basic scaling determined in this paper could also apply to field scale pyroclastic flows, which would most likely also be inertial. The viscous fluid-particle interaction effect we have pointed out in this study may buffer the interparticle friction and collisions. We have argued that viscous fluid-particle interactions are controlled by the Darcy number, which in our experiments reaches sufficiently high values so that these interactions are dominant. For pyroclastic flows, calculation of the Darcy number is not straightforward as one needs to assess the permeability, shear rate, and mean grain size because of the particle Reynolds number requirement (i.e., Re_p<1-10). However, considering likely estimations for ash-rich pyroclastic flows, the values of the Darcy number in these flows can still be above the critical value for viscous fluid-particle interactions to be dominant. With these assumptions, dense, ash-rich pyroclastic flows can then be expected to propagate on simple topographies (with a continuously decreasing slope) as inertial fluid flows during most of their emplacement, and would enter a granular-frictional regime at late stages. However, any positive brake in slope could accelerate the flow, which would return to a fluid-inertial regime.

2.6 Conclusion

The present work on dam-break flows of both granular matter and water on a horizontal surface brings new insights into the physics of granular flows and has important implications for the emplacement mechanisms of dense, ash-rich pyroclastic flows. Experiments were carried out for a wide range of aspect-ratios of the reservoir (r=0.5-3). They show that dense granular flows can propagate similarly to their inertial water counterparts provided they are generated from a fluidized, slightly expanded column (e=2.5-4.5%), and as long as motion is driven by a sufficiently high pressure gradient between the reservoir and the channel. Analysis of the kinematic data reveals that the relevant length scale is the initial reservoir height (h_0), and that flow emplacement occurs in three phases controlled by the timescale of free fall of the column proportional to $(h_0/g)^{1/2}$. The flows experience a first (collapse) phase, and a transition to a second (constant velocity) phase occurs at normalized time $t/(h_0/g)^{1/2}$~1.5 and distance x/h_0~1.2, representing about one fourth the flow duration and run-out. During that second phase, initially fluidized, slightly expanded granular flows and water flows propagate at a nearly constant front velocity $U\sim\sqrt{2}(gh_0)^{1/2}$, about 1.5 times faster than *dry* granular flows. Transition to a last, third phase occurs at $t/(h_0/g)^{1/2}$~4 and x/h_0~4.5, representing about 65% and 80% the flow duration and run-out, respectively, when the height of the column in the reservoir has decreased to about that of the flow in the channel. During this last phase of emplacement, flows of water decelerate slightly whereas those of granular matter enter into their stopping phase as they steadily decelerate before motion ceases at $t/(h_0/g)^{1/2}$~6.5 and x/h_0~5.5-6. The flow front position of the initially fluidized granular flows varies as $t^{1/3}$, as observed also for *dry* granular flows.

These observations suggest that the interstitial gas can damp dramatically particle-particle interactions in granular flows. Viscous, air-particle interactions can be the dominant process in these flows, thus conferring to the two-phase mixture a behavior similar to that of water or any other inertial fluid flow. Once contact forces of the force-chain network are strongly decreased or possibly eliminated, then return to frictional-collisional behavior typical of *dry* granular flows is very much delayed as motion is driven by gravity. A slight expansion of the granular medium is sufficient to confer on the resulting flow a fluid-inertial behavior, thus contrasting fundamentally with that of *dry* granular flows. Flows of initially fluidized, slightly expanded granular matter may be characterized by the same resistance law as that of flows of water for most of their emplacement, corresponding to the first (collapse) and second (constant velocity) phase in the dam-break conditions. As particle interactions are very much reduced, one can envisage that they are (1) totally negligible, or (2) weak and act along with viscous air-particle interactions as internal sources of energy dissipation. Our results suggest that gas-dominated granular flows can be modeled using the hydraulic theory for flows of inertial fluids, as long as motion occurs at a sufficiently high shear rate (cf. high *Da*), whose threshold is to be characterized in more detail. Transition to a second behavior, typical of dry granular flows dominated by particle interactions, must then be taken into account to describe flow motion accurately.

This experimental study has implications for the emplacement of dense, ash-rich pyroclastic flows, as it brings new insights into their physics and helps to identify the most appropriate approaches for their modeling. The flow behavior will be two-fold, (1) inertial fluid-like at sufficiently high shear rate, and this is likely to represent most of the flow emplacement, and then (2) frictional-granular at late stages. In this context, analyses combining resistance terms of inertial-turbulent (ξ proportional to ρU^2) and Coulomb-frictional (ξ proportional to $\rho g h$) form appear to be appropriate tools to simulate the emplacement of these pyroclastic flows.

Acknowledgements. This work was supported by Institut de Recherche pour le Développement (IRD, France), ACI-INSU (France), ANR (France), and ECOS-Conicyt n° C06U01 (France-Chile) projects, and Université Blaise Pascal. S.M. thanks the financial support from MECESUP under project UCH0310 in the form of a Ph.D. fellowship and Departamento de Postgrado y Postítulo de la Vicerrectoría de Asuntos Académicos, Universidad de Chile, in the form of a foreign residence fellowship. An earlier draft benefited from stimulating discussions with Tim Druitt and Jeremy Phillips. Sarah Fagents and two anonymous reviewers are thanked for fruitful reviews.

Chapter 3

3 Pore fluid pressure and internal kinematics of gravitational laboratory air-particle flows: Insights into the emplacement dynamics of pyroclastic flows

This chapter corresponds to the paper authored by Olivier Roche, Santiago Montserrat, Yarko Niño and Aldo Tamburrino, published in *Journal of Geophysical Research*, volume 115 (2010), B09206, 18 pp.

Abstract

The emplacement dynamics of pyroclastic flows were investigated through noninvasive measurements of the pore fluid pressure in laboratory air-particle flows generated from the release of fluidized and nonfluidized granular columns. Analyses of high speed videos allowed for correlation of the pressure signal with the flow structure. The flows consisted of a sliding head that caused underpressure relative to the ambient, followed by a body that generated overpressure and at the base of which a deposit aggraded. For initially fluidized flows, overpressure in the body derived from advection of the pore pressure generated in the initial column and decreased by diffusion during propagation. Relatively slow diffusion caused the pore pressure in the thinner flow to be larger than lithostatic at early stages. Furthermore, partial auto-fluidization, revealed in initially nonfluidized flows, also occurred and contributed to maintain high pore pressure, whereas dilation or contraction of the air-particle mixture with associated drag and/or pore volume variation transiently led the pressure to decrease or increase, respectively. The combination of all these processes resulted in long-lived high pore fluid pressure in the body of the flows during most of their emplacement. In the case of the initially fluidized and slightly expanded (~3-4%) flows, (at least) ~70%-100% of the weight of the particles was supported by pore pressure, which is consistent with their inertial fluid-like behavior. Dense pyroclastic flows on subhorizontal slopes are expected to propagate as inertial fluidized gas-particle mixtures consisting of a sliding head, possibly entraining basement-derived clasts, and of a gradually depositing body.

Keywords: Explosive volcanism, Pyroclastic flow, Granular avalanche, Dam break, Pore fluid pressure, Fluidization.

3.1 Introduction

Dense gravitational fluid-particle flows, for which interactions between the solid particles and the interstitial fluid (liquid or gas) may dominate the flow dynamics, commonly occur in the environment. Examples include debris flows, snow avalanches, and pyroclastic flows, for which the respective fluid phase is water, air, or (principally) volcanic gases [*e.g.*, *Iverson*, 1997; *Hopfinger*, 1983; *Druitt*, 1998]. The present study deals with gas-particle flows, with a special emphasis on pyroclastic flows. These commonly occur during volcanic eruptions and result from the gravitational collapse of a lava dome or of an eruptive column, as well as from the sedimentation of a dilute ash cloud. They consist of a mixture of gas and particles that propagates downslope under the influence of gravity [*e.g.*, *Druitt*, 1998; *Freundt and Bursik*, 1998; *Branney and Kokelaar*, 2002]. Possible additional sources of gas include release from the pyroclasts, burnt vegetation, and entrainment of the ambient air during emission at the vent and propagation. Pyroclastic flows are potentially highly destructive phenomena as they can propagate at speeds of several tens of meters per second, over distances of several tens of kilometers, even on slopes of only a few degrees. A better understanding of the fundamental mechanisms of these natural events, including modes of propagation and deposition, is crucial to better constrain numerical simulations in the context of hazard assessment.

This paper is aimed at investigating the processes that act in natural two-phase gravity currents, and for this we report a series of pore fluid pressure measurements in laboratory air-particle flows. The concept of pore fluid pressure was developed in soil mechanics and has been used subsequently to investigate the dynamics of fluid-particle flows [see *Iverson*, 1997; *Major and Iverson*, 1999; *Major*, 2000; and references therein]. At the base of a static column (of height H) of solid particles with a lighter interstitial fluid (of density ρ_f), the hydrostatic pore fluid pressure is

$$P_h = \rho_f g H , \tag{3.1}$$

where g is the gravitational acceleration. If a vertical differential motion between the particles and the fluid occurs, so that the fluid and the particles move relatively upwards and downwards, respectively, viscous drag is generated and stresses are transmitted to the fluid phase. In consequence, a (so-called) dynamic pore fluid pressure arises, and the total pore pressure is then

$$P = P_h + P_s , \tag{3.2}$$

where P_s results from the buoyant weight of the solid particles counterbalanced by drag. If the weight of the particles is fully supported, then

$$P_s = (\rho_s - \rho_f)(1-\varepsilon) g H , \tag{3.3}$$

where ρ_s is the particle density and ε is the interstitial pore volume fraction (voidage). The interparticle contact stresses, which vary as the inverse of the pore fluid pressure, then vanish as the granular column is fully fluidized. Hence, the value of the pore fluid pressure indicates the amount of the weight of the particles that is supported and gives insights into the degree of particle-particle interactions. Note that if the interstitial fluid is much less dense than the particles, as in the present study, the hydrostatic component of P in Equation 3.2 is negligible, and when the granular column is fully fluidized

$$P \approx \rho_s (1-\varepsilon) g H \,, \qquad (3.4)$$

which corresponds to the "lithostatic" pressure in the column. Dynamic pore fluid pressure can be generated both when a vertical fluid flow is introduced to a static granular column (fluidization) and when a highly concentrated bed of particles settles in a static fluid (sedimentation). The latter case may occur in nature as a granular network contracts, thus generating high pore pressure and low interparticle contact stresses [*Major*, 2000], and this can be the cause of landslide initiation [*Hutchinson*, 1986; *Iverson et al.*, 1997; *Snieder and van den Beukel*, 2004; *Iverson*, 2005; *Montgomery et al.*, 2009]. In contrast, dilation of the granular network can generate a decrease of the pore pressure [*Iverson et al.*, 2000; *Okada et al.*, 2004; *Gabet and Mudd*, 2006]. Once pore pressure is generated, it may decrease through a diffusion process whose timescale is proportional to H^2/D, where H is then the characteristic drainage path length and D is the hydraulic diffusion coefficient [*e.g.*, *Iverson*, 1997].

Measurement of the pore pressure in fluid-particle gravitational flows has been performed in the field as well as in laboratory experiments. Data on natural flows are scarce, due to technical limitations and because these events are rare and hazardous. Pore pressure relative to the ambient of up to ~15 kPa was reported for debris flows and accounted for ~20% of the total normal stress [*Berti and Simoni*, 2005; *McArdell et al.*, 2007] whereas values of ~10-100 Pa were measured in snow avalanches [*Nishimura al.*, 1995; *McElwaine and Turnbull*, 2005]. More investigations have been done on controlled laboratory experiments, during which excess pore pressure indicating partial support of the weight of the particles was commonly measured. Most experiments dealt with water-particle mixtures flowing on (inclined) channels aimed to simulate subaqueaous or subaerial flows, so that the flows propagated under either water [*Ilstad et al.*, 2004; *Cassar et al.*, 2005] or air [*Major and Iverson*, 1999; *Okura et al.*, 2002; *Okada and Ochiai*, 2008]. Only a few works have been carried out on air-particle flows. These include large scale flows of ping-pong balls on a ski jump [*McElwaine and Nishimura*, 2001] and laboratory scale experiments involving particles of polystyrene or snow [*Turnbull and McElwaine*, 2008 and 2009].

In the present study, we carried out measurements of the pore fluid pressure in dam break (*i.e.*, transient) air-particles flows, generated from the release of an initially fluidized or non fluidized granular column, that propagated on a horizontal substrate in the ambient atmosphere. This work was principally motivated by an earlier study, which showed that initially fluidized flows of fine particles under these conditions propagate as inertial currents of pure fluid for most their emplacement [*Roche et al.*, 2008]. This result suggested that the pore fluid pressure in the flows was long-lived and high enough to account for nearly complete fluidization. In order to test this hypothesis, we made detailed measurements of the spatial and temporal variation of the pore pressure in similar flows. The pressure data were then used, along with high speed video analyses, to decipher the internal flow structure in terms of degree of fluidization and depositional processes.

3.2 Experimental apparatus, material, and method

We carried out dam break air-particle flow experiments in an apparatus consisting of a reservoir and a horizontal channel separated by a vertical sluice gate (Figure 3.1). The reservoir and the channel had a length of 20 cm and 300 cm, respectively, and both had a width of 10 cm. The particles in the reservoir were released into the channel as the gate was removed, and the flow generated then propagated until it came to halt and formed a deposit. The gate was lifted by means of a counterweight, thus ensuring rapid opening at consistent speed, and was connected to an electrical switch that indicated the moment of removal. In order to generate a fluidized column of particles in the reservoir, air was supplied by a compressor and pressure was reduced to 1 bar at the entrance of the device. Air was then dried and its volumetric flow rate controlled by a manometer. The flow entered into a windbox filled with coarse (few mm) particles in order to reduce the volume of air. It then passed through a 1 cm-thick porous plate with mean pore size of 20 µm, which allowed for uniform fluidization of the column of particles resting on the plate. The defluidization behavior of the static column in the reservoir with the gate closed was also investigated by using a manually-controlled solenoid valve that allowed for quasi-instantaneous (<20 ms) shut off of the air flux.

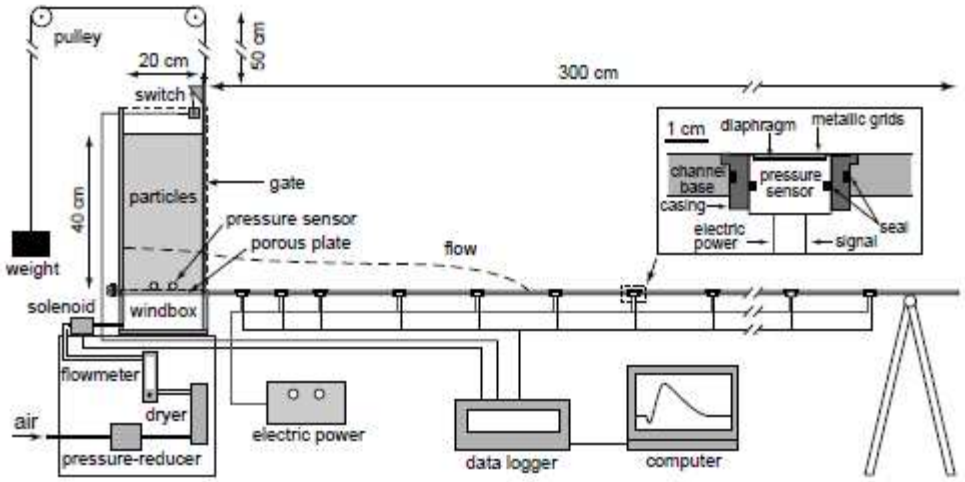

Figure 3.1. Experimental apparatus used in this study. Particles were placed in a reservoir, where they could be fluidized, and were released into a horizontal channel by means of a sluice gate. Sensors in the reservoir and in the channel, in horizontal and vertical position, respectively, allowed for non invasive measurement of the pore fluid pressure. The insert shows the casing in which the sensors were set, the distance between the diaphragm of the sensor and the grids being ~1 mm. See text for details.

Both the reservoir and the channel were equipped with pressure sensors located at various distances from the sluice gate, at one side of the reservoir at the lowermost position, and along the base of the channel. The pressure sensors, of piezoresistive type, were provided by ICSensors™ (model 154N). Their sensing package utilizes oil to transfer pressure from a stainless steel diaphragm to a sensing element having a frequency response of 1000 Hz. This

element allows for the measurement of both positive and negative pressure relative to that of the ambient atmosphere. The sensors could measure pressure in the standard range of ~6.9 kPa (1 psi) in the channel or ~34.5 kPa (5 psi) in the reservoir with a typical noise of 5-10 Pa and 15-25 Pa, respectively. They were set in an aluminium casing specially designed for the experiments, which allowed for non invasive measurement of the pore fluid pressure (see insert in Figure 3.1). The diaphragm of the sensors was as close as possible to the air-particle mixture, both being separated by superposed metallic grids sealed on the casing. Two crossed thin grids of 38 µm-aperture (smaller than the particles used) were in contact with the mixture and were supported by a thicker grid of 600 µm-aperture that ensured rigidity of the assemblage. Electric power was supplied to the sensors, and when pressure was applied on the diaphragm the sensing element delivered a voltage of 0 to ±100 mV that was sent to a data logger that sampled at a frequency of 100-1000 Hz. Then, the signal was sent to a computer and was converted into pressure values through a linear calibration law. The solenoid valve and the gate switch were also connected to the data logger in order to indicate when the air supply was turned off during defluidization tests on static beds and when the gate was lifted in dam break flow experiments, respectively.

The particles used were the same as those in a previous study on dam break granular flows by *Roche et al.* [2008], and were spherical glass beads of grain size range 60-90 µm (with a mean of 75 µm) and density ρ_s~2500 kg m^{-3}. The bulk density of the loosely packed granular column was $\rho_b \sim \rho_s(1-\varepsilon)=1450 \pm 50$ kg m^{-3}, thus indicating a pore volume fraction $\varepsilon \sim 0.42 \pm 0.02$. Concerning the fluidization processes when air was introduced vertically at the base of the column in the reservoir, the particles belonged to the group A as classified by *Geldart* [1973], (see also in *Rhodes* [1998]). For this type of particles, homogeneous expansion occurs over a range of air mean velocity, equivalent to the mean volumetric flow rate divided by the cross sectional area of the granular bed, between the minimum fluidization velocity (U_{mf}) and the minimum bubbling velocity ($U_{mb}>U_{mf}$). At U_{mf}, the bed is nearly fully supported as its weight is counterbalanced by the drag force generated by the interstitial air flow. In consequence, the pore fluid pressure approaches the maximum value given by Equation 3.4. Expansion of the granular network occurs at higher air velocity and is maximum at U_{mb}, above which air bubbles form. It is important to note that ash-rich matrices of pyroclastic flow deposits have a typical group-A behavior when fluidized [*Druitt et al.*, 2007], and the use of such type of particles in our experiments ensures the basis for dynamic similarity with the natural system. In complementary experiments, we used larger particles as markers at low volume fraction (< 10%) to visualize the internal flow kinematics, and these were either 700 µm-glass beads of density equal to ρ_s or 1-2 mm-plastic particles of density close to ρ_b.

Most flows were generated from the release of fluidized or dry (*i.e.*, non fluidized) granular columns having an initial loosely-packed height h_0=40 cm. We also performed complementary experiments at h_0=10-30 cm. For fluidized columns, experiments were carried out at U_{mf}=0.82 cm s^{-1} and U_{mb}=1.28-1.36 cm s^{-1}, at which the bulk expansion was nill and ~3-4%, respectively, and in both cases the initial pore fluid pressure was then $P \sim \rho_s(1-\varepsilon)gh_0$ (*i.e.*, Equation 3.4). We began acquisition of the pressure data in the reservoir and in the channel before gate opening. The flows were recorded in their entire length with a high-speed video camera through the lateral transparent side walls of the apparatus, at a rate of 100-250 frames per second. The videos were subsequently analyzed to determine the flow front kinematics and the flow height above the sensors as a function of time. When investigating the internal flow

kinematics, we considered a much smaller zone typically of length 10-30 cm. Such close up views were necessary in order to accurately capture the motion of the marker particles.

3.3 Results

3.3.1 General flow behavior

The kinematics of dam break granular flows was studied in detail by *Roche et al.* [2008]. The fundamental issues of their investigation are reported here because they will be referred to hereafter to discuss the results of the present study. Flows resulting from the release of granular columns of initial height h_0 and with a height-to-length ratio up to 3 propagated in three distinct phases, according to the kinematics of their front (see snapshots in Figure 2.4 [*Roche et al.*, 2008]). The distance and time at which transition between the phases occurred depended on the length scale h_0 and on the time scale $(h_0/g)^{1/2}$, respectively, the latter being proportional to the time scale of the column free fall. The flows first steadily accelerated or had a nearly constant (small) velocity as the column collapsed, before they entered into a second, constant (high) velocity phase. They then decelerated and stopped during a third (stopping) phase. For initially fluidized flows, the transition between the second and the third phase occurred when the difference in height between the collapsing column in the reservoir and the flow in the channel, thus generating a pressure gradient, had become negligible. An important observation was that granular flows generated from the collapse of slightly expanded (2.5-4.5 %) columns fluidized at U_{mb} behaved as inertial flows of water as their front velocity was close to that observed for such flows, $U_f \sim (2gh_0)^{1/2}$, until the beginning of the stopping phase, which occurred at ~65% and ~80% of the flow duration and runout, respectively.

In the present study, repetition of the experiments at h_0=40 cm showed good reproducibility, with runout (duration) of 102±2 cm (0.90±0.03 s), 187±3 cm (1.12±0.04 s), and 221±4 cm (1.28±0.04 s) for flows of dry material and those generated from columns fluidized at U_{mf} and U_{mb}, respectively. Most characteristics of flows with initial fluidization at U_{mf} were similar to those at U_{mb}, though flow duration and run out were a bit smaller, and because of that are not always presented in detail hereafter. The experiments carried out with markers revealed a basal deposit that formed behind a sliding head (where no deposition occurred), and whose upper surface aggraded upwards with time in the flow body (Figure 3.2). In consequence, the height of the overlying mobile part at a given location in the body decreased with time as the flow propagated into the channel, and the basal deposit took the form of a slender wedge. In the following sections, we report the characteristics of the flows and of their basal deposit, and then use the results to analyze and discuss the pore fluid pressure data.

3.3.2 Characteristics of the flows and of their basal deposit

Surface flow profiles were acquired from the video images and are shown in Figure 3.3a. In dry flows, the profiles are wedge shaped, with the height decreasing downstream at a given

time, and the surface slope is relatively steep except at the front. In contrast, initially fluidized flows spread much more as most of the material is evacuated from the reservoir. This leads to nearly flat profiles at late stages with a maximum height at the entrance of the channel. We note that for both types of flows some superficial motion occurs after the flow front has stopped. The distal limit of this motion migrates upstream and then stops at the rear of the reservoir or at the entrance of the channel in case of dry or initially fluidized flows, respectively. In dry flows, late avalanches result in a slight increase and decrease of the total flow height at the entrance of the channel and in the reservoir, respectively. In the reservoir, the surface slope then approaches the angle of repose of the material (~28°). In contrast, late superficial motion in initially fluidized flows does not modify the surface flow profile significantly. Figure 3.3b shows the total flow height as a function of time (*h*, in Figure 3.2) extracted from the surface flow profiles. The height in the reservoir decreases with time and remains larger or becomes smaller than that in the channel in case of dry and initially fluidized flows, respectively. In dry flows, the total height at a given location in the channel increases rapidly (in ~0.10-0.15 s) and remains thereafter approximately constant with time, though it increases slightly close to the reservoir gate because of late superficial avalanches. In contrast, in initially fluidized flows, the flow height rapidly increases to a maximum (in ~0.15-0.20 s), then decreases and finally slightly increases at late stages.

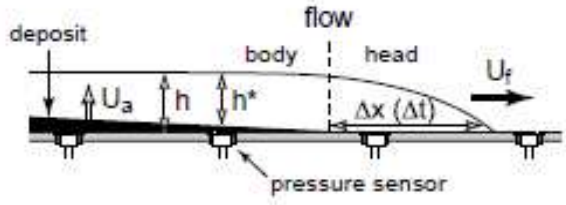

Figure 3.2. Structure of the flows in the channel (the vertical scale is exaggerated). The basal deposit (black) in the flow body forms behind the sliding head at a distance Δx (and time interval Δt) from the front that propagates at velocity U_f, and aggrades at a rate U_a. At a given location in the body, the height of the mobile part overlying the deposit (h^*), smaller than the total flow height (h), decreases with time.

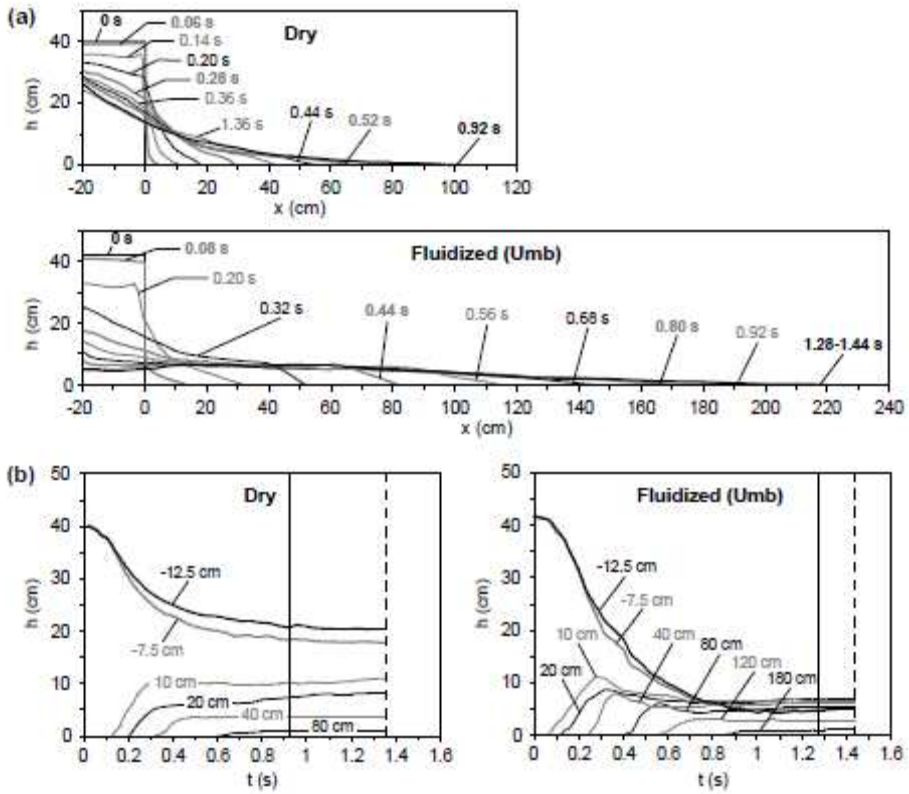

Figure 3.3. (a) Surface flow profiles as a function of time after release (see labels), for dry and initially fluidized (at U_{mb}) flows. The reservoir gate is at distance x=0. Thick black lines represent the initial column in the reservoir (at 0 s) and the profile when the flow front stops, the latter being at 0.92 s (dry) and 1.28 s (U_{mb}). Note that superficial motion occurs until 1.36 s (dry) and 1.44 s (U_{mb}). (b) Total flow height (h) as a function of time (t) after gate opening, extracted from the surface flow profiles in (a). Labels denote the distance from the reservoir gate. The vertical plain and dashed lines indicate the time at which the flow front stops and superficial motion ceases, respectively.

The internal velocity field of the flows was investigated from high-speed videos of the experiments involving markers. The trajectory of these markers was principally in the horizontal direction, except close to the reservoir in the upper portion of the flows and at the flow front. Figure 3.4 shows that both the flow head and body are pervasively sheared as the internal velocity increases upwards. We highlight that the lowermost part of the head slides over the channel base, whereas in the upper parts the internal velocity approaches the flow front velocity, such suggesting that drag and air entrainment on the upper free surface are negligible. In the body, the velocity is zero at the top of the basal deposit, and then increases upwards to a value significantly smaller than that of the front velocity. Note that velocities in the flow head higher than that in the body imply that the flows stretch during propagation. The shear rate in initially fluidized flows is smaller in the body than in the head, whereas it is approximately the same in both regions in dry flows. Although the shear rate just above the channel base and the top of the basal deposit might be larger [*i.e., Girolami et al.*, 2010], this could not be detected with the method we used. For initially fluidized flows, particles at the front came from the lower part of the initial column. A weak caterpillar effect was evidenced at late stages of emplacement, with

particles at the front overran by those located behind them and then incorporated into the basal part of the sliding head.

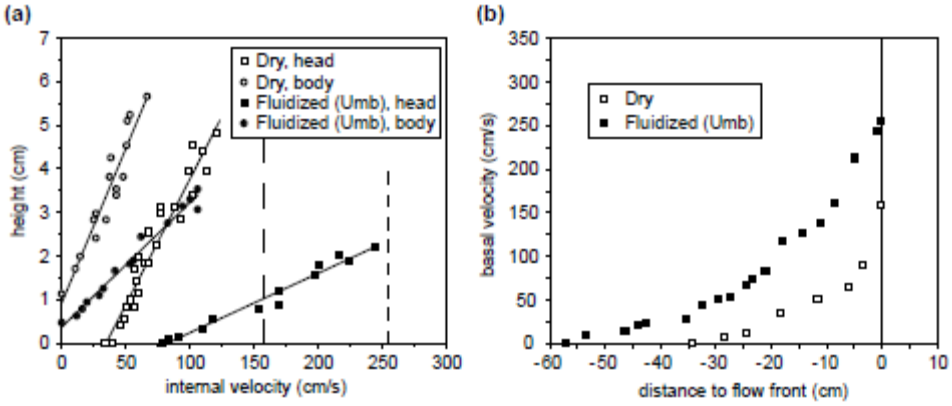

Figure 3.4. Internal horizontal velocity of the markers in the flows as a function of height. Measurements were made at a distance from the reservoir gate of one third and one half of the flow run out in dry and initially fluidized flows, respectively, approximately at half the length of the flow head and body, and during time intervals of ~0.02-0.04 s. Linear fits are assumed for simplicity. Non zero height at zero internal velocity in the flow body corresponds to the top of the basal deposit. Vertical lines denote the flow front velocity in dry (large-dashed) and initially fluidized (small-dashed) flows. The shear rate in the initially fluidized flow is ~74 s^{-1} (head) and ~35 s^{-1} (body), and in the dry flow is ~14-18 s^{-1}.

The characteristics of the basal deposits were investigated in detail in flows with markers (Figure 3.5). The video camera was located at various distances from the reservoir gate in the channel, and recordings were obtained by repeating the experiments, as permitted by their high reproducibility. We measured the thickness of the basal deposit, assuming that this corresponded to the distance between the channel base and the markers when their motion ceased. Figure 3.5a shows that the deposit aggradation begins ~0.2-0.3 s and ~0.2-0.4 s after the passage of the front in dry and initially fluidized flows, respectively, and that this time interval (Δt_{dep}) tend to decrease as the distance from the reservoir gate increases (see detailed data in Figure 3.7). The deposit thickness increases almost linearly with time, so that the aggradation velocity (U_a) can be determined by simply assuming a linear fit of the data. Figure 3.5b reveals that U_a is larger in dry flows than in initially fluidized ones, and varies slightly as the distance in the channel increases. In fact, U_a decreases from ~19 to ~16.5 cm s^{-1} in dry flows, whereas it first increases from ~6.5 to ~8.5 cm s^{-1} and then decreases to ~6.5 cm s^{-1} in initially fluidized ones. The thickness of the deposit (h_d) as a function of time (t) was then calculated from the observed onset of aggradation by assuming $h_d=U_a t$. Figures 3.5c-d show that h_d calculated is about equal to the measured total flow thickness when the flow front stops.

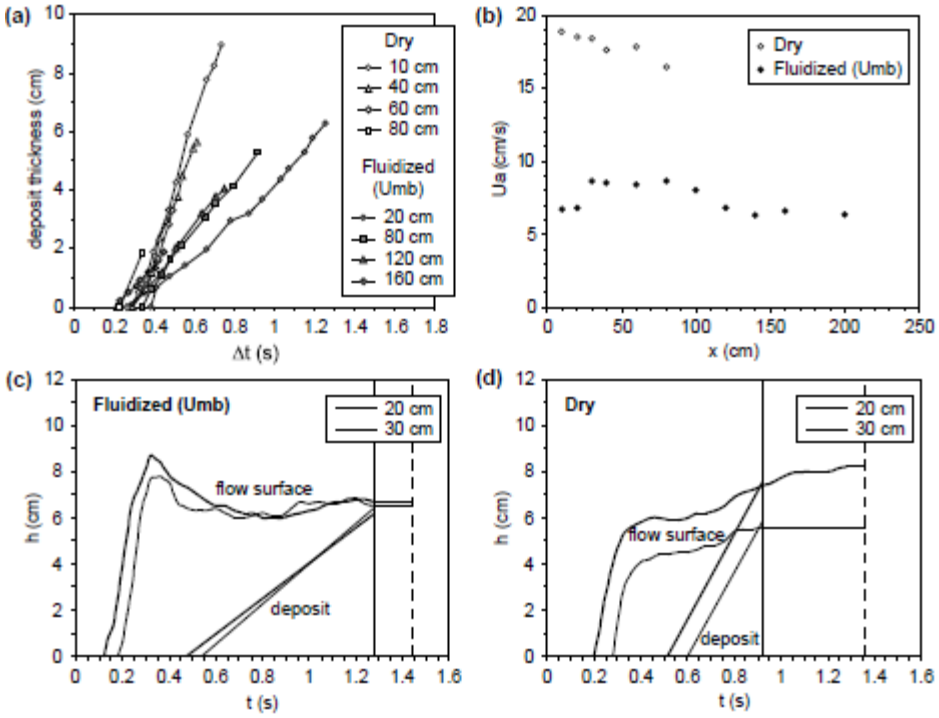

Figure 3.5. Characteristics of the basal deposits in dry and initially fluidized (at U_{mb}) flows. (a) Thickness of the basal deposit as a function of time, at various distances from the reservoir gate in the channel, where Δt=0 corresponds to the arrival of the flow front. Measurements were made at other locations but are not shown for clarity. (b) Mean aggradation velocity (U_a) of the basal deposit as a function of the distance from the reservoir gate (x), according to linear fit of the data in (a). In (a-b) error bars have about the size of the symbols and are not shown. (c-d) Observed total flow height (flow surface) taken from Figure 3.3, and calculated thickness of the deposit (h_d) as a function of time (gate opening at t=0) assuming $h_d=U_a t$, at 20 and 30 cm from the reservoir gate. The vertical solid and dashed lines indicate when the flow front stops and superficial motion ceases, respectively.

3.3.3 Pore fluid pressure in the flows

The pore fluid pressure data are presented in Figure 3.6. It is important to bear in mind that measurements were made relative to the ambient, at which P=0. Hence the terms underpressure or overpressure used hereafter means that the pressure is less or more than the atmospheric pressure, respectively. We report the pore pressure measured by the sensors, P, as well as the normalized pressure P/P_L and P/P_L*, with lithostatic terms P_L and P_L* defined as

$$P_L = \rho g h \tag{3.5}$$

and

$$P_L^* = \rho g h^*, \tag{3.6}$$

where ρ is the bulk density of the flow assumed to be equal to that of the initial column (ρ_b~1450 kg m^{-3}), h is the total flow height extracted from the surface flow profiles in Figure 3.3, and $h^*=h-h_d$ where $h_d=U_a t$ is the calculated thickness of the basal deposit taking into account the time interval Δt_{dep} between the passage of the front and the onset of deposition (*i.e.*, Figure 3.5). Regarding equation 3.6, we assume that the pressure increases from the flow surface to a maximum value at the top of the deposit and is then constant down to the base of the channel. Note that for fluidized columns in the reservoir $P_L^*=P_L$. For a few sensors, U_a and Δt_{dep} could not be determined accurately because of a lack of markers on the videos. In that case, we assumed a simple linear interpolation between values of these parameters measured at adjacent locations. Calculation of P_L^* was stopped as P/P_L^* (1) became negative as $h^*<0$ or (2) increased abruptly to very high values (~5-10) as h^* approached h because of the uncertainty in the measurement of h and on the estimate of h^*. We also report the flow front position in order to discuss the pore fluid pressure data in link with the phases of flow emplacement described in Section 3.1. As discussed below, the correlation between those phases and the pressure signals is good in most cases.

Figure 3.6. Pore fluid pressure in initially fluidized (at U_{mb}, left and U_{mf} ,middle) and dry flows (right, note that the vertical scales are different), generated from columns of loosely-packed height h_0=40 cm. The graphs show the measured pore pressure (P) where P=0 corresponds to the atmospheric pressure (a-c), and the ratios P/P_L (d-f) and P/P_L^* (g-i) as a function of time, t=0 indicating gate opening (small-dashed vertical line). Only positive pressure is considered for P/P_L and P/P_L^*. The location of the sensors is relative to the reservoir gate, so that values are negative in the reservoir and positive in the channel. Solid and large-dashed vertical lines indicate when the flow front stops and superficial motion ceases, respectively. Numbers in circle denote the collapse (1), constant velocity (2), and stopping (3) phases of flow emplacement, based on the kinematics of the front whose position (x) is reported (thick black curve, right scale), and their relative duration is indicated by small vertical dashed lines.

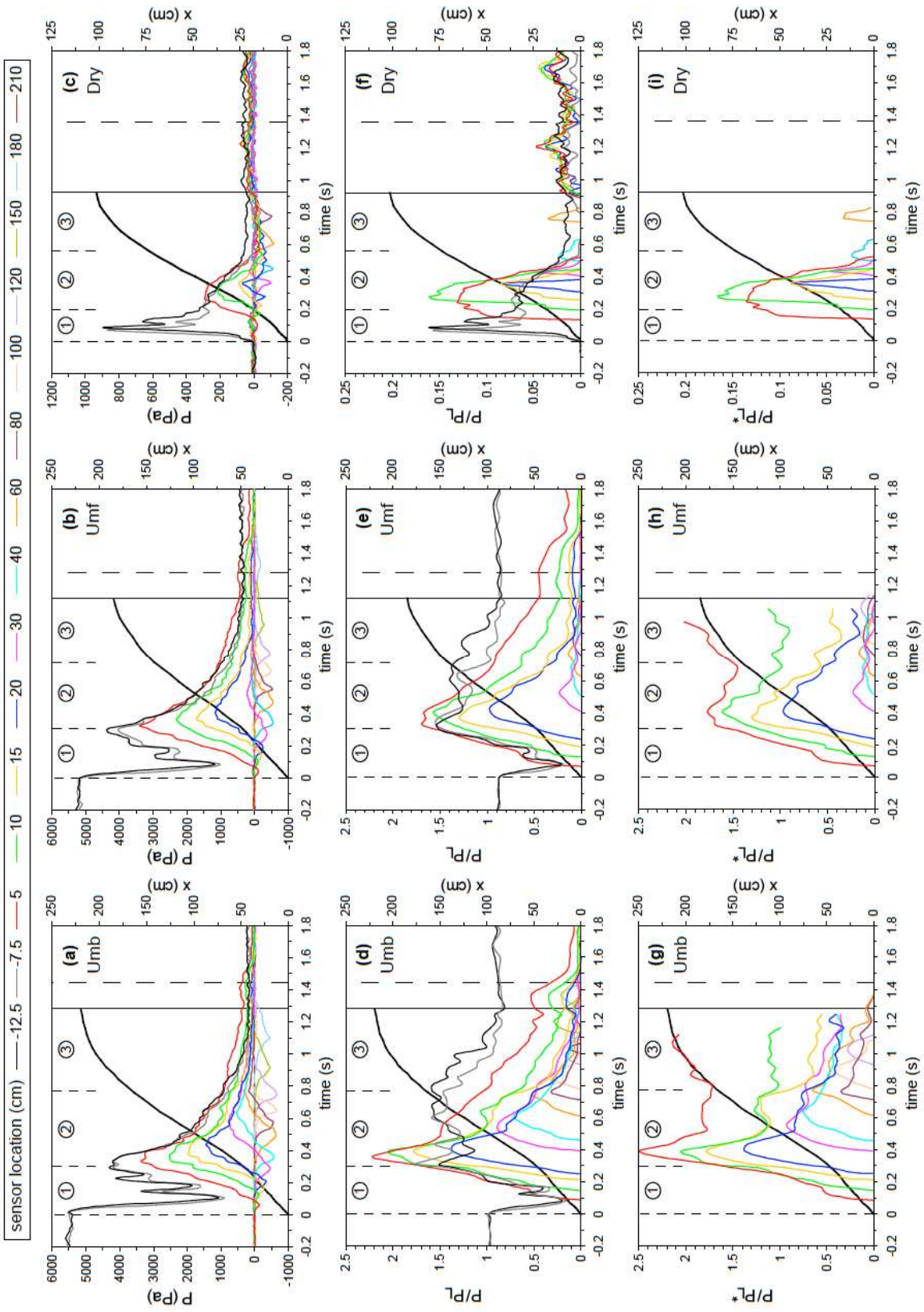
sensor location (cm)
-12.5
-7.5
-5
10
15
20
30
40
60
80
100
120
150
180
210
(a) Umb
(b) Umf
(c) Dry
(d) Umb
(e) Umf
(f) Dry
(g) Umb
(h) Umf
(i) Dry
P (Pa)
P/PL
P/PL*
x (cm)
time (s)
①
②
③

Figure 3.6

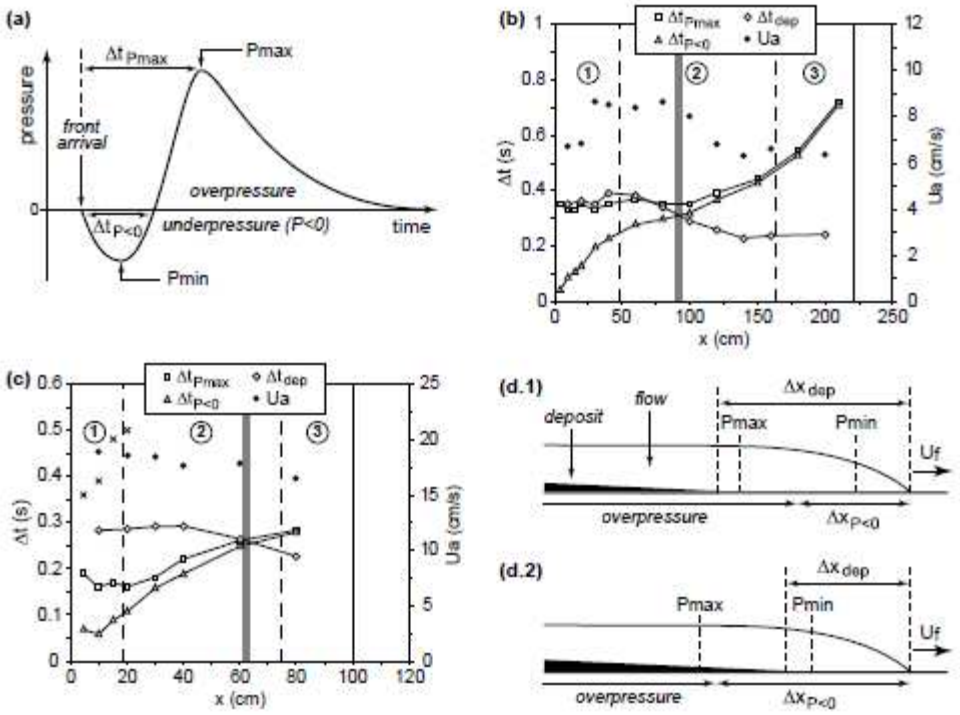

Figure 3.7. Characteristics of the pore fluid pressure data and of the basal deposits. (a) Typical pressure signal in the channel, showing successive stages of underpressure and overpressure. Zero pressure corresponds to atmospheric. (b-c) Variation as a function of the distance from the reservoir gate (x) of the duration of the underpressure stage ($\Delta t_{P<0}$), and of the time interval between the front arrival and the maximum pressure (Δt_{Pmax}) or the onset of deposit aggradation (Δt_{dep}), for (b) initially fluidized (at U_{mb}) and (c) dry flows. In (c), crosses indicate the duration of the second underpressure stage (see text for details). The deposit aggradation velocity (U_a) taken from Figure 3.5 is also shown (right scale). Numbers in circle denote the collapse (1), constant velocity (2), and stopping (3) phases of flow emplacement whose corresponding length is delimited by vertical dashed lines. The vertical solid line indicates the flow run out. (d) Interpretation of the internal flow structure from (b-c), when the flow front is at a distance shorter (d.1) or longer (d.2) than that indicated by the grey bar in (b-c). Horizontal arrows indicate corresponding lengths assuming $\Delta x = U_f \Delta t$, and vertical dashed lines show the location of P_{min} and P_{max}. Note that the underpressure zone can extend within that of the basal deposit (d.2), but P_{min} is still ahead the deposit.

For initially fluidized flows, the pore fluid pressure in the reservoir before gate opening (P~5500 Pa) indicates that nearly full bed support is achieved at U_{mb} (P/P_L~1) whereas ~90% of the weight is supported at U_{mf} (P/P_L~0.9) (Figure 3.6). Once the gate is lifted and the material enters into the channel, P rapidly drops to ~1000 Pa. Pressure then oscillates while increasing up to ~4500 Pa at the end of the first, collapse phase, and this maximum pressure is more than lithostatic as P/P_L~1.5. The ratio P/P_L then varies a bit until the beginning of the stopping phase, and then returns to ~0.9-1 when the flow front stops as the air flux still fluidizes the particles remained in the reservoir. At that stage, P at U_{mf} is larger than that at U_{mb} because the bed height is higher as less particles were evacuated from the reservoir, and waves at the surface of the fluidized bed then cause pressure oscillation in both cases. In the channel, the sensors reveal all

the same pressure signal pattern (Figure 3.7a). Deviation from atmospheric pressure is recorded as soon as the flow front arrives at the sensors, as confirmed by close examination of the videos and the front kinematic data in Figure 3.6. The pressure signal first reveals a negative, almost symmetrical stage (relative to the minimum value), followed by a positive, asymmetrical stage as the pressure rapidly increases to a maximum value and then slowly decreases. The duration of the underpressure stage increases at increasing distance from the gate, and the minimum pressure (P_{min}) is down to ~ -500 to -600 Pa and is correlated at a first order to the flow front velocity, U_f. We note that during the first phase of emplacement for h_0=40 cm (as in Figure 3.6), P_{min} varies while U_f is nearly constant. However, complementary experiments at lower h_0, for which U_f steadily increased during this first phase, showed that P_{min} was proportional to U_f. Positive pressure values for flows initially fluidized at U_{mf} are close to that of those fluidized at U_{mb} for sensors located up to 20 cm from the gate, and then are significantly smaller beyond. The maximum pressure (P_{max}) is less than that in the reservoir at the same time, and it decreases with distance. However, the pore pressure can be more than lithostatic close to the gate (at 5 to 20 cm) during the constant velocity phase as maximum P/P_L is larger than 1, and is similar to that (P/P_L~1.5, at U_{mf}) or larger than (P/P_L~2, at U_{mb}) in the reservoir. P/P_L* is larger than P/P_L at a given time after the onset of deposit aggradation, because h*<h, and remains high for most the sensors. An important result is that high pore pressure is maintained approximately until the beginning of the stopping phase. For instance in flows initially fluidized at U_{mb}, up to ~90%, ~75%, and ~65% of the weight of the flow overlying the basal deposit is supported at distances of 30, 40, and 60 cm, respectively. We highlight (1) that at the moment of maximum pore pressure, the flow front is located much further away in the channel than the corresponding sensor, that is at ~110 cm (sensor at 30 cm), ~130 cm (40 cm), and ~165 cm (60 cm), and (2) that the amount of weight supported would be even larger in case the bulk flow density would be smaller than that assumed (ρ_b~1450 kg m^{-3}) because of dilation of the air-particle mixture. Note that at a given time, the flows have a longitudinal pressure gradient as P/P_L* decreases with distance from the reservoir (Figure 3.8). When the flows decelerate during their stopping phase, P/P_L* decreases but the most distal sensors indicate that up to 25-40% (at U_{mb}) and 15-20% (at U_{mf}) of the weight of the particles is still supported. Pressure returns to atmospheric at the end of flow propagation, except for the most proximal sensor (at 5 cm), as air flowing from the reservoir is diverted sideways, so that the final deposit is still partially fluidized. Note that a slight pressure increase occurs for sensors close to the gate (5-20 cm) after the flow front has stopped due to late-stage superficial flow, and that very small amount of pressure is still present shortly after motion has totally ceased.

Interestingly, pore fluid pressure is also detected in initially dry flows, though it is much smaller than in initially fluidized ones. In the reservoir, P increases rapidly up to ~850 Pa during the collapse phase as most the material above the sensors is in motion, showing that at least ~16% of the weight of the column is supported. The pressure then steadily decreases, though some slight fluctuation occurs after the peak value. Very small residual pressure corresponding to only ~1-2 % of the weight of the collapsed column is measured at the latest stages and even after motion has completely ceased. In the channel, the pressure signal has the same characteristics as for initially fluidized flows, though it is weaker, as it reveals successive underpressure and overpressure stages. P_{min} decreases as the flow front velocity increases during the collapse phase, and P_{max} decreases with the distance from the gate. Values of P/P_L similar to that in the reservoir at early stages (~0.13-0.16) are measured at the entrance of the channel (at 5-10 cm) at the beginning of the constant velocity phase. We note that close to the gate (at 5-20 cm), (1)

overpressure may be followed by a second underpressure stage that appears approximately at the onset of basal deposition and whose minimum value is close to that of the first one and (2) that some very small residual pore pressure similar to that in the reservoir is measured after the flow has stopped.

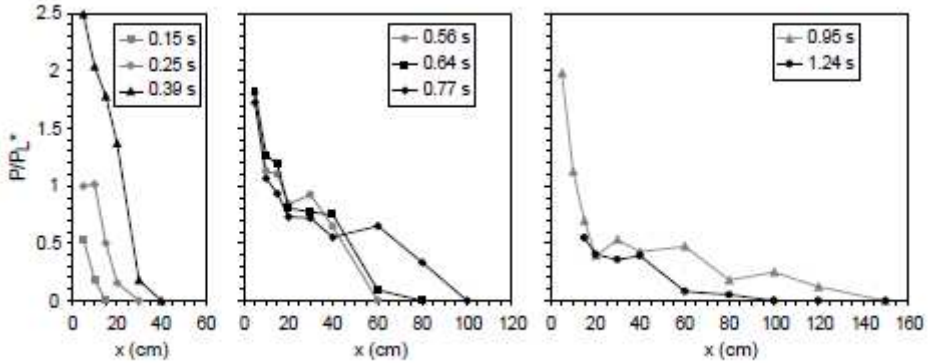

Figure 3.8. Lateral pressure gradient at different times after release in the initially fluidized (at U_{mb}) flow whose data are presented in detail in Figure 3.6. The pressure ratio P/P_L* decreases as the distance in the channel (x) increases. Note that pressure is more than lithostatic (P/P_L*>1) at early stages and/or close to the reservoir gate (at x=0).

The detailed characteristics of the pressure signals are reported in Figure 3.7. They reveal variations similar to that of the deposits at increasing distance from the reservoir gate, and a transition occurs during the constant velocity phase. Before the transition (grey bar in Figures 3.7b-c), the time interval between the front arrival and (1) the maximum overpressure (Δt_{Pmax}) or (2) the onset of deposit aggradation (Δt_{dep}) varies slightly and is larger than the duration of the underpressure stage ($\Delta t_{P<0}$), which increases almost steadily. Transition occurs when these time intervals are almost equal to $\Delta t_{P<0}$, whose rate of change then decreases. Beyond the transition, for initially fluidized flows, $\Delta t_{Pmax} \sim \Delta t_{P<0}$ and both increase, whereas Δt_{dep} varies similarly to the deposit aggradation velocity as it decreases slightly with distance. At that stage, evolution of the time intervals in dry flows is less clear. These results imply that the basal deposit begins to aggrade behind both the location of P_{max} and the zone of underpressure at early stages of propagation (Figure 3.7d.1), whereas it aggrades ahead of P_{max} and within the underpressure zone at later stages (Figure 3.7d.2). Note that the length of the sliding head does not vary much until the stopping phase. This shows that the tip of the basal deposit migrates downstream, as the particles sediment from the flow body, at a velocity close to that of the flow front.

3.3.4 Comparison with defluidization of static beds

Initially fluidized flows basically defluidize while they propagate in the channel. In order to investigate the defluidization processes, we performed experiments on static columns in the reservoir with the gate closed and made comparison of their defluidization timescale with that of the flows. The aim of these tests was to assess if the flows deaerate accordingly to the simple configuration of a static column or if other processes may act. Experiments consisted of columns

of various heights fluidized at U_{mf} and U_{mb}, then the air supply was turned off instantaneously using the solenoid valve and the pressure was recorded by the sensors in the reservoir. At U_{mb}, this corresponded to a bed collapse test [*Geldart and Wong*, 1985; *Druitt et al.*, 2007].

Comparison of the flows and the static columns defluidization timescales is not straightforward for the following reasons. (1) The flow height varies spatially and temporarily whereas columns in the reservoir have a constant height (neglecting the small initial expansion at U_{mb}). For simplicity, we have considered the nearly constant flow height (h~6 cm) observed during the dominant constant velocity phase (see Figure 3.3) and we made comparisons with experiments on static columns of similar heights. (2) The pore fluid pressure in the flows can be more than lithostatic close to the reservoir (see Figure 3.6). (3) The weight of a fluidized static column is not entirely supported at small height typically <20 cm, possibly because of heterogeneities caused by air flow channeling [*Gilbertson et al.*, 2008]. In consequence, the initial normalized pore pressure for the small static columns investigated was less than for the 40 cm-high columns used to generate the flows. (4) Deposit aggradation occurs in the flows, but not in static columns initially fluidized at U_{mf} because of the negligible expansion of these columns; furthermore, onset of aggradation in the flows occurs after a significant time interval following the passage of the front, whereas a deposit forms immediately in static columns fluidized at U_{mb} once air flux is no longer supplied.

Figure 3.9 shows P/P_L as a function of time in defluidizing static columns, and the data are compared to that of the flows taken from Figure 3.6. Results are reported for a range of column height H=4-8 cm including the nearly constant flow height (~6 cm) observed during the dominant constant velocity phase. As mentioned above, P/P_L for small static columns before the air supply is turned off decreases as the column height decreases and it is equal to ~0.78-0.88 at U_{mb} and ~0.70-0.82 at U_{mf}, a bit less than for the higher columns used in flow experiments (see Figure 3.6). The duration of complete defluidization of the static columns is close to that of the flow and, as expected, increases with the column height as the pore pressure diffusion timescale is proportional to H^2/D. Note that in the case of initially expanded columns fluidized at U_{mb}, the rate of pressure decrease depends both on pressure diffusion and on bed contraction related to particle settling. As a consequence, for a given column height, P/P_L at a given time as well as the duration of defluidization are larger in columns initially fluidized at U_{mb} than in those fluidized at U_{mf}. Considering a column and flow height of 6 cm, we highlight that at a given time P/P_L in the flow during its constant velocity and stopping phases is higher than in the static column, and it is even up to about twice that in the column in case of initial fluidization at U_{mb}.

3.4 Discussion

3.4.1 Origins of the pressure signals

i) Causes of underpressure at the flow head

We now discuss the possible mechanisms that are likely to explain the characteristics of the pressure signals measured in the experiments, and these are summarized in Figure 3.10. We first address the origin of the underpressure (i.e., pressure less than atmospheric) in the channel, measured as soon as the flow front arrives at the sensors. Underpressure relative to the ambient at the flow head has already been measured in experimental debris flows [*Iverson*, 1997], and in air-particle mixtures including natural snow avalanches [*McElwaine and Turnbull*, 2005] as well as experimental flows such as large-scale ping-pong ball avalanches [*McElwaine and Nishimura*, 2001] and small-scale laboratory gravity currents on steep slopes [*Turnbull and McElwaine*, 2008 and 2009].

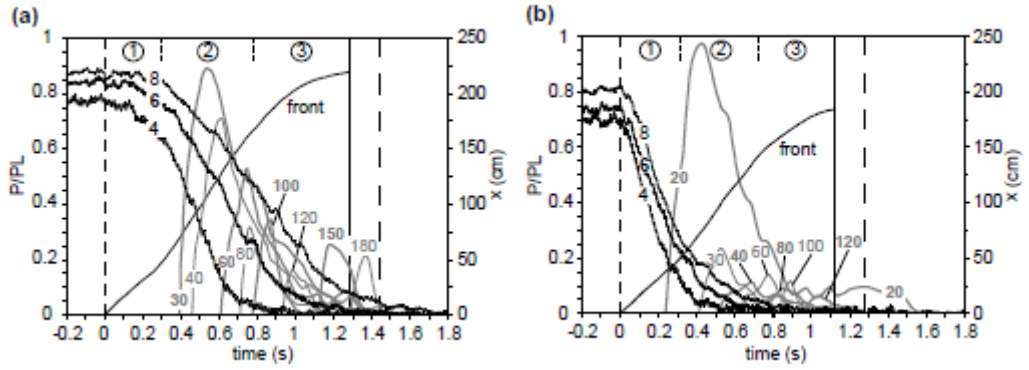

Figure 3.9. P/P_L as a function of time for granular columns initially fluidized at (a) U_{mb} or (b) U_{mf}, for static columns in defluidization tests (black) and for flows (grey, data from Figure 3.6 at $P/P_L<1$). Indices denote the height of the loosely packed static columns (black, in cm) and the sensor location in the channel for flow experiments (grey, in cm). The flow front position is also shown (x, right scale), and numbers in circle denote the collapse (1), constant velocity (2), and stopping (3) phases of flow emplacement whose duration is indicated by small vertical dashed lines. The vertical solid lines point out when the flow front stops, and vertical dashed lines designate the moment the solenoid valve is turned off (static beds) or the reservoir gate is open (flows) at t=0 and when superficial flow motion ceases at late stages. Measurements for static columns were made with sensors measuring pressure in the range of ~34.5 kPa (5 psi) and at high sampling frequency (600-800 Hz), thus explaining the noisy aspect of the curves.

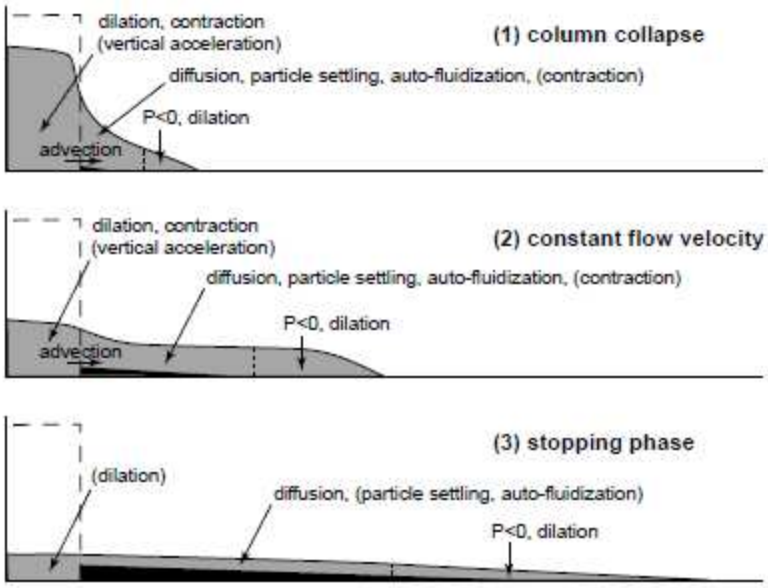

Figure 3.10. Mechanisms accounting for the pore pressure measured in initially fluidized flows, with second order processes in brackets. The small vertical dashed line separates the zones of underpressure at the flow head, where $P<0$ denotes the mechanism proposed by *McElwaine* [2005] (see text for details), and of overpressure in the body whose basal deposit is shown (black). The processes acting in initially dry flows are auto-fluidization and $P<0$.

McElwaine [2005] developed a model, based on Bernoulli's theorem, for an inviscid gravity current down an incline. The model gives solution for the fluid pressure along the substrate, ahead of the current front and at the base of the current head (see Figure 3 in *McElwaine* [2005]). First, ambient air pressure is positive ahead of the current and increases to a maximum equal to $\rho_a u^2/2$ at the front, where ρ_a is the air density and u is the air velocity assumed to be equal to that of the front. In our experiments, this positive pressure was of the order of 1 Pa, and could not be detected with the sensors used. Second, air pressure at the base of the current head decreases with distance behind the front and may become negative, so that

$$P = \frac{1}{2}\rho_a u^2\left(1-\frac{\kappa r}{R}\right) + 2g(\rho-\rho_a)r\sin\left(\frac{\phi}{2}\right)\cos\left(\theta+\frac{\phi}{2}\right), \qquad (3.7)$$

where R is the effective length of the current (aerodynamic flow radius), $r=(t_0-t)U$ is the distance from the front where t_0 is the moment the front arrives at the sensor and U is the flow velocity, g is gravity acceleration, ρ is the (bulk) flow density, ϕ is the front angle with the substratum, θ is the slope of the incline, and κ is a constant ≈1.01. Behind the effective length, it is assumed that the pressure returns to zero. In our case, $\theta=0$ and the first term in equation 3.7 is negligible for R being of the order of the flow height, so that equation 3.7 becomes

$$P \approx g(\rho-\rho_a)(t_0-t)U\sin(\phi)\,. \qquad (3.8)$$

Note that t_0-t<0, and that P has the same dimension as $(\rho-\rho_a)U^2$.

Figure 3.11 shows the underpressure measured during the constant velocity phase of our experimental flows. As mentioned already, the minimum pressure P_{min} is approximately constant during that phase. In detail, however, P_{min} in initially fluidized flows slightly decreases (at U_{mb}) or increases (at U_{mf}) when the distance increases. In order to match P_{min} in the experiments, we calculated the theoretical pressure with Equation 3.8, from t_0 (at P=0) to the time of P_{min}, so that the parameters to be fitted were the flow density (ρ) and the flow velocity (U). There are, however, limitations regarding the applicability of the model to our experiments. The structure of the experimental flows close to the front could be different from that assumed in the model. The value of P_{min} was fitted at a distance r larger than the effective length, so that calculation was strictly valid only at early stages of underpressure. Furthermore, we also addressed the initially dry flows though the model does not strictly apply to them. Note that underpressure may also result from other processes, as discussed at the end of this section as well as in section 4.1.3.

We calculated the flow parameters required to fit P_{min} with Equation 3.8 by considering the front angles observed in our experiments, which decreased with the distance travelled (Figure 3.3, Table 3.1). Firstly, we assumed that U in Equation 3.8 was equal to U_f observed in experiments, and obtained bulk flow density values much less than ρ_b~1450 kg m^{-3} (Table 1). This implies very high degrees of homogeneous expansion of the mixtures of at least ~70-200% (initially fluidized flows) and ~220-280% (dry flows), which is evidently not true from observation of the videos. Secondly, we calculated U required to fit P_{min} assuming that the flow density was equal to that of the initial mixture ρ_b (ρ=1450 kg m^{-3}) (Table 1). In that case, values of U are smaller than U_f. Interestingly, U is about one third to one half U_f, as shown also in Figure 3.4 for the middle part of the sliding head, approximately where P_{min} is generated. We point out that the normalized pressure $-P_{min}/\rho U^2$ is then about two times smaller in dry flows than in initially fluidized ones (Table 1). All else being equal, this might reflect contrasting degrees of fluidization of the head of both types of flows, and in turn implies that the head of the initially fluidized flows remained at least partially fluidized. In summary, bearing in mind the limitations of applicability of the model to our experiments, the above analysis suggests that the sliding head of the flows had a particle concentration close to that of the initial mixture and generated underpressure according to *McElwaine*'s [2005] model, as long as we accept the required values for the flow velocity U at the base of the sliding head. There are uncertainties regarding the degree of fluidization of the head during the constant front velocity phase, but this remained probably close to that of the initial column before release. Though the amount of underpressure appeared to be controlled by this degree of fluidization, it depended primarily on the basal flow velocity. In this context, the decrease of P_{min} while the flow front velocity was constant during the early collapse phase of the initially fluidized flows at h_0=40 cm (Figure 3.6) may reflect an increasing basal velocity. Note also that sliding of the granular material above the nose of the basal deposit may also explain (1) the second underpressure stage measured in the body of the dry flows at the entrance of the channel and (2) why the underpressure zone in the initially fluidized flows extends behind the tip of the deposit at late stages of emplacement.

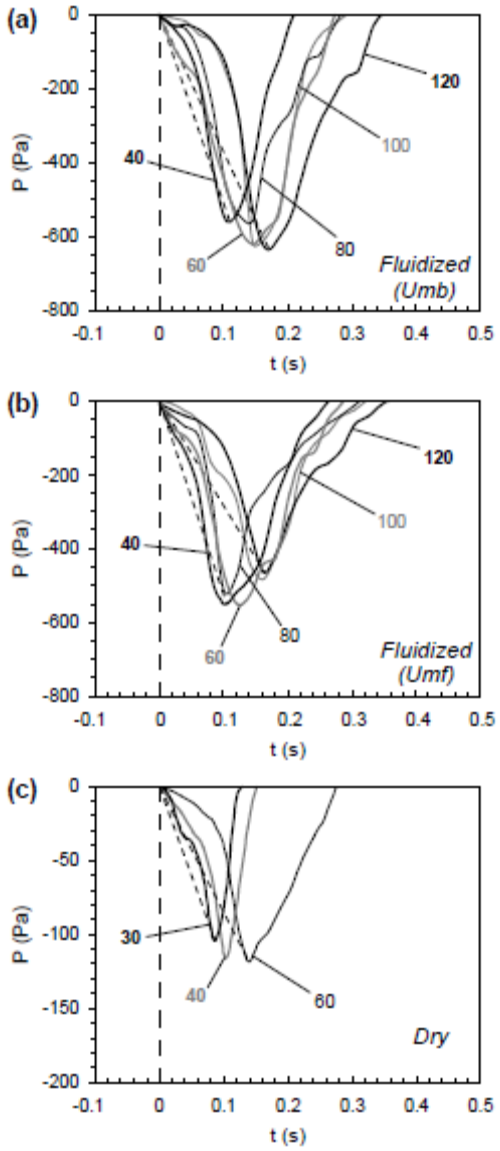

Figure 3.11. Underpressure measured in the channel during the constant velocity phase of flows initially fluidized at U_{mb} (a) or U_{mf} (b), and of dry flows (c). The data are from Figure 3.6. Pressure (P) is shown as a function of time (t), and t=0 indicates arrival of the flow front at the sensors. Indices denote the distance (in cm) of the sensors from the reservoir gate. The thin dashed lines are the model from Equation 3.8 that fit P_{min}, for the most proximal and distal sensors considered. See text for details.

Table 3.1. Characteristics of the flows and values of the bulk flow density ρ and flow velocity U required to fit P_{min} using Equation 3.8.

Initial condition	Umb		Umf		Dry	
Sensor location, (cm)	40	120	40	120	30	60
ϕ, (deg)	25	10	25	10	12	7
[(a)] ρ, (kg m^{-3})	490	868	562	744	380	453
[(b)] U, (cm s^{-1})	90	153	88	116	42	63
[(b)] U/U_f	0.35	0.60	0.39	0.51	0.26	0.39
[(b)] $-P_{min}/\rho U^2$	0.06	0.07	0.06	0.07	0.03	0.03

[(a)] $U=U_f$, [(b)] ρ =1450 kg m^{-3}.

Underpressure at the flow head could be generated by other mechanisms. It could result from the presence of a boundary layer at the base of the flows that we could not detect. Dilation at the flow head with particles and interstitial air moving relatively upwards and downwards, respectively, thus generating drag, could be another mechanism to generate underpressure. However, assuming this is the only active process, this would correspond to a rather complex structure of the flow head. Dilation would increase from the front, would be maximum about where P_{min} is generated, and then would decrease behind. By simply assuming that the dilating mixture behaves similarly to a fluidized bed, for which the pore fluid pressure varies linearly with the interstitial air velocity, then the maximum air-particle relative velocity is $U_r=(P_{min}U_{mf})/P$, where P is the pore pressure in a bed of given height h fluidized at U_{mf}. Taking into account the flow height and P_{min} measured in the experiments, then U_r (at P_{min}) is ~0.4-0.6 cm s^{-1} and ~0.1-0.2 cm s^{-1} in initially fluidized and dry flows, respectively, which appear as possible values according to the flow dimensions and velocities. Dilation could act along with sliding as described in the previous paragraph, and U_r would then be smaller than indicated just above. The effects of dilation of the mixture without differential motion between the solid and fluid phases are considered in section 4.1.3.

ii) Causes of overpressure in the flow body

The positive pressure (*i.e.*, more than atmospheric) measured in the body of the initially fluidized flows, without any air supply from the substrate, primarily derives from advection of the initial pore pressure generated in the reservoir. In the channel, the decrease of P_{max} as the distance from the reservoir increases and of the pore pressure with time after P_{max} at a given location both suggest that pore pressure diffusion is a fundamental process until the flows are completely defluidized and stop. Diffusion is relatively slow compared with advection, because at the entrance of the channel pore pressure in the flows generated from the base of the thicker fluidized columns remains close to that in the reservoir (Figure 3.6) and is then larger than lithostatic (Figure 3.12). Note that pressure in the reservoir can be larger than lithostatic, and this is discussed in section 4.1.3. In slightly expanded mixtures, settling of the particles also acts opposite to pressure diffusion because it generates pore pressure and hence increases the defluidization timescale, as mentioned earlier for static columns (Figure 3.9). This occurs readily in flows initially fluidized at U_{mb}, but may happen as well in other types of flows provided they

experience sufficient expansion during emplacement. Particle settling might generate overpressure in dry flows, but these, however, are initially not expanded and can only experience Reynolds dilation.

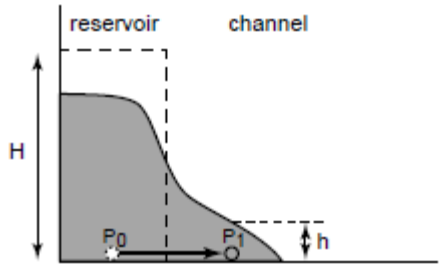

Figure 3.12. Advection of the pore fluid pressure from the reservoir to the channel (horizontal arrow). The pressure in the initially fluidized column is $P_0=\rho_b gH$. If the timescale of pressure diffusion is large compared with that of advection, then pressure in the flow can be more than lithostatic as $P_1 \sim \rho_b gH > \rho_b gh$.

Overpressure in the initially dry flows is an important observation. This suggests that viscous drag is induced by differential motion between the unsteady particles and the interstitial air during bulk movement of the mixture. This dynamic, motion-induced pore pressure arises at early stages as the flowing granular material is sheared. It is more important in the reservoir and at the entrance of the channel, where at least up to ~16% of the weight of the particles is supported, and is smaller further away probably because of less efficient air-particle interactions. We point out that a dimensional analysis of experiments similar to those presented in this paper showed that strong viscous air-particle interactions can develop in these internally sheared flows, thus promoting at least partial support of the weight of the particles [*Roche et al.*, 2008]. This phenomenon will be referred to auto-fluidization hereafter for convenience though we acknowledge that full bed support is not achieved. We highlight that auto-fluidization of our air-particle flows has an internal origin and does not require any external fluidizing gas. This is similar to the model of *Huang et al.* [2009] for granular flows sheared in rotating drums and that can be fluidized by internal cycling air. In contrast, this differs from the conclusion of *Bareschino et al.* [2008] for flows in rotating drums invoking air ingestion at the front through plunging avalanches. Note that auto-fluidization is likely to occur in initially fluidized flows as well, at an amount at least equivalent to that in dry flows, and this would contribute to generate high pore fluid pressure along with the other mechanisms described in this paper. This may explain why the pore pressure in the flows is larger than in defluidizing static columns of equivalent height at given time (Figure 3.9), though comparison between the dynamic and static cases is not straightforward as discussed in section 3.4.

iii) Voidage variation of the fluidized air-particle mixture

We now consider the influence of dilation and contraction of the air-particle mixture on the pore fluid pressure. The following better applies to fluidized mixtures, *i.e.* for which stresses are readily transmitted by the fluid phase. The perfect gas law indicates that PV/T is constant for

a constant mass of gas, where P, V, and T are the pressure, volume, and temperature of air, respectively. Assuming that T is constant, then

$$P_2 = P_1 \frac{V_1}{V_2}, \tag{3.9}$$

where indices denote two successive stages. We note from Equation 3.9 that 1% dilation (contraction) of a fluidized air-particle mixture at pressure about equal to that of the ambient atmosphere, so that $P_1 \sim 10^5$ Pa, causes a pressure decrease (increase) of ~1000 Pa. In case of dilation of the mixture, the internal air pressure decreases as the ambient cannot supply sufficient new air to compensate the pressure drop inside the flow. Variation of the voidage of the air-particle mixture may occur both in the reservoir once the column is released and in the subsequent flows.

In the flows, dilation could generate underpressure at the flow head, and P_{min} measured would correspond (assuming pressure decrease from P=0) to a dilation of ~0.5-0.6 % and ~0.1% in initially fluidized and dry flows, respectively. Note that the second underpressure stage measured in dry flows would be compatible with an equivalent amount of dilation of the granular material flowing above the nose of the basal deposit. In case underpressure at the head would also be generated by the process proposed by *McElwaine* [2005] (section 4.1.1), then the amount of dilation would be smaller than indicated above. Generation of underpressure through dilation, however, would require a rather complex structure of the flow head in terms of degree of dilation, as mentioned in section 4.1.1. Furthermore, we highlight that underpressure measured at the head of debris flows [*e.g.*, *Iverson*, 1997] appears to be incompatible with the low compressibility of the interstitial water if one assumes a pressure decrease through dilation.

Pressure variations measured at the base of the fluidized columns in the reservoir can be explained by successive dilation and contraction stages of the air-particle mixture (Figure 3.10). Once the column is released, dilation may occur readily as the mixture stretches when the flow enters the channel and/or as pressure at the base of the column tend to equilibrate with the lower atmospheric pressure. In this context, the sudden pressure decrease of ~4500 Pa right after gate opening in columns fluidized at U_{mb} and U_{mf} (Figure 3.6) indicates dilation of ~4.5 %, so that the total expansion at U_{mb} relative to the initial loosely packed state is ~7.5-8.5 %. Then, the following pressure increase up to values that can be larger than lithostatic at the end of the collapse phase may be generated by two means: (1) the acceleration of the falling particles within the reservoir, and (2) a contraction of the mixture, and successive transient stages of slight dilation and contraction would account for the pressure oscillations observed. In case (1), as the gate is open and the whole granular mass falls under the influence of gravity, then the basal pore pressure counterbalances the weight of the particles (as before release) plus the force related to their acceleration. The excess pore pressure generated is then $P_e = \rho U_c^2$, where U_c is the vertical velocity of the collapsing column ~80-85 cm s^{-1}, so that $P_e \sim 1000$ Pa. This, however, is insufficient to account for the pressure measured at the end of the collapse phase. In case (2), at both U_{mb} and U_{mf}, P-P_L is ~1500 Pa (as $P/P_L \sim 1.5$) at the end of the collapse phase when the reservoir is about half emptied. Taking into account the possible excess pressure of ~1000 Pa caused by vertical motion of the mixture, the difference of ~500 Pa indicates a contraction of ~0.5 % compared to the initial static fluidized state before release (in case no excess pore

pressure would be generated by column collapse, then contraction would be only ~1 % more). This means that the packing at U_{mf} is then slightly larger than the loose packing of the initial column, which is plausible as loose granular beds can compact by a few percents when subjected to external forcing [*Duran*, 1999]. In contrast, beds fluidized at U_{mb} are still slightly expanded, at an amount of ~2.5-3.5 %. In summary, to explain the pressure increase following the initial decrease in the reservoir during the column collapse phase, we favor contraction of the air-particle mixture possibly combined with its vertical acceleration. Interestingly, at both U_{mb} and U_{mf}, slight dilation related to the sudden acceleration of the flows when they enter the second, constant flow velocity phase can explain why P/P_L slightly decreases at that stage. Then, at U_{mb}, contraction of the mixture as the granular column terminates to collapse can account for the slight increase of P/P_L during that constant velocity phase, and pressure returns to lithostatic as the mixtures reacquires its initial voidage during the last, stopping phase. Note that this effect is less pronounced in columns fluidized at U_{mf}, for which contraction is more difficult to achieve because of their initial non expanded state.

In the case of the initially dry flows, the sudden pressure increase of ~800 Pa in the reservoir right after gate opening could suggest a contraction of ~0.8 %. However, as the granular column is initially not fluidized nor expanded, a pressure increase through voidage reduction is probably difficult to achieve. Furthermore, the mixture is rather expected to dilate once in motion. In consequence, auto-fluidization as described in the previous section better explains the positive pressure generated. Nevertheless, voidage variation could cause the small pressure fluctuations measured once the granular material is partially fluidized during flow emplacement.

3.4.2 Implications for geophysical flows

Our experimental study applies to dense (or the dense part of) subaerial geophysical flows propagating on a subhorizontal slope, and particularly to cases where fluid-particle interactions at initial stages are strong enough to generate a fluidized mixture with high pore fluid pressure. The experiments are relevant to flows rich in fine particles, which, regarding the type of air fluidization processes, belong to the *Geldart* [1973] group A. In the volcanological context, these conditions are readily achieved in ash-rich pyroclastic flows as a fluidized mixture of gas and particles is emitted at the eruptive vent. The flows then basically defluidize as they propagate, though local and transient gas supply may be provided from either internal or external sources. Note that particle aggregation and temperature-derived buoyancy were negligible in the experiments, unlike to what it may happen for pyroclastic flows in nature. These experiments may also apply to other types of flows such as dense snow avalanches [*Bartelt et al.*, 1999], as these may be fluidized by air entrainment at the front as the air-snow mixture is relatively dilute during initial acceleration on steep slopes [*Rastello and Hopfinger*, 2004; *Turnbull and McElwaine*, 2007]. Uncertainties, however, concern the type of air fluidization processes of snow particles, and aggregation of these particles then forming a coherent plug may complicate this simple picture [*Salm*, 1993]. The pore fluid pressure and internal kinematic data reported in this study give insights into the structure of these geophysical flows. These may consist of a (at least) partially fluidized sliding head generating underpressure, followed by an almost fully fluidized body at the base of which a deposit forms and aggrades upwards at a nearly constant rate, and both the head and body are sheared pervasively (Figure 3.13). As the flow basically defluidizes

during transport, the degree of fluidization at a given time is expected to decrease from the source, provided auto-fluidization is not efficient enough.

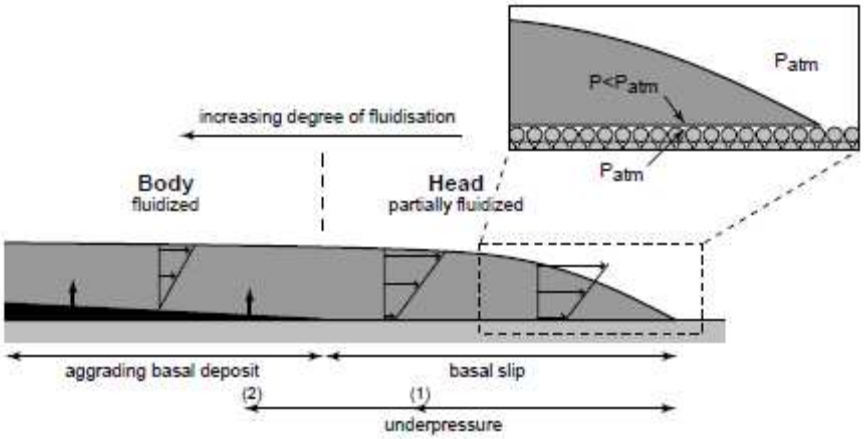

Figure 3.13. Structure of a geophysical flow inferred from the present study. Horizontal and vertical arrows in the flow head and body indicate the internal velocity and aggradation of the basal deposit (black), respectively. Numbers denote the shift of the rear limit of the underpressure zone at early (1) and late (2) stages. In the latter case, this zone extends towards the distal part of the deposit. The insert is the sketch of the head passing over a substrate consisting of an unconsolidated granular material (circles), not to scale. Pressure in the pores of the substrate is that of the ambient atmosphere (P_{atm}), and underpressure ($P<P_{atm}$) at the base of the sliding head generates an upward-directed pressure gradient.

Regarding pyroclastic flows, the experimental results are consistent with several field observations. Sliding and associated shear at the base of the flow head may generate erosion features, as discussed also by *Girolami et al.* [2010]. This is likely to occur if large lithic clasts segregate in the lowermost part of the flow [*Druitt and Sparks*, 1982; *Sparks et al.*, 1997; *Pittari and Cas*, 2004] and are dragged by the (partially) fluidized ash matrix [*Dufek and Bergantz*, 2007a and 2007b; *Dufek et al.*, 2009; *Roche et al.*, 2005], or when the flow has acquired a frictional behavior once defluidized at late stages. In case of a substrate consisting of an unconsolidated loose granular material, underpressure relative to the ambient atmosphere at the base of the head may cause an upward-directed pressure gradient, provided atmospheric pressure is maintained in the pores of the substrate as the latter is overlain by the flow (Figure 3.13). This, along with basal shear (if strong enough), may act as an efficient mechanism to entrain loose material from the ground. Substrate-derived clasts are often encountered in pyroclastic flow deposits and may be the witness of such a process. For example, slabs of pumice fall deposits a few tens of centimeters-thick can be incorporated into overlying pyroclastic flow deposits [*Druitt and Sparks*, 1982, their figure 3.8]. More generally, accidental substrate-derived clasts could be incorporated into the flow head, possibly contributing to form the (ground) layer 1 observed in many deposits [*Wilson*, 1986]. The mechanism for clasts incorporation we discuss here is an alternative to the proposed turbulent boundary layer at the flow base induced by surface roughness of the substrate [*Buesch*, 1992] or to the sudden flow acceleration on local steep slope [*Suzuki-Kamata*, 1998]. As experiments showed that the rear limit of the underpressure zone migrated to the basal deposit at late stages of emplacement, particles deposited from the flow

body might be reworked if a sufficient pressure gradient developed. Neglecting this process, the data of *Girolami et al*. [2010] as well as those reported in the present study suggest that the basal deposit in the body may aggrade at a nearly constant rate until the overlying flow is entirely consumed, as also inferred from textural studies of pyroclastic flow deposits [*Branney and Kokelaar*, 1992; 2002]. The body of pyroclastic flows is likely to be almost fully fluidized provided pore pressure diffusion is relatively slow and viscous gas-particle interactions caused by differential motion between the solid and fluid phases are strong enough, the latter occurring through mixture contraction and particle settling as well as auto-fluidization as defined above. Internal interparticle contact stresses may then be considerably reduced, thus conferring an inertial fluid-like behavior despite the very high particle concentration [*i.e.*, *Roche et al.*, 2008] and the presence of a sliding head. In this context, the contribution of the head to the whole flow resistance would be negligible, though basal shear might contribute to generate erosion features as described above. At late stages of emplacement, particle interactions are expected to become dominant once pore pressure has decreased sufficiently, thus promoting a transition from a fluid-inertial to a granular-frictional behavior [*Roche et al.*, 2008].

The relative magnitudes of the pore pressure diffusion and advection timescales are important regarding the flow dynamics. Close to the source, the pore pressure can be larger than lithostatic if diffusion is relatively slow and the flow thins rapidly (*i.e.*, Figure 3.12). The issue of the flow run out can be addressed considering the dimensionless pore pressure number defined by *Iverson and Denlinger* [2001]. This number (N_p) represents the ratio of the timescale for flow run out related to pressure advection, $(L/g)^{1/2}$, to the timescale for pressure diffusion, h^2/D, so that

$$N_p = \frac{D(L/g)^{1/2}}{h^2}. \qquad (3.10)$$

In our experiments, with D~0.01 m^2 s^{-1} [*Montserrat et al.*, 2007] and h~0.06 m, then N_p~1. This is larger but close to that for pyroclastic flows as N_p~0.1 if one assumes a same value of D, L~1000 m, and h~1 m. Note, however, that likely smaller hydraulic diffusivity and larger flow thickness values in natural flows would decrease the pore pressure number, thus indicating that high pore fluid pressure would persist relatively longer than in experiments. In consequence, assuming that the mechanisms of pore pressure generation are of comparable relative magnitude at the natural and laboratory scales, the flow run out in nature would be relatively larger than in the experiments. Nevertheless, the structure of the natural flows is expected to be similar to that of their experimental analogs, though more elongated horizontally.

3.5 Conclusion

The emplacement dynamics of dense air-particle gravitational flows were investigated through analogue laboratory experiments. We carried out measurements of the pore fluid pressure in dam break flows generated from the release of fluidized and non fluidized granular columns. The internal structure of the flows was also investigated from analyses of high speed videos. The experimental set up was designed to allow for non invasive measurement of the pore pressure relative to that of the ambient atmosphere, and we studied how it varied both spatially and temporarily during flow emplacement. All types of flows consisted of (1) a sliding head that

caused relative underpressure, followed by (2) a body that generated relative overpressure and at the base of which a deposit aggraded at a nearly constant rate. Both the head and body were sheared pervasively. The measured pressure signal resulted from the combination of several processes (Figure 3.10). The underpressure generated by the sliding head may be explained by two mechanisms, possibly acting together. Dilation of the flow head of the order of 0.1-1 % may generate the amount of the peak of underpressure (P_{min}) observed. Underpressure was also accounted for by the theory developed by *McElwaine* [2005] assuming an inviscid fluid flow, though uncertainties remain on the applicability of the model to our experimental flows. P_{min} was primarily proportional to the basal flow velocity, but depended also on the degree of fluidization of the head as it was relatively smaller in dry flows than in initially fluidized ones whose head was probably at least partially fluidized. We acknowledge, however, that this latter issue deserves further investigation. For initially fluidized mixtures, overpressure in the flow body primarily derived from advection of the pore pressure generated in the initial column, and the flows defluidized by pressure diffusion until they came to halt. The amount of overpressure depended on the relative timescales of pressure advection and diffusion, on auto-fluidization processes, and on variation of the voidage of the air-particle mixture. At early stages, relatively slow pressure diffusion led the pore pressure in the thin flows to be larger than lithostatic. Auto-fluidization was evidenced in initially dry flows, for which at least up to ~16% of the weight of the particles was supported. It arose from shear-induced, relative motion between the particles and the interstitial air. Auto-fluidization occurred probably also in initially fluidized flows and then contributed to generate positive pore pressure along with the other processes. Additionally, slight dilation or contraction of the flow body with air drag and/or pore volume variation led the pore pressure to transiently decrease or increase, respectively. We highlight that, in the case of initially slightly expanded (~3-4 %) fluidized mixtures, high pore fluid pressure persisted for most the flow propagation as (at least) ~70 to 100% of the weight of the particles was supported, thus showing that particle-particle shear interactions were then very much reduced. This provides an explanation for the inertial fluid-like behavior of these flows until the beginning of their stopping phase [*Roche et al.*, 2008].

Our study better applies to pyroclastic flows propagating on subhorizontal slopes, but it may also have interest for other types of dense two-phase gravity currents such as snow avalanches. It shows that accurately modeling gas-particle flows requires taking into account detailed processes of fluid-solid interactions whose degree depend on variation of the voidage of the mixture and on the relative velocity of the two phases [*i.e., Meruane et al.*, 2010]. Pyroclastic flows may consist of two distinct parts, both sheared pervasively: (1) a partially fluidized sliding head that may erode the substrate and where incorporation of accidental lithic clasts can occur; and (2) a fluidized body at the base of which a deposit aggrades [*i.e, Branney and Kokelaar*, 1992; 2002] at a nearly constant rate. Even though these flows are highly concentrated and have a sliding head, they are expected to propagate as inertial fluids for most their emplacement, thus being highly mobile [*i.e., Roche et al.*, 2008]. Particle-particle shear interactions may dominate the flow dynamics only at late stages, when the pore fluid pressure has sufficiently decreased by diffusion and other processes that are likely to increase the pore pressure have become no longer efficient enough.

Acknowledgements. This work would not have been possible without the technical assistance of Delphine Auclair, Eric Brut, Jean-Louis Fruquière, and Jean-Luc Piro at Laboratoire Magmas et

Volcans. Thanks also to Frédéric Chausse (Lasmea, U. Blaise Pascal) for his advice on the experimental set up. This work was supported by Institut de Recherche pour le Développement (IRD, France), and ANR VolBiFlo (France) and ECOS-Conicyt n° C06U01 (France-Chile) projects. An earlier version benefited from stimulating discussions with Tim Druitt, David Jessop, and Jim McElwaine. We thank the anonymous Associate Editor and reviewers for their constructive comments.

Chapter 4

4 Pore fluid pressure diffusion in defluidizing granular columns

This chapter corresponds to the paper authored by Santiago Montserrat, Aldo Tamburrino, Olivier Roche and Yarko Niño, published in *Journal of Geophysical Research*, volume 117 (2012), F02034, 15 pp.

Abstract

Pore-fluid pressure variations play an important role in the motion of natural granular flows like debris and pyroclastic flows. Pore-pressure in a defluidizing air-particle bed was investigated by means of experiments and numerical modeling. Experiments consisted of recording the defluidization process, measured as the decay of the basal pore-fluid pressure in initially aerated granular mixtures. Mixtures were aerated to different degrees of fluidization by introducing a vertical air flux at the base of a granular column. The degree of fluidization was characterized by the parameter βo (pore-fluid pressure / lithostatic pressure). Bed expansion occurred for $\beta o > 0.8 - 0.9$, with maximum expansions near 8 % at $\beta o \sim 1$. Pore-pressure diffusion in our mixtures was modeled by a simple diffusion equation, taking into account a variable diffusion coefficient. When mixtures were expanded ($\beta o > 0.8 - 0.9$), continuous consolidation introduced non-linearities in the diffusion coefficients, which retarded the decay of pore pressure. In contrast, for non-expanded mixtures, the diffusion coefficient remained constant (linear diffusion). Our results highlight that mixture compressibility can effectively reduce the pressure diffusion coefficient in initially expanded granular mixtures, thus increasing the duration of pressure diffusion. In our experiments, as well as for most self-consolidating natural granular mixtures, changes in permeability due to mixture consolidation appear to be negligible for the defluidizing process, as they are counteracted by changes in porosity and because the fluid behaves as incompressible, even when the fluid is air.

4.1 Introduction and objective

Geophysical granular flows consist of solid-fluid mixtures driven by gravity, which propagate over natural terrains. The solid phase typically consists of grains of different sizes, commonly ranging from microns to decimeters and possibly meters, while the fluid phase is

either water or gas. In case of water-solid mixtures, fine sediments and water act as an equivalent fluid phase, with a different effective fluid viscosity, and possibly rheology, with respect to pure water [*Iverson*, 1997; *Major*, 2000]. Examples of geophysical granular flows include debris flows, pyroclastic flows, snow avalanches, and rock avalanches [*Iverson*, 1997*; Iverson and Denlinger*, 2001*; Jain et al.*, 2004*; Freundt et al.*, 2000]. Since *Bagnold* [1954] introduced the concept of dispersive stress, important advances have been made regarding the understanding of fluid-particle flow dynamics. Nevertheless, the formulation of general constitutive laws and their relation with mixture constituents and terrain characteristics remains an active research field.

Geophysical granular flows have been commonly modeled using shallow water equations to solve their bulk behavior [*Savage and Hutter*, 1989; *Denlinger and Iverson*, 2001; *Iverson et al*., 2004; *Vollmöller*, 2004; *Pudasaini et al.*, 2005]. A major issue arises when considering an appropriate flow resistance relationship to adequately describe the flow regime. Such flows have often been modeled as plastic materials, and two plastic theories are commonly used: viscoplasticity and Coulomb plasticity. A viscoplastic model often assumes an equivalent single-phase viscous fluid with a specific rheology, typically of Bingham or Herschel-Bulkley type, as considered in pure fluid mechanics [*Ancey*, 2006; *Naef et al*., 2006]. In contrast, Coulomb plasticity derives from soil-mechanics considerations. Coulomb models are two-phase models that consider both a solid and a fluid phase. The fluid-phase energy dissipation is commonly treated as a viscous term, while inter-particle interactions are assumed to be dominated by friction, which is well described by the Coulomb law [*Savage and Hutter*, 1989; *Iverson*, 1997; *Iverson and Denlinger*, 2001; *Savage and Iverson*, 2003; *Iverson et al*., 2004; *Hutter et al*., 2005; *Pudasaini et al*., 2005; *Ancey*, 2006]. Inter-particle friction is controlled by pore-fluid pressure, which counterbalances the weight of the particles, thus reducing contact shear stresses according to the Terzaghi effective-stress principle [*Iverson*, 1997; *Iverson and Denlinger*, 2001; *Savage and Iverson*, 2003; *Goren et al*., 2010]. Thus, inter-granular pore-fluid pressure appears important for understanding the dynamics and mobility of granular flows. When dilute mixtures are highly agitated, particle collisions dominate energy dissipation within the flow. In these cases, constitutive equations derived from the kinetic theory of gases have provided good flow descriptions [*Campbell*, 1990; *Azanza et al*, 1999; *Goldhirsch*, 2003]. In most natural granular flows, as well as in industrial applications, the two limiting regimes, frictional and collisional, coexist [*Ancey and Evesque*, 2000; *Armanini, et al*., 2005]. Two-dimensional numerical simulations of sheared granular layers have shown the appearance of force chains, formed by long-lasting contact networks (frictional forces), which transmit most of the stress within the flow [*Aharonov and Sparks*, 1999]. Vertical rheological stratification has been experimentally observed by *Armanini et al*., [2005, 2008] in chute flows, where distinct sub-layers are characterized by either frictional or collisional regimes.

Observations made at different scales support the idea that pore-fluid pressure in excess of hydrostatic or atmospheric pressure, respectively, in wet and dry mixtures (hereafter named excess pore-fluid pressure), can be retained for long durations. High pore-fluid pressure has been measured in experimental and natural debris flows [*Iverson*, 1997; *Major and Iverson*, 1999; *McArdell et al*., 2007] and in laboratory experiments on initially fluidized air-particle flows [*Roche et al*., 2010], and explains why the run-out of fluidized flows can be twice that of non-fluidized flows [*Roche et al*., 2004, 2008; *Girolami et al*., 2008]. In spite of the prevailing idea that differential fluid-particle motion generates excess pore-fluid pressure that may diffuse in

ways that depend on the mixtures characteristics [*Iverson and LaHusen*, 1989; *Iverson, 1997*; *Iverson and Denlinger*, 2001; *Goren et al*., 2010, 2011], the details of the associated pore-pressure dynamics (generation, transport and diffusion) are still poorly understood. Based on experimental data, *Iverson and Denlinger* [2001] proposed that basal pore pressure should advect passively with the flow in the horizontal directions (x and y), and simultaneously diffuse in the vertical direction (z) following a simple linear diffusion model [*Iverson and Denlinger*, 2001, their eq. 59]. This approach has been used by different authors to model debris flows and has led to good results, requiring a prescribed model for the pore-pressure diffusion coefficient [*Vollmöller*, 2004; *Denlinger and Iverson*, 2001; *Pudasaini et al*., 2005]. *Savage and Iverson* [2003] explicitly coupled a pore-pressure-diffusion equation to changes in debris flow thickness and showed that pore pressure can be generated due to changes in flow height. Recently, a numerical model coupling the evolution of dilatancy, solid and fluid volume fractions, pore-fluid pressure, and flow depth and velocity has demonstrated the ability to simulate debris flows from initiation to deposition [*George and Iverson*, 2011]. Numerical results compared well with experimental data.

Previous one-dimensional experimental results on a defluidizing static column have shown that above a critical value of about ~80-90 % of full initial fluidization, occurring at the onset of bed expansion, the pore-pressure diffusion coefficient drops abruptly. Linear pore pressure diffusion models [*Major*, 2000; *Iverson and Denlinger*, 2001] fail to represent the pore pressure diffusion in static granular columns for fluidization degrees exceeding those triggering the onset of bed expansion [*Montserrat et al*., 2007]. At the same critical fluidization threshold, an important increase in the run-out distance of initially expanded mixtures occurs [*Montserrat et al*., 2007; *Roche et al*., 2004, 2008, 2010], suggesting that changes in the pore pressure diffusion dynamics may significantly affect flow behavior. This work aims to extend the present understanding of pore pressure diffusion at fluidization degrees exceeding the critical value, for expanded mixtures, towards a better description of the implications and modeling of pore pressure in granular flows. To this purpose, we carried out coupled experimental and numerical studies on the pore-pressure diffusion process in a static granular bed. Experiments focused on the decay of pore pressure at the base of a reservoir filled with an air-particle mixture that can be fluidized at different degrees by introducing a vertical upward air flux through the granular medium [*Montserrat et al*., 2007]. Similar, fluidization techniques have been used since the early 1970s in studies related to industrial applications as well as to pyroclastic flows [e. g. *Davidson and Harrison*, 1971; *Geldart*, 1973; *Wilson*, 1980; *Geldart and Wong*, 1985; *Lorences et al*., 2003; *Roche et al*., 2004, 2008, 2010; *Druitt et al*., 2007]. In our experiments, fluidization was used to generate an initial excess pore-pressure gradient, above atmospheric, within the granular mixture. In nature, excess pore-fluid pressure can be caused by particle settling or by the presence of an upward fluid flux, both configurations being dynamically equivalent [*Richardson and Zaki*, 1954; *Druitt et al*., 2007]. Our results show that pore-pressure diffusion can be well represented, from nil to complete fluidization, by a simple linear diffusion model taking into account a variable diffusion coefficient. The coefficient is a strong function of the mixture compressibility, which in turns depends on the initial degree of fluidization. For low degrees of fluidization, the linear diffusion model (with a constant pore-pressure diffusion coefficient) is recovered.

The experiments presented here are probably the simplest way to study pore-pressure diffusion in granular mixtures, and represent a first step toward the study of pore pressure in

flowing mixtures. We acknowledge that in sheared flows, however, complex processes such as deposition, varying flow height [*Girolami et al*., 2008; *Roche et al*., 2010], continuous grain rearrangement (dilative-compactive grains motion [*Iverson and LaHusen*, 1989; *Goren et al*., 2010]), self-fluidization due to flow instabilities and gas entrainment [*Bareschino et al*., 2008], and other processes can affect pore pressure dynamics

4.2 Experimental device and procedure

The experimental device (Figure 4.1) consisted of a 0.5 m tall rectangular Plexiglas reservoir having a cross-sectional area of 0.1×0.2 m^2, which contained a dry particle mixture. An air flux was introduced through a 10 mm thick porous plate (pore size ~ 20 μm) located at the bottom of the reservoir in order to fluidize the mixture. Air was first introduced in a wind box separated from the tank by the porous plate (Figure 4.1). A pressure transducer, placed perpendicular to the upward air flux, continuously measured the pore pressure at the base of the reservoir. Air flow velocities (with maximum interstitial values ~ 10 mm/s) were low enough to not affect the pressure transducer readings. The air flux could be stopped almost instantaneously (in ~0.01s) by means of a solenoid valve, thus starting the defluidizing process. Pore pressure could not diffuse back towards the porous plate because pressure was maximum in the wind box. Measurements taken inside the wind box showed that pressure diffused almost instantaneously (<0.01s) when no particles were placed above the porous plate. Thus, the wind box could be neglected in the analysis, and the porous plate could be assumed as an impermeable wall above the granular column after the solenoid valve was closed. Therefore, pore pressure diffusion only occurred in the upward direction. Special care was taken to control the mixture humidity in order to avoid excessive cohesion and electrostatic effects and to ensure reproducibility of the experiments. Air was dried before entering the reservoir. A humidity transducer placed at the top of the reservoir controlled the air flux relative humidity (RH), which had a mean value of 35 % ± 5 %. Before each experiment, the particles were aerated for about one hour.

When a vertical air flow is supplied at the bottom of a granular column, an upward drag force is exerted on the particles. When the drag force is less than the weight of the particles, the granular column is commonly termed aerated [*Gibilaro*, 2001]. If the weight of the particles is fully counterbalanced by the drag force, the column is termed fluidized. In fluidized granular columns, intergranular frictional stress is negligible and the fluid-particle mixture acquires fluid-like properties, with the internal pore fluid pressure equaling that generated by the particle network. A linear pressure gradient is established during the aeration procedure, with maximum pore pressure at the base of the mixture and atmospheric pressure at the top of the granular column. The degree of fluidization is defined by comparing the pore pressure at the base of the granular column (p_{bed}) with the lithostatic pressure, P_L, (defined as the particles weight divided by the cross sectional area of the container). Thus, when $p_{bed}/P_L = \beta_0 < 1$, the bed is aerated, and when $p_{bed}/P_L = \beta_0 = 1$, the bed is fully fluidized.

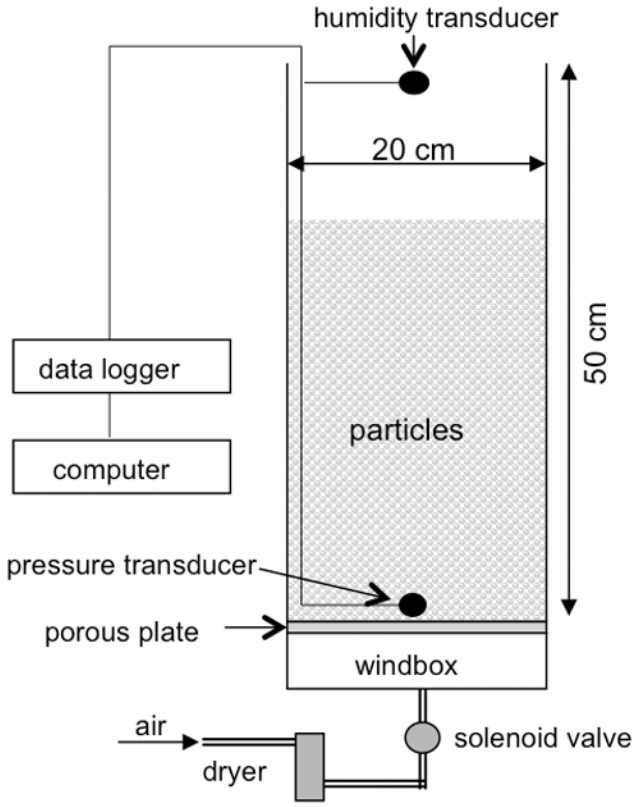

Figure 4.1. Sketch of the experimental device.

We used nearly spherical glass beads, with a density of 2500 kg/m³ (Ballotini, Potters Industries), which had almost the same characteristics as those used by *Roche et al*. [2004, 2008, 2010] in their dam break studies on air-particle flows. Particle diameter ranged from 45 to 90 μm, with a mean diameter of about 60 μm (measured by a Mastersizer 2000 particle analyzer, Malvern Instruments Ltd.). The bulk density of the granular bed was 1400±40 kg/m³, which indicated a porosity of 0.44 ± 0.02. In terms of their gas fluidization properties, the particles belonged to the *Geldart* [1973] group A. This means that once particles are fully fluidized at a critical air flow velocity, *Umf* (minimum fluidization velocity), gas bubbles form at a second critical velocity, *Umb* > *Umf*. Note that air flow velocity is defined as the volumetric air flow rate (introduced at the bottom of the reservoir) divided by the reservoir cross-sectional area. Between *Umf* and *Umb*, the homogeneously fluidized bed expands linearly as the flow rate is increased [*Gibilaro*, 2001; *Roche et al*., 2004]. In practice, fluidization may not be fully homogeneous throughout the granular column, as air flow channeling tends to occur. Thus, bed expansion may occur before complete fluidization is achieved [*Gilbertson et al*., 2008]. For this reason, *Umf* is defined in practice as the air velocity at the onset of bed expansion, which commonly occurs at velocity slightly smaller than that for which full bed support is achieved. This definition is used here [cf. *Roche et al*., 2004; *Druit et al*., 2007].

At the laboratory scale, the use of group A particles of small grain size (and hence small permeability) is required for allowing pore pressure measurements, as mixtures of coarser particles diffuse pore pressure too fast and are almost immediately defluidized [*Iverson*, 1997;

Major, 2000; *Iverson and Denlinger*, 2001, *Druitt et al*., 2007, *Roche et al*., 2004]. It is important to note that our experiments best apply to natural gas-particle mixtures, such as pyroclastic flows, because fluidized beds of pyroclastic debris that consist of a matrix of fine ash have a typical group-A behavior, including homogenous expansion [*Druitt et al*., 2007]. In addition, the defluidization process characteristics of our beds of group-A particles share similarities with pore pressure diffusion in consolidating debris flow deposits [Iverson, 1997; *Major*, 2000]. In particular, *Major* [2000] showed experimentally that pore-fluid pressure in debris flow deposits can diffuse in a few seconds to several hours depending on the amount of fine sediment in the debris.

4.3 Pore pressure modeling

The complete equation describing the dynamics of pore pressure in porous media is well known and can be easily derived by coupling the fluid-phase continuity equation (equation 4.1) with the Darcy equation (equation 4.2), which is a reduced form of the fluid-momentum equation assuming negligible inertia [*Goren et al*., 2010]:

$$\frac{\partial}{\partial t}(\rho_a \phi)+\frac{\partial}{\partial x}(\rho_a \phi\ u)=0 \tag{4.1}$$

$$\phi\ u=-\frac{k}{\mu}\frac{\partial p}{\partial x} \tag{4.2}$$

where p is the pore pressure, t is time, k is the mixture permeability, μ is the fluid dynamic viscosity ϕ is the bed porosity, x is the length coordinate, u is the interstitial air flow velocity, and ρ_a is the fluid density. Inertia can be neglected because of low Reynolds numbers, $Re = \rho_a\ u\ l\ /\ \mu$, where l is a characteristic length scale of the flow. In our experiments, u has maximum values of ~ 10 mm/s, ρ_a = 1.2 kg/m³ and $\mu = 1.8 \times 10^{-5}$ Pa s (typical values of ρ_a and μ for air at ambient temperature). The characteristic length, l, scales with pore sizes that are about equal to the particle diameter. Thus, l ~ 60 μm. With these considerations, Reynolds numbers Re < 0.1, justifying the assumption of negligible inertia. Coupling equations 4.1 and 4.2, the 1-D pore pressure equation can be expressed as [*Yilmaz et al*., 1994; *Liang et al*., 2001]:

$$\frac{\partial p}{\partial t}=D\frac{\partial^2 p}{\partial x^2}+D(\gamma+c_f)\left(\frac{\partial p}{\partial x}\right)^2 \tag{4.3}$$

where

$$D=\frac{k}{\mu\phi(c_\phi+c_f)} \tag{4.4}$$

$$c_\phi=\frac{1}{\phi}\frac{\partial \phi}{\partial p};\qquad c_f=\frac{1}{\rho_a}\frac{\partial \rho_a}{\partial p};\qquad \gamma=\frac{1}{k}\frac{\partial k}{\partial p} \tag{4.5}$$

D corresponds to the pore-pressure diffusion coefficient. The term c_ϕ is the so called porosity compressibility, c_f is the fluid compressibility, and γ is known as the permeability compliance since it describes the variation of permeability with pore pressure [*Yilmaz et al*., 1994]. The Darcy equation used for the derivation of equations 4.1 to 4.5 neglect particles velocity, and can be used for the analysis of quasi-static consolidation [*Major*, 2000]. Although this assumption appears reasonable for cases such as that investigated in the present study on the consolidation of moderately expanded mixtures, the above equations fail to predict pore pressure variations when significant grain rearrangement occurs [cf. *Iverson and LaHusen*, 1989; *Goren et al*., 2010; 2011]. Compared with other proposed formulations [see *Goren et al*., 2010], our model (equations4. 3 to 4.5) appears to be adequate for studying pore-pressure dynamics for a prescribed initial pore pressure (generated by means of fluidization or rapid initial particle settling) when relative particle motion is negligible (quasi-static consolidation).

If volume changes of the mixture are negligible, ϕ remain constant so that c_ϕ ~0. With this assumption, a characteristic pore-pressure diffusion coefficient can be defined as $Do = k_o / (\mu\, \phi_o\, c_{fR})$, where the subscript o indicates reference values of the mixture in the non-expanded and non-aerated (i.e., no air flux) state, and c_{fR} denotes a reference value for the fluid (air or water) compressibility.

In the following analysis, dimensionless variables are introduced,

$$p^* = p / P_L \;,\quad x^* = x / H \;,\quad t^* = t^* / \tau \;,\quad k^* = k / k_o \;,\quad \phi^* = \phi / \phi_o$$
$$c_f{}^* = c_f / c_{fR} \;,\quad c_\phi{}^* = c_\phi / c_{fR} \;,\quad \gamma^* = \gamma / c_{fR} \qquad (4.6)$$

where the superscript * denotes dimensionless variables. P_L is the lithostatic pressure at the bottom of the mixture given by $P_L = \rho\, g\, H$, ρ and H are the mixture density and height respectively, and g is gravitational acceleration. The time scale for pore pressure diffusion is given by $\tau = L^2 / Do$, where L is a characteristic length scale along which pressure is diffused. As in our experiments the base of the tank can be considered impermeable, the characteristic length scale $L \sim H$ [*Iverson*, 1997; *Major*, 2000; *Iverson and Denlinger*, 2001]. Substituting the dimensionless variables of Equation 4.6 into the pore pressure diffusion equations (equations 4.3 to 4.5), a dimensionless form of the system of equations describing pore pressure evolution is then obtained:

$$\frac{\partial p^*}{\partial t^*} = D^* \frac{\partial^2 p^*}{\partial x^{*2}} + D^* \left(\gamma^* + c_f{}^*\right) c_{fR} P_L \left(\frac{\partial p^*}{\partial x^*}\right)^2 \qquad (4.7)$$

$$D^* = \frac{D}{Do} = \frac{k^*}{\phi^* \left(c_\phi{}^* + c_f{}^*\right)} \qquad (4.8)$$

where D^* represents a dimensionless diffusion coefficient. As stated by *Yilmaz et al*. [1994], it is known that the (dimensional) coefficients c_ϕ and γ are functions of p. To assess the relative impact of these parameters in highly confined porous media, they assumed c_ϕ and γ to be

pressure invariant. Here we relax such a hypothesis by assuming that the dimensionless quantities c_ϕ* and γ* are proportional to p*:

$$c_\phi^* = \alpha \; p^* \tag{4.9}$$

and

$$\gamma^* = \delta \; p^* \tag{4.10}$$

where α and δ are unknown constants. As it will be shown hereafter, this assumption is validated by agreement between the model and the experimental data. Substituting these relationships in the definitions of c_ϕ and γ in equation 4.5 (using the dimensionless parameters defined in equation 4.6), and integrating between the limits [0 , p*], [*1* , ϕ*] and [*1* , k*], the dimensionless porosity and permeability can be expressed as

$$\phi^* = \exp\left(\frac{\alpha \; c_{fR} \; P_L}{2} \, p^{*2} \right) \tag{4.11}$$

$$k^* = \exp\left(\frac{\delta \; c_{fR} \; P_L}{2} \, p^{*2} \right) \tag{4.12}$$

Replacing equations 4.11 and 4.12 in equations 4.7 and 4.8 leads to

$$\frac{\partial p^*}{\partial t^*} = D^* \frac{\partial^2 p^*}{\partial x^{*2}} + D^* \left(\delta \; p^* + c_f^* \right) \; c_{fR} \; P_L \left(\frac{\partial p^*}{\partial x^*} \right)^2 \tag{4.13}$$

$$D^* = \frac{1}{\left(\alpha \; p^* + c_f^* \right)} \exp\left(\left(\delta - \alpha \right) \frac{c_{fR} \; P_L}{2} \, p^{*2} \right) \tag{4.14}$$

Solutions of pore-pressure evolution from equations 4.13 and 4.14 depend on the value of $c_{fR} P_L$, which is a dimensionless parameter that compares the reference fluid compressibility with the lithostatic pore pressure. Thus, highly compressible fluids as well as thick mixtures are characterized by high values of $c_{fR} P_L$. In contrast, for low fluid compressibility and/or shallow mixtures, it is obvious from equation 4.13 that if $c_{fR} P_L << 1$ the quadratic term on the right hand side becomes negligible, and in equation 4.14 the exponential tends toward 1, thus rendering the pore pressure time variation independent of δ. Hence, equations 4.13 and 4.14 can be reduced to a non-linear diffusion equation independent of both δ and $c_{fR} P_L$,

$$\frac{\partial p^*}{\partial t^*} = D^* \frac{\partial^2 p^*}{\partial x^{*2}} \tag{4.15}$$

$$D^* = \frac{1}{\left(\alpha \; p^* + c_f^* \right)} \tag{4.16}$$

Low values of $c_{fR}\,P_L$ can be found in many granular mixtures, making the above simplifications relevant for the analysis. Water and air have a compressibility of ~5×10^{-10} Pa^{-1} and ~10^{-5} Pa^{-1}, respectively. Heights of ~0.1 to ~20 m are representative of many experimental and geophysical flows, for both wet and dry mixtures [*Iverson*, 1997; *Iverson and Denlinger*, 2001; *Freundt et al*., 2000]. Considering mixture densities in the range 500 - 2500 kg/m^3 for both air- and water-solid mixtures, P_L ranges from ~10^2 to ~10^6 Pa. With these limits, $c_{fR}\,P_L$ takes values of ~10^{-8} to ~10^{-4} for water-solid mixtures and of 10^{-3} to 10 for air-solid mixtures. Thus, equations 4.15 and 4.16 might be applicable for most cases of debris flows (water-solid mixtures) as well as very thin air-solid mixtures. For the experiments reported here, the mixture density is ~1400 kg/m^3 and height is always lower than 0.5 m, so that $c_{fR}\,P_L < 0.07$. Hence, the assumption $c_{fR}\,P_L << 1$ may be suitable for our experiments. As it will be shown hereafter, the non-linear pore pressure diffusion model described by equations 4.15 and 4.16 approximates well our experimental data, and so $c_{fR}\,P_L << 1$ will be considered in the following analysis.

If pore volume changes are negligible (i.e. $c_\phi^* \sim 0$) and the fluid can be considered incompressible (i.e. $c_f^* \sim 1$), as expected for water-solid mixtures, the dimensionless pore pressure diffusion coefficient, D^*, is approximately 1. Under these conditions, equation 4.5 reduces to a linear diffusion equation (equation 4.17), as proposed for pore-pressure diffusion in debris-flows modeling [*Iverson and Denlinger* 2001] and for consolidating debris-flow deposits [*Major*, 2000]:

$$\frac{\partial p^*}{\partial t^*} = \frac{\partial^2 p^*}{\partial x^{*2}} \tag{4.17}$$

An initial condition (IC) and two boundary conditions (BC) are required to solve equation 4.15. The initial condition corresponds to a linear pore-pressure profile, ranging from the initial dimensionless pore-pressure value $\beta_o = p_{bed} / P_L$ at the base of the tank (where p_{bed} is the initial pore-pressure at the base of the tank), to 0 at the free surface of the mixture. Boundary conditions are given for zero pore pressure at the top and zero pore pressure flux at the base. Because a pore pressure flux in the experiments persists for a short time while the valve is turned off, an exponential decay is used to model the valve closing. Initial and boundary conditions are thus expressed as:

$$IC: \quad p^*(x^*,0) = \beta_o(1 - x^*) \tag{4.18}$$

$$BC; \quad p^*(1,t^*) = 0 \qquad \frac{\partial p^*(0,t^*)}{dx} = -\beta_o \exp(-\lambda\, t^*) \tag{4.19}$$

where $\lambda = \tau / tc$, $\tau = H^2 / Do$ is the vertical pore-pressure diffusion time scale, and *tc* corresponds to the characteristic closing time of the solenoid valve, ~0.01 s.

The dimensionless pore pressure equations 4.15 and 4.16, satisfying the specified initial and boundary conditions, were solved numerically using a finite-volume scheme with 101 nodes and a dimensionless time spacing $\Delta t^* = 0.01$ [*Patankar*, 1980; *Versteg and Malalasekera*, 1995]. The analytical solution of *Carslaw and Jaeger* [1959, pp. 97, equations 14-15] was used as a

benchmark to validate our numerical model for the case of linear diffusion (i. e. $c_f^* = 1$ and $c_\phi^* = 0$).

4.4 Experimental and numerical studies

4.4.1 Pore pressure diffusion coefficient

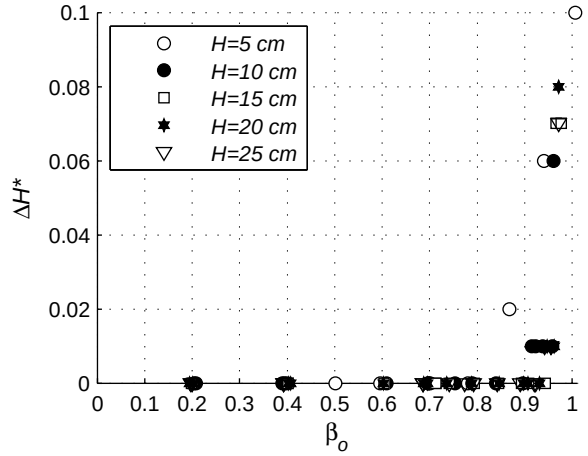

Figure 4.2. Bed expansion as a function of the initial fluidization rate, βo, for different initial bed heights (H). $\Delta H^* = (He - H) / H$, where H is the initial (non-expanded) height and He is the expanded bed height. Bed expansion occurs when $\beta o > \beta o_c$, (with $\beta o_c \sim 0.8$ for $H = 5$ cm and $\beta o_c \sim 0.9$ for $H \geq 10$ cm).

The vertical air flux at the bottom of the tank imposed a pore-fluid pressure, which determined the degree of fluidization, βo. Onset of bed expansion was observed over a narrow range of critical fluidization values ranging from $\beta o_c \sim 0.8$ for a column height of $H = 5$ cm to $\beta o_c \sim 0.9$ for column heights in the range 10 - 25 cm (Figure 4.2). Channeling and heterogeneities were observed in beds at $H = 5$ cm, which caused early onset of bed expansion [*Gilbertson et al*., 2008]. The values of 80 - 90% of complete fluidization corresponding to onset of expansion agree with the findings of *Gilbertson et al*. [2008] for bed depths of 5 - 30 cm. Once the value of βo surpassed βo_c, expansion of the bed increased and reached a maximum value of ~ 8 - 10% at $\beta o \sim 1$ (Figure 4.2). The maximum degree of fluidization was obtained in the bubbling state, whereas complete fluidization ($\beta o = 1$) was difficult to achieve.

In our experiments, $c_{fR} P_L$ could be neglected. Furthermore, the air compressibility may be estimated as $c_f = 1 / P_{abs}$, where P_{abs} is the absolute pressure. The absolute pressure corresponds to $P_{abs} = P_{atm} + p$, where P_{atm} is the atmospheric pressure ($P_{atm} \sim 10^5$ Pa) and p is the pore fluid pressure in excess to P_{atm}. As p scales with P_L, the reference pore fluid compressibility may be estimated as $c_{fR} = 1 / (P_{atm} + P_L)$. If $P_L << P_{atm}$, $c_{fR} \sim 1 / P_{atm}$. On the contrary, if $P_L >> P_{atm}$, $c_{fR} \sim 1 / P_L$. In our experiments, P_L had maximum values of ~5000 Pa, that is to say, p and P_L are at least two orders of magnitude smaller than P_{atm}, and thus $c_{fR} \sim 1 / P_{atm}$. Similarly, $P_{abs} \sim P_{atm}$ whence $c_f \sim 1 / P_{atm} \sim 10^{-5}$ Pa^{-1}, which means that the dimensionless pore fluid compressibility $c_f^* = c_f \, c_{fR}^{-1} \sim 1$. Therefore, in our experiments, the pore fluid could be considered incompressible. In

addition, for $\beta o < \beta o_c$ pore volume changes were negligible, making $c_\phi^* = 0$. Thus, in the non-expanded state, ($\beta o < \beta o_c$) the simple linear diffusion equation (equation 4.17) could be used to describe pore pressure diffusion. Although equation 4.17 seems not to be adequate for solving the pore pressure diffusion in initially expanded mixtures ($\beta o > \beta o_c$) as $c_\phi^* > 0$, and as we do not know how much our experiments deviate from the linear case, we assumed as a first approximation that the linear diffusion equation also applied for this narrow range of βo values. Note that *Major* [2000] found experimentally that the simple linear diffusion model satisfactorily described pore-pressure diffusion in consolidating (with small initial expansion < ~10 %) non-cohesive debris-flows deposits. Our estimates of *Do* were obtained by fitting the linear numerical solution of the pore-fluid pressure to the experimental measurements at the base of the tank, following the procedure used by *Major* [2000]. The chosen *Do* value was the one that minimized the root mean square (rms) differences between the experimental data and the numerical results. Examples of this procedure for different βo values are shown in Figure 4.3. Results show that the proposed linear model fits well the experimental data when $\beta o < \beta o_c$. For higher values of βo, the model deviates from the experimental results. In fact, Figure 4.3c shows that the theoretical time for the basal pore-pressure diffusion is about twice that observed experimentally. This suggests that non-linearities in the pore-pressure diffusion coefficient, due to the initial expansion and continuous mixture consolidation, cannot be neglected in the analysis. In other words, D^* should not be considered equal to 1 when $\beta o > \beta o_c$.

The variation of *Do* as a function of βo is presented in Figure 4.4. The data show that for a given height of material, *Do* slightly decreases with βo and tends toward a nearly constant value, *Dm*, in the range $\beta o \approx 0.7$ to βo_c. For $\beta o > \beta o_c$, when the bed is expanded, fitted values of *Do* drop abruptly, suggesting that initially fluidized expanded beds retain pore pressure for longer durations, behavior that is shown in Figure 4.4A for a single bed height. However, this result is not conclusive, as the linear model overestimates the time of pore-pressure diffusion. Figure 4.4B compiles the data for different bed heights, showing that for a given βo value, *Do* increases with bed height, which is probably related to different degrees of initial bed compaction.

The value of *Dm*, the mean *Do* value obtained in the range $\beta o \approx 0.7$ to βo_c, shows a linear dependence with the bed height, having a constant slope $Uc = 0.29$ m/s (Figure 4.5). Thus, *Uc* appears to be a characteristic velocity for pore-pressure diffusion in our experiments. In the following analysis, experiments at $H = 5$ cm are not considered because strong heterogeneities and channeling in the fluidized beds did not allow for a detailed analysis.

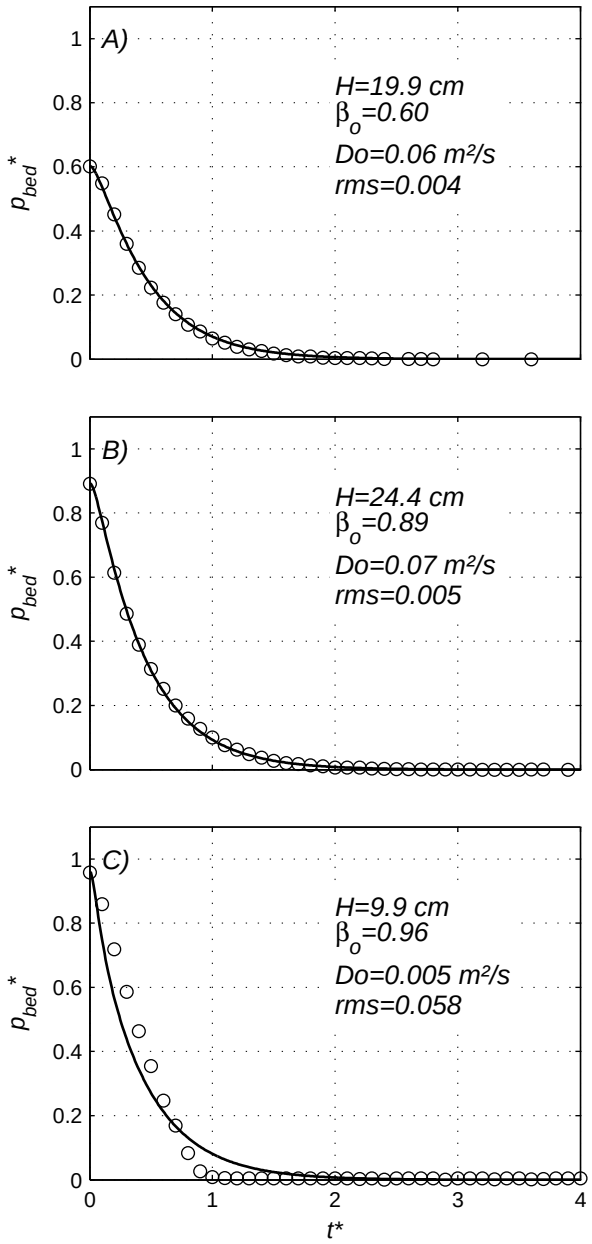

Figure 4.3. Experimental data (○) and theoretical model (—) for the time variation of pore pressure at the base of the granular column for: A) $\beta o < \beta o_c$ B) βo values lower but close to βo_c and C) $\beta o > \beta o_c$. For column height of the order of or greater than ~10 cm, βo_c ~0.9. The solid line corresponds to the best-fit curve with experimental data, adjusting the pore-pressure diffusion coefficient, *Do*. In the figures, *rms* stands for root mean square error of the fitted curve respect to the experimental data.

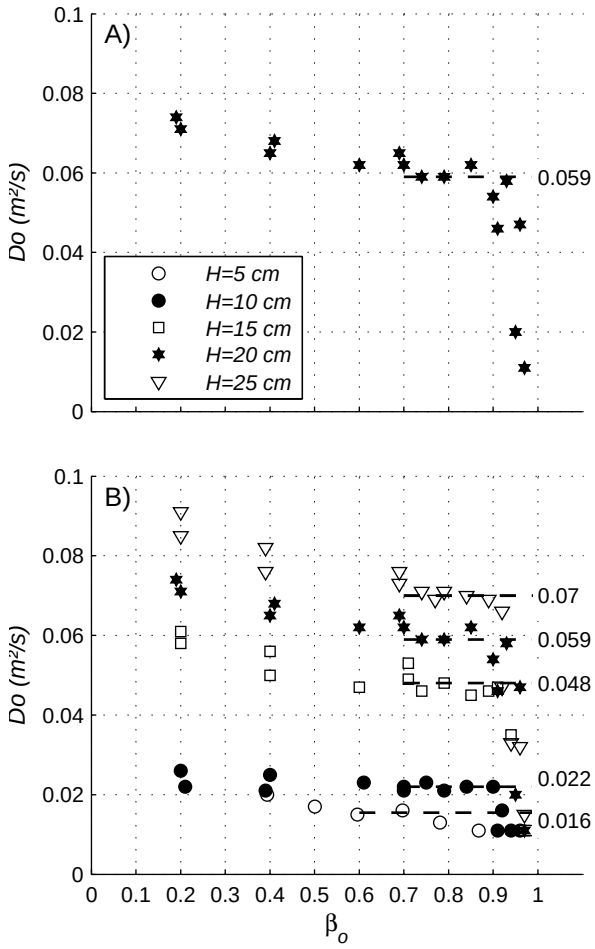

Figure 4.4. Variation of the pore-pressure diffusion coefficient, *Do*, as a function of the initial degree of fluidization, βo, obtained by fitting the experimental measurements at the base of the tank with the linear diffusion model ($D^* = 1$). Figure 4.4A) shows a decrease of *Do* with βo, tending to an almost constant value of *Do* in the range $0.7 < \beta o < \beta o_c$ ($\beta o_c \sim 0.9$). When $\beta o > 0.9$, an abrupt drop in *Do* is observed. Figure 4.4B) summarizes the same results but for different column heights ($\beta o_c \sim 0.8$ for $H = 5$ cm and $\beta o_c \sim 0.9$ for $H > 5$ cm). Numbers on the right indicate values of *Dm*.

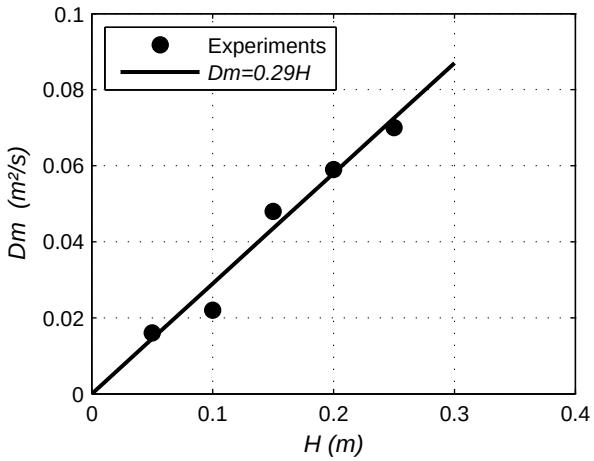

Figure 4.5. Linear dependence of, *Dm*, the mean linear diffusion coefficient in the range $0.7 < \beta o < \beta o_c$ ($\beta o_c \sim 0.8$ for $H = 5$ cm and $\beta o_c \sim 0.9$ for $H > 5$ cm) in terms of the initial column height, *H*.

4.4.2 Pore-pressure-diffusion time scales

For high degrees of fluidization before bed expansion (i.e., $0.7 < \beta o < \beta o_c$, $\beta o_c \sim 0.9$), *Do* tends to an almost constant value, *Dm*. The latter coefficient results to be a characteristic value for pore-pressure diffusion in the expanded state. Thus, in the narrow range of fluidization degrees between $\beta o_c < \beta o < 1$, the pore pressure diffusion coefficient could be estimated as $D = Dm\ D^*$, where *Dm* accounts for linear diffusion while D^* accounts for non-linearities due to mixture compaction during the defluidization process. In other words, the pore pressure diffusion coefficient at high degrees of fluidization in expanded beds scales with *Dm*. To account for the importance of non-linear effects due to the pressure diffusion process in expanded beds, the time for pore pressure diffusion obtained from the experiments is compared to that obtained by assuming a linear diffusion model, using *Dm* as a characteristic value when $\beta o_c < \beta o < 1$.

For a given initial fluidization degree, βo, a theoretical characteristic dimensionless diffusion time scale is defined as:

$$T_{char} = \frac{1}{\beta_0} \int p^*_{lin}\, dt^* \tag{4.20}$$

where p^*_{lin} is the dimensionless pore pressure at the base of the tank obtained from the linear pore pressure equation (equation 4.17). Similarly, an experimental dimensionless diffusion time scale, T_{exp}, based on the measured dimensionless pressure at the base of the tank ($p^*_{measured}$) is defined as:

$$T_{\exp} = \frac{1}{\beta_0} \int p^*_{measured}\, dt^* \tag{4.21}$$

For the purposes of estimating T_{exp}, $p^*_{measured}$ was made dimensionless using the corresponding value of P_L, and the dimensionless time, t^*, was obtained with the time scale $\tau = H^2 / D_i$, where $D_i = Do$ for $\beta o < \beta o_c$ ($\beta o_c \sim 0.9$), and $D_i = Dm$ for $\beta o > \beta o_c$.

Figure 4.6 shows the dependence of T_{exp} / T_{char} on βo. T_{exp} / T_{char} ~1 for $\beta o < \beta o_c$, as expected because $D^* = 1$. In contrast, the time ratio increases substantially as $\beta o \sim 1$, demonstrating that bed expansion retards pore-pressure diffusion by a factor of about 4 compared to the linear diffusion case. This result may seem contradictorily as the pore-pressure diffusion timescale would be expected to decrease in the case of an initial bed expansion due to the increase in permeability. However, as shown by equations 4.4 and 4.8, although the pore-pressure diffusion coefficient is proportional to the mixture permeability, it is inversely proportional to the mixture porosity that increases when the bed expands [*Iverson* 1997; *Major*, 2000]. Therefore, if changes in porosity outweigh changes in permeability, as porosity increases, the pore-pressure diffusion should decrease, and the diffusion time scale should increase.

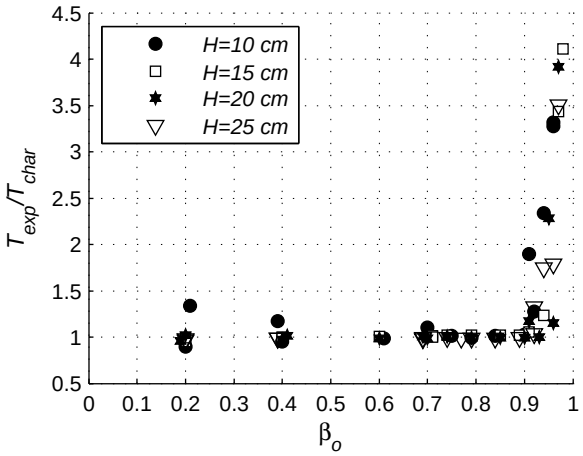

Figure 4.6. Ratio of characteristic diffusion time scales, T_{exp} / T_{char}, where T_{exp} represents a characteristic dimensionless diffusion time scale estimated by means of the measured basal pore fluid pressure evolution and T_{char} corresponds to a characteristic dimensionless diffusion time scale based in the linear solution for the pore fluid pressure equation. The experimental pore-pressure diffusion time scale becomes larger than the theoretical linear diffusion time scale at $\beta o > \sim \beta o_c$. Values greater than 1 for $\beta o \sim 0.2$ and $\beta o \sim 0.4$ and $H = 10$ cm are attributed to errors in the experimental procedure.

4.4.3 Pore-pressure modeling of initially expanded columns

Porosity changes appear to be a key factor influencing pore-pressure diffusion when mixtures are initially expanded. Thus, equations 4.15 and 4.16 appear more suitable for computing pore-pressure diffusion in our experiments, assuming that $c_{fR} P_L << 1$. Equations 4.15 and 4.16 can be solved numerically for given values of α and c_f^*. In our experiments $c_f^* \sim 1$. The values of α in equation 4.16 were obtained by fitting numerical solutions of equations 4.15 and

4.16 to the experimental pressure data at the base of the tank, with α as a fitting parameter. For the fitting procedure, it was assumed that $D = Do\ D^*$ in non-expanded mixtures, and $D = Dm\ D^*$ in the case of expanded mixtures. Differences between the experimental data and numerical results were quantified using their root mean squares (rms), and minimized by choosing α as the value that minimizes the rms.

Our results show that values of α are near zero for $\beta o < \beta o_c$, as linear diffusion applies for fluidization degrees below those causing bed expansion (Figure 4.7). In contrast, for $\beta o > \beta o_c$, α values increase up to ~10 for near complete fluidization, showing that the linear pore-pressure diffusion coefficient (Dm) could be reduced by about one order of magnitude in expanded beds at maximum fluidization ($p^* = 1$). This corresponds to maximum values of $c_\phi = c_\phi^*\, c_{fR} \sim 10^{-4}$ Pa^{-1}, which are several orders of magnitude larger than values commonly reported for pressure diffusion in confined porous media (e.g., $c_\phi \sim 0.15 \times 10^{-9}$ - 15×10^{-9} Pa^{-1} [*Yilmaz et al*., 1994; *Hummel*, 2008]) and about 10 times greater than values reported for self consolidating debris-flows mixture [*Major*, 2000].

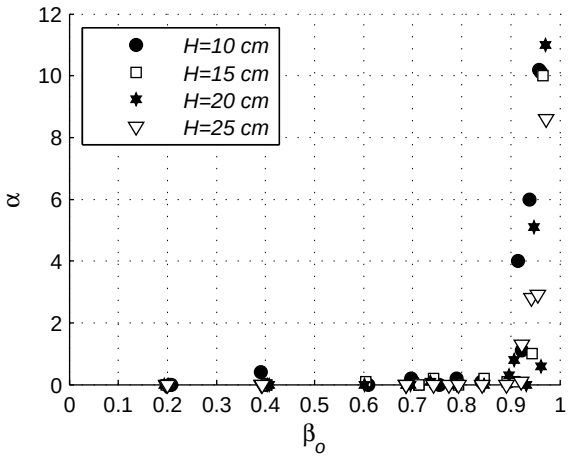

Figure 4.7. Fitted values of α as a function of βo for different initial heights. For $\beta o < \beta o_c$, when the bed is not expanded and the linear diffusion model is applicable, values of α are equal to zero.

Taking into account the fitted values of α, excellent agreement is achieved between the experimental and numerical results for the time needed to diffuse pore fluid pressure (Figure 4.8). This agreement shows that the proposed model adequately describes pore-pressure evolution of initially expanded mixtures. Note that if $\alpha = 0$ in equation 4.15 (and because $c_f^* \sim 1$), the linear diffusion equation is recovered as $D^* = 1$. Thus, the proposed model adequately predicts pore-pressure evolution in non-expanded mixtures. Our results show that when the interstitial fluid is air, assumptions that simplify the pore-pressure equations, specifically $c_{fR} P_L << 1$ and $c_f^* = 1$, are adequate for modeling the pore-fluid pressure time evolution. Such assumptions neglect pore-fluid compressibility effects.

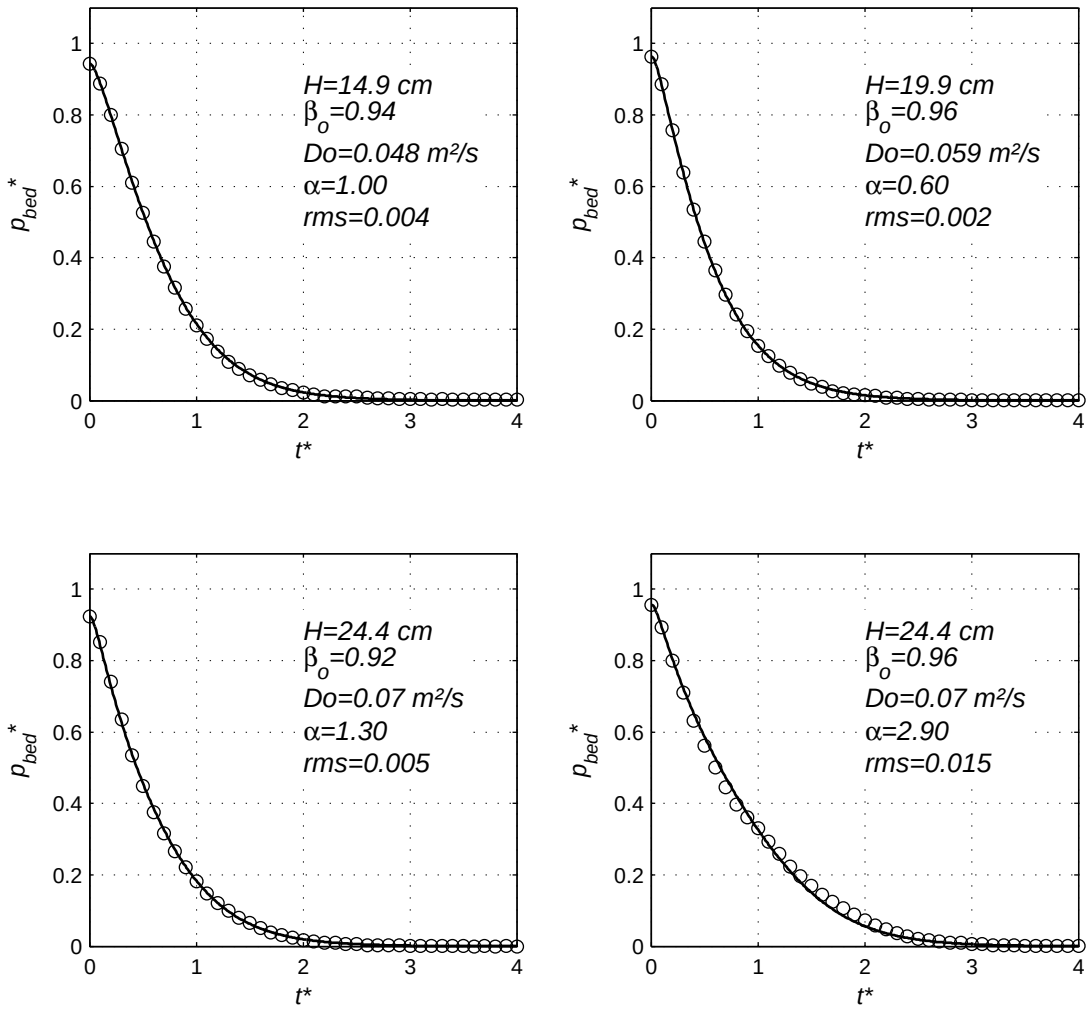

Figure 4.8. Experimental data (○) and numerical fit (—) at the base of the tank for initially expanded mixtures ($\beta o > \beta o_c$) using equations 4.15 and 4.16. In the figures, *rms* stands for root mean square error of the fitted curve respect to the experimental data.

An important increase in the time scale of pore-pressure diffusion is observed as α increases. Numerical results obtained for the case of a fully fluidized mixture (βo = 1) show that for the linear diffusion case (α = 0) pore pressure diffuses almost entirely at t^* ~2 (Figure 4.9). However, excess pore-pressure persists until t^* ~3 when α = 5, and until t^* ~5 when α = 10. Therefore, changes in the porosity compressibility (c_ϕ), resulting from column consolidation, control the diffusion of excess pore pressure in expanded granular material. Additionally, the proposed numerical model provides the time pore pressure evolution at any height within the mixture for a given value of α.

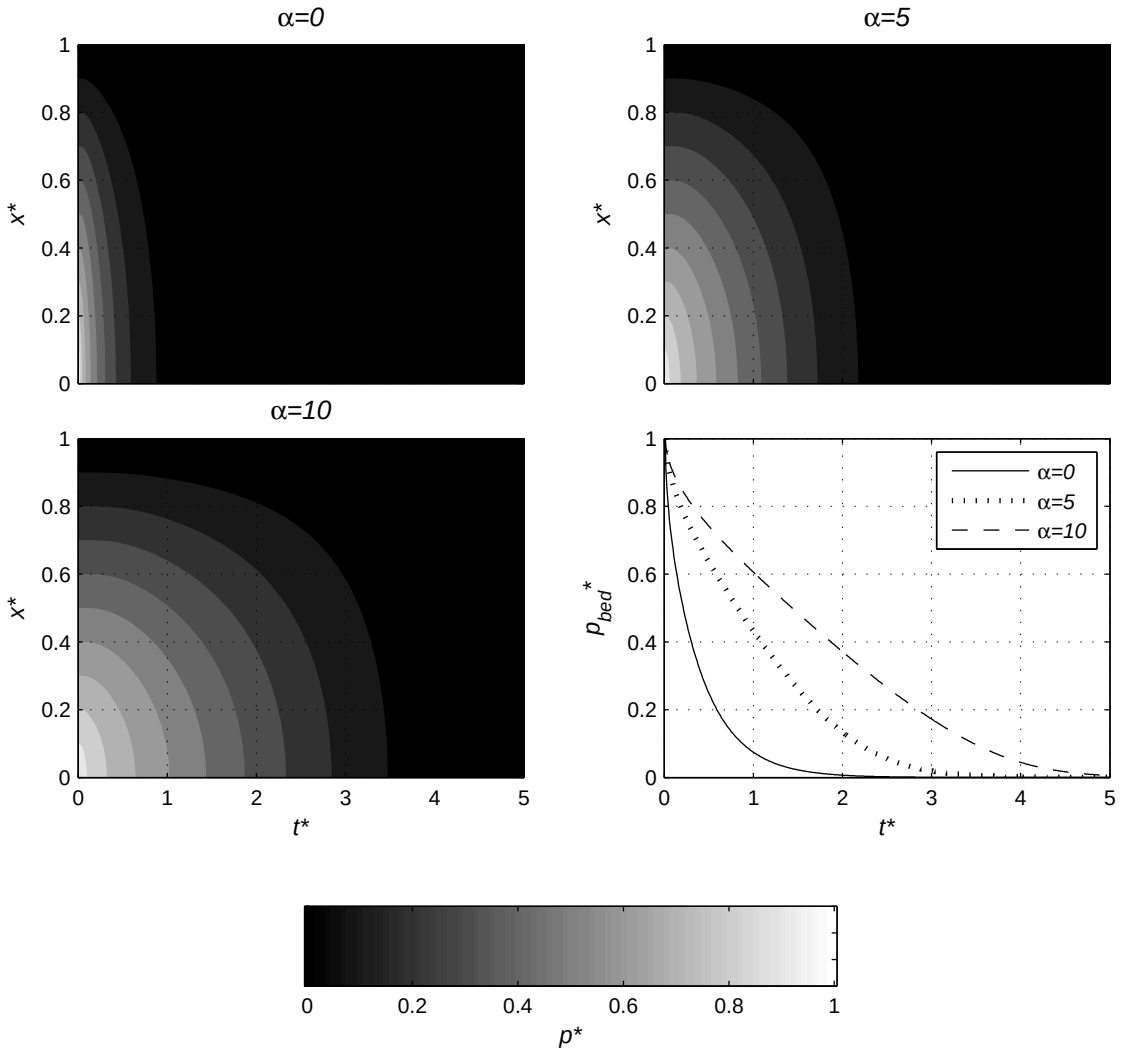

Figure 4.9. Vertical profile of the dimensionless pore pressure time evolution (*p*)* for an initially fully fluidized granular bed and different α values using equation 4.19. Values of α vary in the range of 0 to 10 (Figure 4.7). The solutions shown for $\alpha = 0$ correspond to those of linear diffusion. p_{bed}* at the right bottom corner represents the dimensionless pore fluid pressure at the base of the granular column. The color bar represents values of *p**.

In initially expanded beds, the local pore-pressure diffusion coefficient at a given time is a function of the local pore-pressure, thus the pore pressure diffusion coefficient varies with both time and height (Figure 4.10). For given values of $\alpha > 0$, the diffusion coefficient is maximum at the top of the granular column, as $D^* = 1$, and progressively reduces toward the bottom of the column. The dimensionless diffusion coefficient D^*, decreases as α increases, reaching minimum values of the order of 0.1 at the bottom of the granular column for the maximum values of $\alpha \sim 10$. For linear diffusion ($\alpha = 1$), D^* is constant and equal to 1, independently of time and height. In expanded beds, the return to a linear diffusion behavior ($D^* = 1$) is slowly and asymptotically achieved. Figure 4.9 shows that the time taken for D^* at the bottom of the granular column to reach values of $D^* \sim 1$ is longer that that of pore pressure diffusion. For example, it takes about $t^* = 4$ and more than $t^* = 5$ to reach $D^* \sim 1$ for cases at $\alpha = 5$ and $\alpha = 10$,

respectively, while pore pressure is almost entirely diffused at $t^* = 3$ and $t^* = 4$ for the same conditions (Figures 4.9 and 4.10).

4.5 Discussion

4.5.1 Pore-pressure diffusion in initially aerated granular columns

Pore-pressure diffusion in aerated granular mixtures shows remarkably variable behavior that depends on the degree of initial bulk expansion. For non-expanded beds, pore-pressure diffusion follows a simple linear diffusion model, with a constant value for the diffusion coefficient. In contrast, the pore-pressure diffusion coefficient in initially expanded beds is pressure dependent, evolving as long as pore pressure diffuses within the granular mixture. As shown by equation 4.4, D is a function of permeability (k), porosity (ϕ), fluid viscosity (μ), mixture compressibility (c_ϕ) and fluid compressibility (c_f). In our experiments (as well as those using wet debris-flow material or shallow air-particles mixtures), fluid can be treated as uncompressible, thus c_f is nearly constant. Furthermore, changes in fluid viscosity are negligible, although fine particles (dust or colloids) can increase the bulk viscosity in some geophysical mixtures [*Iverson*, 1997; *Major*, 2000]. Though permeability appears relevant for the reference pressure diffusion coefficients (*Do*, *Dm*), our numerical model shows that changes in permeability can be neglected, even when permeability varies significantly under small changes of porosity. Note that, the dependence of D on k and ϕ has been previously addressed by *Iverson* [1997] and *Major*, [2000].

Major [2000] showed that for a wide range of debris flow mixture permeabilities (10^{-9} m² to 10^{-14} m²) low pore-pressure diffusivities are not solely influenced by low permeability. High mixture compressibility (or porosity compressibility) in initially dilated mixtures under low effective stress also influences pore pressure diffusion and contributes to low diffusivity coefficients. In some mixtures, changes in compressibility can outweigh changes in permeability [*Major*, 2000]. In our experiments, using initially expanded beds, mixture compressibility strongly affected pore-pressure diffusion. As shown by equation 4.16, the dimensionless pore-pressure diffusion coefficient, D^*, is a function solely of the pore compressibility ($c_\phi^* = \alpha p^*$). In this study $c_\phi \sim 10^{-4}$ Pa^{-1}, that is, one order of magnitude higher than in *Major* [2000] ($c_\phi \sim 10^{-5}$ Pa^{-1}). This explains why the linear model applies better to the debris-flow mixtures tested by *Major* [2000] than to our experiments. For non-expanded mixtures, where $c_\phi \approx 0$, the linear model provides good results. As shown by equations 4.13 and 4.14, permeability changes, represented by the permeability compliance (γ), are multiplied by $c_{fR} P_L$. Therefore, permeability changes (γ) do not contribute to the pore-pressure diffusion process when fluid compressibility effects are negligible ($c_{fR} P_L << 1$), As a result, changes in porosity do not just outweigh changes in permeability, but instead changes in permeability are typically negligible when $c_{fR} P_L << 1$.

The parameter $c_{fR} P_L$ shows that pore-fluid compressibility effects are not solely a function of fluid compressibility, but are also a function of effective stress, which in our case scaled with the lithostatic pressure P_L. Thus, even for low compressible fluids, fluid compressibility could affect pore-pressure diffusion in highly confined systems, such as deep groundwater or hydrocarbons

reservoirs [*Yilmaz et al*., 1994., *Hummel*, 2008], in which case permeability compliance could become relevant. However, this might not be applicable for most unconfined, self-consolidating mixtures such as natural granular mixtures.

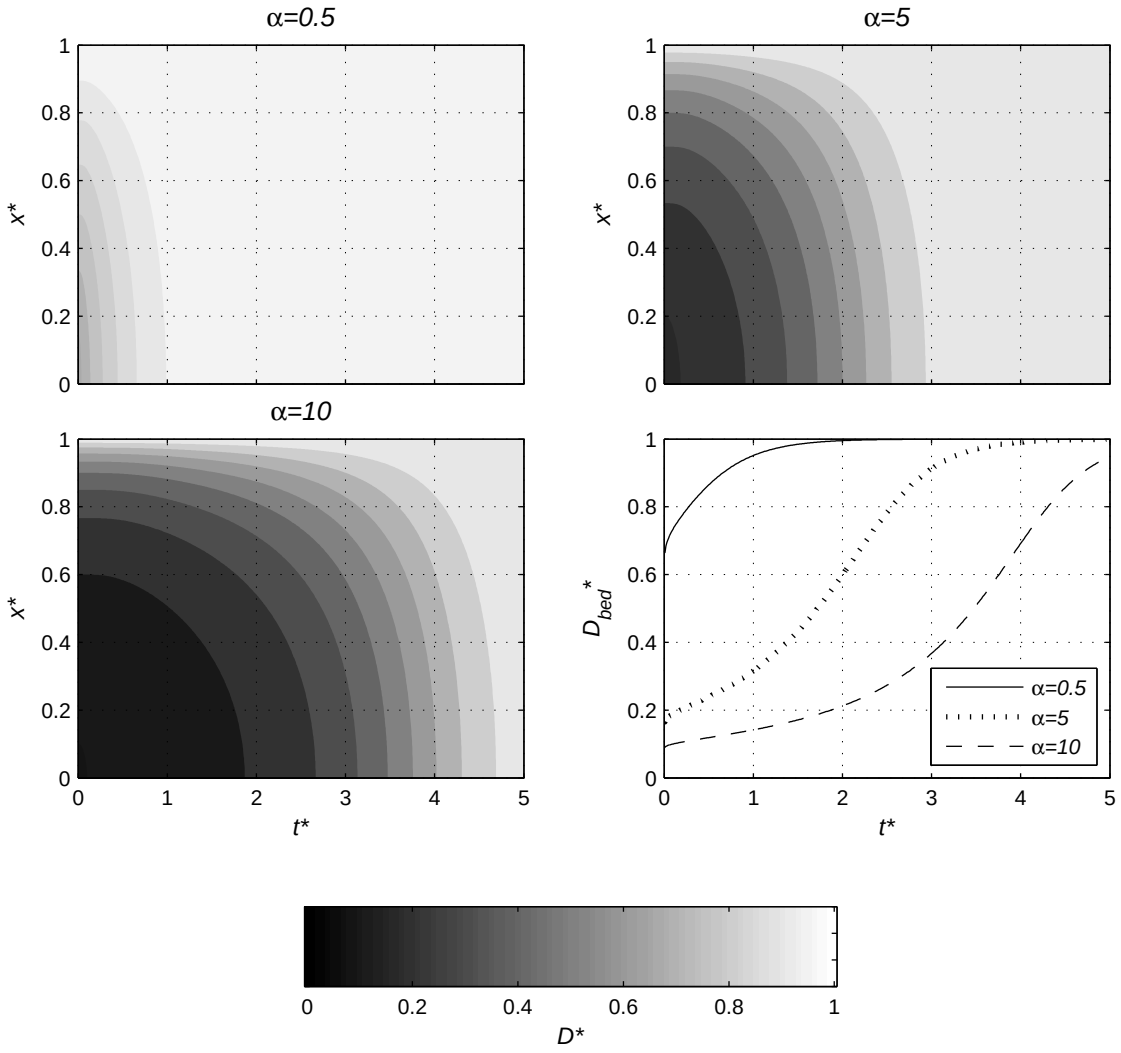

Figure 4.10. Vertical profile of the diffusion coefficient time evolution (*D*)* for an initially fully fluidized granular bed and different α values using equation 4.19. Values of α vary in the range of 0.5 to 10 (Figure 4.7). The solution for $\alpha = 0$ (i. e. linear diffusion) is not shown, as in this case *D** is constant and equal to 1. D_{bed}* at the right bottom corner represents the dimensionless fluid diffusion coefficient at the base of the granular column. The color bar represents values of *D**.

4.5.2 Time scales of the pore-pressure diffusion process

For estimating pore-pressure diffusion time scales in our experiments, we calculate T^*_D, the dimensionless time required for basal pore pressure to reach 1% of the initial degree of fluidization (i.e., $p_o^* = 0.01\ \beta o$), according to the proposed numerical model. This cutoff value was chosen arbitrarily for convenience since the diffusion model decreases asymptotically to

p^*=0. For calculations, $\alpha = 0$ was considered when $0 \leq \beta o \leq \beta o_c$. In the range $\beta o_c \leq \beta o \leq 1$, it was supposed that α varied linearly from 0 to 10. The obtained diffusion timescale has a constant value $T^*_D = 1.84$ for $0 \leq \beta o \leq \beta o_c$. In contrast, once the bed is expanded ($\beta o_c \leq \beta o \leq 1$), T^*_D increases linearly up to 4.74 (βo =1, fully fluidized mixture). Thus, a break in the tendency occurs when $\beta o > \beta o_c$ with a maximum about 2.6 times greater than the constant value of T^*_D (in the range $0 < \beta o < \beta o_c$) when $\beta o = 1$. A similar break in tendency was previously reported for the run-out distance of initially aerated granular flows of almost the same particle mixtures [*Montserrat et al*., 2007; *Roche et al*., 2008]. The run-out distance showed a little increase between $0 < \beta o < \beta o_c$, but importantly increased to almost twice that observed for $\beta o = \beta o_c$, when $\beta o = 1$. This result suggested that the initial degree of fluidization, and related mixture expansion when $\beta o > \beta o_c$, controlled most of the flow dynamics and run-out distance. It is worth mentioning that for comparison with experiments of *Roche et al*. [2008], it is assumed that βo_c was reached at ~*Umf* and complete fluidization (i.e. βo=1) was obtained at ~*Umb*. In complementary experiments, *Roche et al*. [2010] measured the pore pressure at the base of initially fluidized and expanded flows (cf. $\beta o = 1$). They reported that the duration of pore pressure diffusion was close to the duration of the flows and also to the duration of pressure diffusion in defluidizing static columns of similar heights. As a matter of fact our method predicts, at $\beta o = 1$ ($T^*_D \sim 5$), that the duration of pressure diffusion is close to the flow duration reported by *Roche et al*. [2010]. This supports the idea that the dynamics of initially fluidized flows are controlled by overall mixture compaction and associated pore pressure diffusion, as observed in our self-consolidating static experiments.

The time scale for pressure diffusion cannot be directly extrapolated to other conditions, as it is mixture dependent. However, because α is related only to the pore compressibility, it should be a function of the range of dilation or compaction that can be attained for a given mixture. In case of quasi-static consolidation, α scales with the initial degree of expansion, so that more expanded mixtures attain larger values of α. The nature of the interstitial fluid does not appear to affect the value of α, but as our experiments focused on just one type of air-particle mixtures this needs further research. It is also known that the amount of initial expansion of gas-fluidized mixtures depends on the grain size distribution. In particular, the mixture expansion increases with the amount of fine particles. For instance, ash-rich pyroclastic flow materials, with particle diameters in the range ~ 1 μm to 250 μm, can have maximum expansions near 50% [*Druitt et al*., 2007¸ *Girolami et al*., 2008], which would result in larger values of α than those determined here. Furthermore, increasing the amount of fines reduces the mixture permeability by clogging connected pores and inhibiting the ease of fluid flows. Thus, the reduction in permeability due to fine particles can effectively reduce the reference pore-pressure diffusion coefficient, thus increasing the time needed to diffuse the excess pore-fluid pressure and even in non-expanded mixtures [*Major*, 2000; *Lorences et al*., 2003].

4.5.3 Insights into geophysical granular flow processes

In initially expanded granular mixtures, our results highlight the effects that mean mixture compaction has in retarding pore-fluid pressure. Pore-fluid pressure measured at the base of granular flows often reveals a complex behavior [*Iverson* 1997; *Iverson et al*., 2010; *Roche et al*.,

2010]. Our study, however, suggests that initial material expansion (due to a certain degree of fluidization) may explain much of the bulk flow dynamics in small-scale, fine-grained, mono-disperse granular flows with low pore-pressure -diffusion coefficients (D ~ 0.01 - 0.02 m²/s). Note that these values of D are in the range inferred for thin ash-rich pyroclastic flows on the basis of their material permeability [*Druitt et al*., 2007]. For debris flows, pore-pressure-diffusion coefficients range between $D \sim 10^{-7}$ - 10^{-3} m²/s [*Iverson*, 1997; *Major et al*., 1997; *Major and Iverson*, 1999; *Major*, 2000]. Thus, in wet flows, pore-pressure diffusion takes longer than in air-particle mixtures of similar size. Fine particles clearly affect the value of D, effectively retarding pore-pressure diffusion, as shown experimentally for debris flows [*Major and Iverson*, 1999; *Major*, 2000] and pyroclastic-flow material [*Druitt et al.*, 2007]. Although our mono-disperse air-particle mixtures lack the range of grain size distribution typical of most natural geophysical flows, fine group-A-type air-particle mixtures may replicate most of the observed characteristics of pore-pressure diffusion in natural flows containing large amounts of fines. Despite the reduced scale of our experiments (H < ~ 0.5 m) compared to natural geophysical flows, our results highlight the mechanisms retarding pore-fluid-pressure diffusion. Note, however, that the size of some of the smaller flows in nature is of the same order of that of our experiments. For instance, distal deposits of pyroclastic flows are commonly a few decimeters thick [*Druitt*, 1998; *Freundt et al.*, 2000; *Wilson and Head*; 1981]. In this context, our findings should apply well to pyroclastic flows with D values similar to those presented in this paper.

In the present study, we assumed that pore-fluid compressibility effects are negligible even when the pore fluid is air, which is a consequence of the shallow mixture heights in our experiments. This assumption is appropriate for wet debris flows (or any water-particle mixture), but may not be valid for thick gas-particles mixtures such as large pyroclastic flows and snow avalanches. Figure 4.11 shows values of the product $c_{fR} P_L$ for our experimental granular mixtures and natural geophysical flows. As in air particle-mixtures the fluid compressibility can be calculated as $c_{fR} = 1 / (P_{atm} + P_L)$, in thick flows, where $P_L >> P_{atm}$, the product $c_{fR} P_L$ approaches 1. For natural flows shown in Figure 4.11, we considered typical values of mixture densities to estimate P_L. Values of the product $c_{fR} P_L$ in our experiments are comparable to those of thin pyroclastic flows (H < 1 m). For thick pyroclastic flows (H > 10 m) $c_{fR} P_L \sim 1$, implying that pore-fluid pressure compressibility is not negligible and that the permeability compliance (γ) has an important effect on the pore-pressure diffusion process. In particular, if $c_{fR} P_L$ is non-negligible, the quadratic term on the right hand side of equation 4.13 may promote pore-fluid-pressure generation. Furthermore, the exponential term affecting the pore-pressure diffusion coefficient (equation 4.14) can become non-negligible, and thus can accelerate the diffusion process. Detailed effects of the permeability compliance on pore-pressure diffusion are beyond the scope of this work.

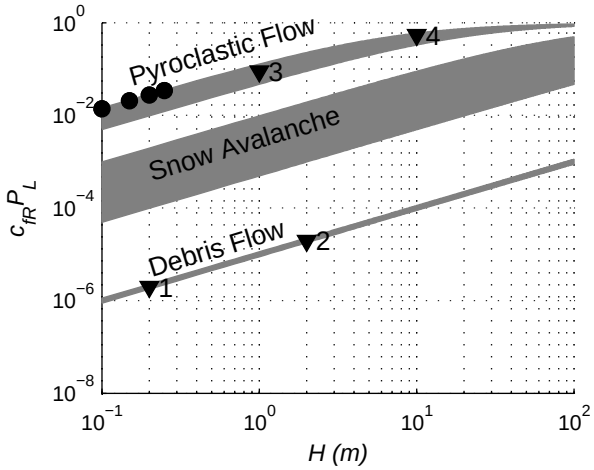

Figure 4.11. Estimates of $c_{fR}\, P_L$ for different types of geophysical granular flows and our laboratory experiments. Reference values of the pore fluid compressibility (c_{fR}) are assumed to be 5×10^{-10} Pa^{-1} and 10^{-5} Pa^{-1} in the case of water-particle (debris flow) and air-particle (pyroclastic flows and snow avalanches) mixtures, respectively. Mixture densities are assumed within the range 1800 - 2300 kg/m³ for debris flows [*Iverson*, 1997; *Iverson and Vallance*, 2001; *Hausser*, 2002], 10 - 1000 kg/m³ for snow avalanches [*McClung and Shaerer*, 1993; *Turnbull and McElwaine*, 2007], and 500 - 1500 kg/m³ for pyroclastic flows [*Druitt*, 1998; *Freundt et al*., 2000]. Flow heights, *H*, are in the range 0.1 - 100 m. Black dots represent the values of $c_{fR}\, P_L$ in the present experiments, while black triangles correspond to estimations of $c_{fR}\, P_L$ values computed out of the granular flow data reported by *Iverson and Denlinger*, [2001]: 1) experimental USGS debris flows, 2) Yake Dake, debris flow, 3) small-volume pumice pyroclastic flow deposits of Mount St. Helens and 4) Elm rock Avalanche.

4.6 Conclusions

Pore-pressure diffusion in initially aerated, air-particle mixtures was investigated through experiments and numerical modeling. Experiments recorded the decay of the pore-fluid pressure at the base of an initially aerated granular column. Pressure data were compared with a 1D numerical model obtained by coupling the continuity equation with the Darcy equation for estimating air velocity and assuming negligible particle relative motion (quasi-static consolidation). A dimensional analysis shows that fluid compressibility and changes in permeability can be neglected for modeling our experiments. Thus, the proposed pore-pressure equation reduces to a simpler diffusion equation with a variable diffusion coefficient, *D*. When pore volume changes are negligible (no expansion or contraction), *D* is constant and pore-pressure can be modeled using a simple linear diffusion equation. This approach has been extensively used in previous works for the analysis of quasi-static soil consolidation and it provided good results for predicting pore-fluid pressure evolution in our experimental mixtures that were not initially expanded. On the other hand, when our mixtures were initially expanded, non-linear effects due to mixture consolidation became important during the pore-pressure diffusion process.

Porosity compressibility (c_ϕ) appears to be a key parameter for estimating the value of the non-linear diffusion coefficient. Large values of c_ϕ reduce the reference pore-pressure-diffusion

coefficient ($D \sim 1 / c_\phi$) and retard pore-pressure diffusion in granular mixtures. Thus, highly dilative (and then contractive) mixtures, with associated large values of c_ϕ, can maintain excess pore-fluid pressure for longer durations compared to less compressible mixtures. Pore-pressure diffusion during mixture compaction in our experimental static columns, occurred over time scales comparable to durations of experimental initially fluidized granular flows of similar heights [*Roche et al*., 2008, 2010], suggesting that our model for static configurations can be applied to flowing mixtures. This is being tested with new experimental results. Although permeability is an important variable that controls the reference pore-pressure diffusion coefficient, changes in permeability were negligible in our experiments because they where outweigh by changes in porosity and because pore-fluid compressibility effects were negligible. Our results highlight that porosity compressibility can effectively retard pore-pressure diffusion in initially expanded dry-granular mixtures and depends chiefly on changes in pore volume size, so that particle-size distribution is important in controlling pressure diffusion. However, because our experiments focused on mono-disperse mixtures, this conclusion deserves further research.

Acknowledgment: The first author acknowledges the financial support from project Mecesup UCH 310, in the form of a PhD fellowship and Departamento de Postgrado y Postítulo de la Vicerrectoría de Asuntos Académicos, Universidad de Chile, as a foreign residence fellowship. This work was supported by ECOS-CONICYT Projects C06U01 and C11U01, Institut de Recherche pour le Développement (IRD, France), ANR (France), Departamento de Ingeniería Civil, Universidad de Chile and Advanced Mining Technology Center (AMTC). The authors acknowledge the valuable comments made by the Associate Editor during the review process.

Chapter 5

5 Run-out of initially fluidized dam-break granular columns on slopes.

This chapter, authored by Santiago Montserrat, Aldo Tamburrino, Olivier Roche and Yarko Niño, is in the form of research article in preparation to be submitted to *Geophysical Research Letters*.

Abstract

Interstitial pore fluid pressure has important effects on the dynamics of many geophysical granular flows and is particularly expected to increase their mobility through severe reduction of particle interactions. Here we investigate in dam-break experiments the run-out of granular flows, on slopes of various angles, generated from the collapse of granular columns fluidized at different degrees. The flow run-out mainly depends of the initial degree of fluidization, βo, defined as the ratio of the measured basal pore fluid pressure over the lithostatic pressure of the column. An important run-out increase is observed for $\beta o > \beta o_c \sim 0.94$ that marks the onset of bed expansion.

This suggests that the pore pressure diffusion timescale in the deflating flows increases with the initial material expansion, which, according to previous studies on static granular columns, is due to high values of the mixture compressibility coefficient. For slope angle lower than the repose angle of the granular material, the flow run-out normalized by the run-out of non-fluidized flows is independent of both the slope angle and the initial column height-to-length ratio, depending only of the degree of fluidization. The dimensionless flow run-out was found to vary with the power of the column height-to-length ratio, being independent of the flume slope and initial degree of fluidization.

5.1 Introduction

Geophysical granular flows consist of fluid-particle mixtures driven by gravity that propagate over topography of various slopes. Typical examples include debris flows, lahars, pyroclastic flows, and snow avalanches. Predicting the run-out of these flows is critical for land-use management and risk assessment in numerous industrial operations. Based on the observation of past events, some authors obtained empirical relationships that correlate the flow run-out with different other parameters such as the channel geometry and flow volume [*Hungr et al*., 1984; *Rikenmman* 1999]. The interstitial fluid may play an important role in flow mobility by reducing frictional stress between the particles according to Terzaghi's stress principle. Thus, excess pore fluid pressure (i.e. over hydrostatic pressure) can effectively reduce energy dissipation caused by particle interactions and enhance the flow mobility. Excess pore fluid pressure arises in natural flows because of an interstitial upward fluid flux and/or particle settling and it can persists up to complete deposition [*Major and Iverson,* 1999; *Major*, 2000; *Iverson*, 1997]. Measurements in experiments at different scales and in the field have revealed the existence of excess pore fluid pressure well above hydrostatic at the base of fluid-particle flows, even at relatively long travel distances from the source [*Iverson*, 1997; *Major and Iverson*, 1999; *Major*, 2000; *McArdell et al*., 2007; *Iverson et al*., 2010, *Roche et al*., 2010]. This highlights the importance that pore pressure has in promoting long run-out distances even on small slopes.

Recent dam-break experiments on air-particles flows demonstrated that the initial fluidization of the mixture enhances the flow run-out in horizontal flumes [*Roche et al*., 2008, 2010, *Roche*, 2012]. For instance, the run-out of initially fully fluidized mixtures is about twice that of non-fluidized ones. In this study, we investigate similar experiments and report new results on the flow run-out as a function of a range of initial degrees of fluidization and of different flume slopes. The flow run-out is assumed to depend primarily on the pore pressure diffusion timescale, which may vary considerably as a function of the initial material expansion as shown by experiments on static defluidizing granular columns [*Montserrat et al*., 2012].

5.2 Experimental device and procedure

The experimental device consisted of a 300 cm-long and 20 cm-wide tilting flume connected to a 20 cm-wide horizontal head reservoir of variable length, x_o (from 5 to 20 cm), equipped with a sluice gate and where particles were initially rested. The entire experimental device is made of transparent plexiglass to permit flow visualization (see Figure 3.1. Only the flume can be tilted. The reservoir remained always horizontal due to the fluidization mechanism).

Particles in the reservoir could be aerated at different degrees, from none to complete fluidization, by introducing a vertical air flux through a basal 10 mm-thick porous plate (with mean pore size of 20 μm) that ensured homogeneous fluidization. Air was supplied by a compressor and dried before entering a wind box filled with coarse particles (3 mm) in order to reduce the volume of air. The granular bed is termed *fluidized* when the drag force exerted by the vertical air flow entirely supports the weight of the particles [*Roche et al*., 2008, 2010; *Montserrat et al*., 2012]. In order to ensure reproducibility of the experiments, particles were fluidized for one hour with dry air in order to eliminate mild cohesion caused by ambient moisture.

The granular flow along the flume was generated by the sudden release (<0.1 s) of the reservoir gate. Piezoresistive pressure sensors (ICSensors^{TM}, model 145N), as used by *Roche et al*. [2010], were located on one side wall of the reservoir at the lowest position and measured the basal pore fluid pressure before and during flow motion. The sensors measured pressure in the range 0 to ~34.5 kPa (0 - 5 psi) and were placed inside an aluminum casing covered by grids of 38 µm-aperture. When the gate was released, the air flux was instantaneously stopped by the action of a solenoid valve connected to an electric switch activated by the gate movement. Measurements showed that pressure inertia effects inside the windbox dissipated in less than 0.01 sec, so that during flow motion the porous plate can be assumed as an impermeable wall [*Montserrat et al*., 2012].

The particles in the experiments were the same than those used in previous studies on dam-break granular flows [*Roche et al*. 2008, 2010; *Roche*, 2012] and were similar to those used by *Montserrat et al*. [2012] for characterizing the defluidization properties in static granular columns. Despite the similarity in size, it is noted that the mean particle diameter used by *Montserrat et al*. [2012] (60 µm) was slightly smaller than those considered here. In present experiments, nearly spherical glass beads (Ballotini, Potters Industries), with a density ρ_p = 2500 kg/m^3, a mean diameter of 75 µm (ranging between 60 µm to 90 µm), and a repose angle $\phi \sim 28°$, were used. The bulk density of a granular columns was ρ ~ 1450 kg/m³. In terms of their fluidization properties, the particles belong to group A according to *Geldart's* (1973) classification. This means that beds of these particles expand homogeneously at gas velocities (defined as the flow rate divided by reservoir horizontal area) between the minimum fluidization velocity at which the weight of the particles is counterbalanced (*Umf*) and the minimum bubbling velocity (*Umb*) at which gas bubbles form [*Gibilaro*, 2001; *Roche et al*., 2004].

5.3 Results

5.3.1 Fluidization characteristics and onset of bed expansion

We quantify the degree of fluidization at the beginning of the experiments as $\beta o = p_o / P_L$, where p_o is the measured pore fluid pressure at the base of the granular column just before gate opening, and $P_L = \rho g h_o$ is the lithostatic pressure where ρ is the bulk mixture density, g is the gravity acceleration, and h_o is the non expanded column height. The fluidization and subsequent pore pressure diffusion (i.e. defluidization) process of static columns of mixtures similar to those

investigated here was previously studied in detail by *Montserrat et al*. [2012]. They showed that pressure diffusion obeys a simple linear diffusion model [e.g., *Iverson and Denlinger*, 2001] for fluidization degrees, βo, lower than a critical value βo_c corresponding to the onset of bed expansion. For $\beta o > \beta o_c$, non linearities in the pore pressure diffusion coefficient, principally because of changes in the mixture compressibility due to grains rearrangement during consolidation, effectively retard pressure diffusion by reducing the effective diffusion coefficient. In this range of fluidization degrees (expanded columns), the linear pore fluid pressure diffusion model fails in representing pore pressure [*Montserrat et al*., 2012].

For our mixtures, the onset of bed expansion occurs at $\beta o = \beta o_c \sim 0.95$ whereas maximum expansion of about 5 %, or $\Delta h^* = 0.05$ occurs at $\beta o = 1$ (Figure 5.1). Here, $H^* = (he - ho) / ho$, where *ho* is the initial non-expanded height and *he* is the expanded bed height. It is noted that these values are slightly different than those reported by *Montserrat et al*., [2012] ($\beta o_c \sim 0.90$, $\Delta h^* = 0.1$), which is most likely due to a mean grain size slightly smaller in their experiments (~60 µm) than in ours (~75 µm).

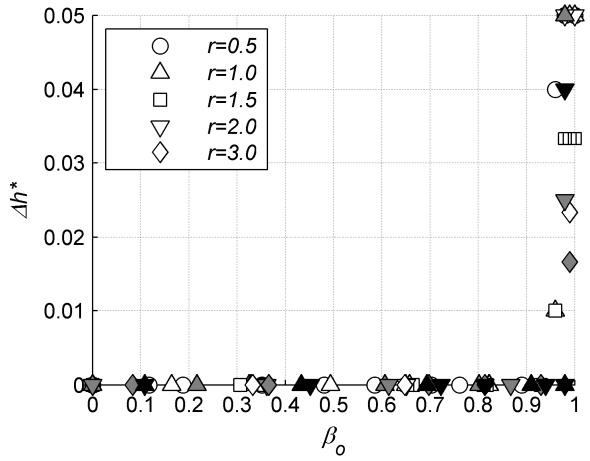

Figure 5.1. Bed expansion as a function of the dimensionless initial fluidization rate, βo, for different initial bed heights (h_o). $\Delta h^* = (he - ho) / ho$, where *ho* is the initial (non-expanded) height and *he* is the expanded bed height. Bed expansion occurs when $\beta o > \beta o_c \sim 0.95$. Open symbols correspond to experimental runs in the horizontal flume configuration, grey symbols correspond to flume slope angles of $\theta = 9.7°$ and black symbols, the case $\theta = 17.0°$.

5.3.2 Flow run-out

Our experiments differ from those of *Roche et al*. [2008, 2010] and *Roche* [2012] in two main aspects: 1) the air supply is stopped just before opening the sluice gate and 2) experiments are carried out for three different slope angles, θ ($\theta = 0°$, 9.7° and 17.°), lower than the repose angle of the material. Note that we also measure the flow run-out for the whole range of initial fluidization degrees ($0 \leq \beta \leq 1$), in more detail than *Roche et al*. [2004].

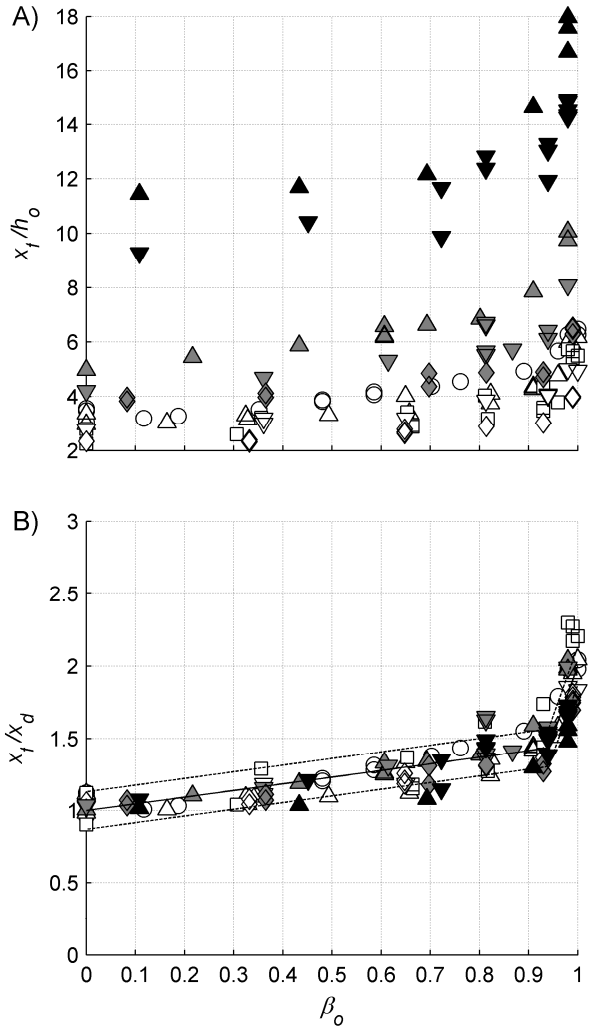

Figure 5.2. Dimensionless flow run-out as a function of the initial degree of fluidization, βo, using two different length scales. A) Flow run-out is made dimensionless by means of the initial column height (h_o) [*Roche et al*., 2008] and B) flow run-out is normalized by using the corresponding flow run-out of non-fluidized mixtures, $x_d = x_f$ ($\beta o = 0$). The solid line in Figure B represents the best fit obtained by equation 5.1, while dashed lines denote the standard deviation of experimental data ($\pm\sigma$).

Despite the initial air flow is stopped at the beginning of the experiments, our dimensionless run-out values in the horizontal channel configuration are close to those reported by *Roche et al*. [2008], which are x_f / h_o (where x_f is the flow run-out measured from the gate) ~ 2 – 3 for non-fluidized flows, 4.5 - 5 for flows initially fluidized at *Umf* (i.e. at the onset of bed expansion, $\beta o = \beta o_c \sim 0.95$), and 5.5 - 6 at *Umb* (i.e. maximum expansion, $\beta o \sim 1$) (Figure 5.2A). This shows that the flow dynamics, that depend on both pore pressure diffusion and advection and that control the flow run-out, are independent on whether fluidization at the source is continuous during the experiment or not. Major differences due to changes in the experimental procedure compared to *Roche et al*. [2008], however, can be seen in the deposit morphology. The

surface slope of the deposits in our experiments steadily decreases downstream, whereas the deposits are flat in the reservoir and have a bulge at the entrance of the channel in experiments of *Roche et al.* [2008] due to continuous fluidization and late particle motion after the main flow body has stopped, respectively.

Our experiments provide detailed description of the experimental flow run-out for different degrees of fluidization and slope angles. For a given slope angle, the dimensionless flow run-out, x_f / h_o, linearly increases with βo for initially non expanded beds (at βo < ~0.95), and then increases at higher rates with βo for initially expanded beds (at $\beta o > \beta oc$) (Figure 5.2A). This break in tendency at the onset of bed expansion coincides with that observed in the pore pressure diffusion timescale of aerated granular columns [*Montserrat et al.*, 2012]. Rescaling the run-out values with those of non-fluidized flows (at $\beta o = 0$), x_d, tends to collapse the data on a single curve independently of *So* and *r* (Figure 5.2B). Assuming that x_f / x_d can be fitted by two straight lines (and imposing $x_d / x_d = 1$), the run-out can be estimated as:

$$\frac{x_f}{x_d} = \max\left(m_1\beta_o + 1\,, m_2\beta_o + 1 + \beta_{oc}\left(m_1 - m_2\right)\right) \pm \sigma \qquad (5.\ 1)$$

where m_1 and m_2 represents the slope of the straight lines fitting the data in the ranges $0 < \beta o < \beta o_c$ and $\beta o_c < \beta o < 1$, respectively, and σ corresponds to the experimental error, assumed to be the standard deviation of the data. The values of the constants m_1, m_2 and βo_c are those that minimize the root mean square value of the data dispersion of equation 5.1, so that $m_1 = 0.47$, $m_2 = 9.40$, $\beta o_c = 0.94$, and $\sigma = 0.13$. Figure 5.2B shows that x_f / x_d increases from 1 to 1.44 in the range $0 < \beta o < \beta o_c$ and then abruptly increases up to ~ 2 when $\beta o = 1$. It also shows that x_f / x_d increases with βo at a rate about 20 times greater at $\beta o > \beta o_c$ than at $\beta o < \beta o_c$.

Previous experimental studies on dam-break, non-fluidized granular flows over horizontal slopes, though using particles coarser than the ones used here [*Lube et al.*, 2004; *Lube et al.*, 2005; *Lajeunesse et al.*, 2005], demonstrated that the dimensionless flow run-out, normalized by either the column length (x_o) or column height (h_o), scales as a power law of *r*, $\sim \lambda\, r^n$. Noting that $x_d / x_o = x_d / h_o\, r$, both scalings are equivalent. Recent experiments regarding the axisymmetric collapse of initially fluidized granular columns over a horizontal plane demonstrate that the same power law function is valid for scaling the flow run-out [*Roche*, 2012], demonstrating that this scaling law is not only typical of dry granular flows. It was demonstrate that the exponent *n* is invariant respect to de initial degree of fluidization of the granular column; but it decreases at increasing *r*. The column fluidization increases the coefficient λ, which takes into account the increase in run-out because the reduction in flow resistance [*Roche*, 2012]. The run-out of non-fluidized flows (at $\beta o = 0$) using x_o as the characteristic length scale is shown in Figure 5.3. The dimensionless run-out, x_d / x_o, as a function of *r* is re-scaled by R^{-1} $(1\text{-}sin\theta)$, with $R = \tan\phi / (\tan\phi - \tan\theta)$, which shows good data collapse independently of the slope angle. The parameter *R* accounts for flow mobility over slopes, as it takes into account the repose angle and the slope angle. When $\theta \rightarrow \phi$, $R \rightarrow \infty$, as the flow continues flowing and never stops in the channel. Analytical solutions in the context of thin layer (i.e., depth –averaged) models, strictly valid for small *r* ($r < 1$), shows that the dimensionless flow run-out is inversely proportional to the difference between the tangent of the effective friction angle (which it is not a material property,

instead a property of the flow) and the tangent of the bed slope, rather similar to our proposed scaling parameter R [*Lucas and Mangeney*, 2007; *Roche*, 2012]. The parameter $(1 - sin\theta)$ is defined to make comparable the flow run-out for different slopes with that of horizontal channel, so that when $\theta = 0$ then $R^{-1} (1 - sin\theta) = 1$.

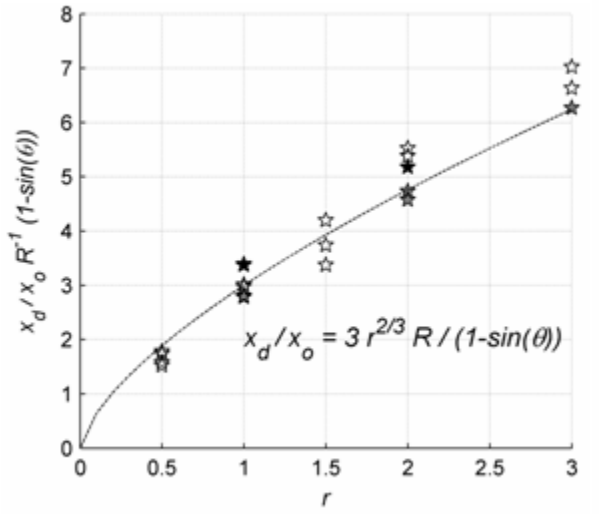

Figure 5.3. Dimensionless run-out of non-fluidized mixtures (i.e. $\beta o = 0$) normalized by the initial column length, x_o as a function of the initial column aspect ratio [*Lube et al*., 2004; *Lube et al*., 2005; *Lajeunesse et al*., 2005, *Roche*, 2012]. It is worth noting that $x_d / x_o = x_d / h_o$ r, and thus both scaling are equivalent. Dashed lines denote the fit indicated in each graph.

Figure 5.3 shows that $x_d / x_o \; R^{-1} \; (1 - sin \; (\theta)) \sim r^{2/3}$, which differs from previous experiments done with coarser particles on horizontal slopes that shows that $x_d / x_o \sim r$ at low aspect ratios ($r < \sim 3$) and $x_d / x_o \sim r^{2/3}$ for $r > \sim 3$ [*Lube et al*., 2004; *Lube et al*., 2005; *Lajeunesse et al*., 2005]. Our results agree with *Roche* [2012] findings respect that the same power law of r ($x_d / x_o \sim \lambda \; r^n$), valid to describe non-fluidized flows, serves to scale initially fluidized granular flows:

$$\frac{x_f}{x_o} \sim \frac{3R}{1-\sin(\theta)} m_i \; \beta_o \; r^{\frac{2}{3}} \qquad (5.2)$$

with $m_i = m_1 = 0.47$ when $0 < \beta o < \beta o_c$, and $m_i = m_2 = 9.40$ when $\beta o > \beta o_c$. As expected, the parameter n is invariant respect to changes in flume slope and the degree of fluidization of the granular column [*Roche*, 2012]. Instead, the parameter λ increases linearly with the initial degree of fluidization, $\lambda \sim m_i \; \beta o$. The parameter m_i highlights the importance of the initial degree of bed expansion in enhancing flow run-out.

5.4 Discussion

With initial fluidization at different degrees, the flow run-out scales with that of non fluidized flows (Figure 5.2B), so that the data collapse on a single curve independent of the slope angle and initial column aspect ratio, and mainly depends on the initial degree of fluidization (βo). An important break in tendency occurs at $\beta o = \beta o_c \sim 0.94$, which coincides with the onset of bed expansion. For $\beta o > \beta o_c$ an important increase in flow run-out is observed respect to non expanded mixtures. This suggests that the reduction in the effective pore pressure diffusion coefficient due to continuous mixture consolidation following initial expansion, as reported by *Montserrat et al*. [2012], can effectively increase the pore pressure diffusion timescale and hence the flow run-out. This is also in agreement with measurements of *Roche et al*., [2010] that reveal high pore fluid pressure at the flow base in the case of initial material expansion, so that 70% to 100 % of the weight of the particles is supported by pore pressure.

As shown previously in dam-break experiments of non-fluidized or fluidized granular flows on horizontal slope, in both 2D and axisymmetric geometries, the dimensionless flow run-out scales with a power law of the initial aspect ratio r, $x_f / x_o \sim \lambda\, r^n$, with n = 2/3 constant. The parameter λ represents the observed dynamics respect to the increasing flow run-out with the initial degree of fluidization and bed expansion, as it varies linearly with $m_i\ \beta o$, with m_i representing the rate of increasing run-out in the non-expanded ($m_i = m_1$) and expanded ($m_i = m_2$) regimes.

In summary, initial mixture expansion caused by fluidization increases the pore pressure diffusion time scale and, other variables being equal, causes larger flow run-out. Implications of this result in nature are evident, as expanded fluid-particle mixtures at the source of initiation of geophysical granular flows results common. For example: loose soils at debris flows initiation areas,or pyroclastic flows initiated by the sedimentation of diluted ash cloud. Even when non-expanded, evidence about the initiation of compacted debris flows suggested that prior to flow initiation soils dilate to acquire loose-soils characteristics [*Gabet and Mudd*, 2006]. Thus, the increase in run-out in initially fluidized-expanded mixtures observed in this experimental work has important implications in the dynamics of geophysical granular flows, and may help to explain the observed long-lived pore-fluid pressure in both experimental and natural granular flows. The basal pore fluid pressure evolution generated by granular flows in the dam-break configuration for the whole range of fluidization degrees and different slopes is now being investigated by our group.

5.5 Conclusions

Experimental results regarding the flow run-out of initially fluidized (type A) granular mixtures show a strong dependence on the initial degree of fluidization as well as the initial column aspect ratio. When the flow run-out is normalized by the run-out of non-fluidized flows (i.e. $\beta o = 0$), a unique behavior relative to the initial degree of fluidization, independent of the initial column aspect ratio (r) and flume slope (So), is observed. Our results shows that the dimensionless run-out, normalized by the initial column length, vary as a power law of r, independently of the initial degree of fluidization, as shown previously by *Roche* [2012]. A distinct change in the trend of

flow run-out evolution was observed at the onset of bed expansion, which is accounted by the proportionality constant of the obtained power law. For fluidization degrees exceeding those corresponding to the onset of bed expansion, flow run-out measurements, despite their linearity, increase with βo at a rate 20 times greater compared to the case of initially non-expanded mixtures. This change in their evolution compares well with different pore pressure diffusion processes for expanded and non-expanded mixtures, observed by *Montserrat et al*. [2012].

Acknowledgements: The first author acknowledges the financial support from project Mecesup UCH 310, in the form of a Ph.D. fellowship and Departamento de Postgrado y Postítulo de la Vicerrectoría de Asuntos Académicos, Universidad de Chile, as a foreign residence fellowship. This work was supported by ECOS-CONICYT Projects C06U01 and C11U01, Institut de Recherche pour le Développement (IRD, France), ANR (France), Departamento de Ingeniería Civil, Universidad de Chile and Advanced Mining Technology Center (AMTC). This is Laboratory of Excellence *ClerVolc* contribution n° X.

Chapter 6

6 Conclusions

The present thesis has successfully addressed as set of different experiments in order to study different relevant features of granular flows. Dam-break experiments of initially fluidized granular columns, as well as pore pressure measurements in initially fluidized granular columns, bring new insights into the physics of granular flows. Because we dealt with air-particle mixtures, with particles belonging to group A according to *Geldart's* classification, our results have important implications for mechanics of dense ash-rich pyroclastic flows. The results show that slightly expanded fluidized granular columns can propagate similarly to their inertial water counterpart for most of their emplacement. Flows occur in three phases controlled by the time scale of free fall of the column (the ratio of initial column height to gravity): 1) column collapsing phase, 2) constant velocity phase and 3) stopping phase. During the constant velocity phase, initially expanded fluidized mixtures, as well as water flows, show front flow velocities near 1.5 times greater than those of non-fluidized flows. Basal pore fluid pressure measurements at the bottom of the granular flows along the flume highlight that, in the case of initially slightly expanded fluidized granular flows, high pore fluid pressures persisted for most the flow propagation: 70 to 100% of the weight of the particles was supported by pore pressure. These results support the idea that pore fluid pressure can significantly reduce inter-particle friction, providing an explanation for the observed inertial fluid-like behavior exhibited by initially expanded-fluidized flows induced in the experimental flume.

Experimental measurements as well as numerical modeling of the decay of basal pore fluid pressure of an initially aerated granular column show marked differences depending on whether

the column was initially expanded or not. For unexpanded mixtures, the decay of pore pressure follows a simple linear diffusion model with a constant pore pressure diffusion coefficient, an approach extensively used for the analysis of quasi-static soils consolidation. On the contrary, for initially expanded mixtures, non-linear effects derived form the continuous mixture consolidation reduced the effective diffusion coefficient, delaying pore pressure diffusion with respect to initially non-expanded columns. In this expanded regime, the simple linear diffusion model is not applicable. Instead, a non-linear diffusion model with a variable pore pressure diffusion coefficient was necessary to explain experimental data. Porosity compressibility appears as the key parameter affecting the pore pressure diffusion coefficient. Surprisingly, permeability changes appear negligible for the pore pressure diffusion process, even when permeability largely changes with porosity. Flow kinematics correlates well with fluidization properties of the granular mixture. It has been shown that the flow run-out increases with the initial degree of fluidization, but increases at a higher rate after fluidization surpass the onset of bed expansion. This means that the reduction in the pore fluid diffusion coefficient due to the initial mixture expansion significantly contributes to the flow mobility. This result is in good agreement with our observations indicating that high pore fluid pressure is long-lived in granular flows. Flow run-out shows to vary as a power law function of the initial column aspect ratio, independently of the initial degree of fluidization and flume slope. The proportionality coefficient of the power law synthesizes most of the physics regarding the initial degree of fluidization. The increment in this parameter with the initial degree of fluidization highlights the ability of pore fluid pressure in decreasing particle-particle interactions.

7 References

Aharonov, E. and D. Sparks. (1999), Rigidity phase transition in granular packings, *Phys. Rev. E. 60* (*6*), 6890-6896, doi:10.1103/PhysRevE.60.6890.

Ancey, C. (2007), Plasticity and geophysical flows: A review, *J. Non-Newt. Fluid Mech., 142*, 4-35.

Ancey, C. and H. Jorrot (2001), Yield stress for particle suspensions within a clay dispersion, *J. Rheol.* 45, 297.

Ancey, C. and P. Evesque (2000), Frictional-collisional regime for granular suspension flows down an inclined channel, *Phys. Rev. E. 62(6),*8349 - 8360, doi:10.1103/PhysRevE.62.8349

Armanini, A., H. Capart, L. Fraccarollo and M. Larcher (2005), Rheological stratification in experimental free-surface flows of granular-liquid mixtures, *J. Fluid. Mech., 532*, 269 - 319, doi:10.1017/S0022112005004283.

Armanini, A., L. Fraccarollo and M. Larcher (2008), Liquid-granular channel flow dynamics, *Powder Technol.,182*, 218 -2 27, doi:10.1016/j.powtec.2007.08.012.

Azanza, E., F. Chevoir and P. Moucheront (1999), Experimental study of collisional granular flows down an inclined plane, *J. Fluid. Mech., 400,* 199 – 227.

Bagnold, R. A. (1954), Experiments on a gravity-free dispersion of large solid spheres in a Newtonian fluid under shear, *Proc. Royal Soc. London A, 225*, 49-63.

Balmforth, N. J., and R. R. Kerswell (2005), Granular collapse in two dimensions, *J. Fluid Mech., 538*, 399-428.

Bareschino, P., A. Marzocchella, P. Salatino, L. Lirer, and P. Petrosino (2008), Self-fluidization of subaerial rapid granular flows, *Powder Technol., 182*, 323-333.

Bartelt, P., B. Salm, and U. Gruber (1999), Calculating dense snow avalanche runout using a Voellmy-fluid model with active/passive longitudinal straining, *J. Glaciol., 45*, 242-254.

Beget, J. E., and A. J. Limke (1988), Two-dimensional kinematic and rheological modeling of the 1912 pyroclastic flow, Katmai, Alaska, *Bull. Volcanol., 56*, 148-160.

Bell, S. W., R. C. Elliott, and M. H. Chaudhry (1992), Experimental results of two-dimensional dam-break flows, *J. Hydraul. Res., 30*, 225-252.

Biggs, M. J., D. Glass, L. Xie, V. Zivkovic, A. Buts, and M. A. C. Kounders (2008), Granular temperature in a fluidized bed, *Gran. Matt., 10*, 63-73, doi: 10.1007/s10035-007-0077-8.

Branney, M. J., and P. Kokelaar (1992), A reappraisal of ignimbrite emplacement: progressive aggradation and changes from particulate to non-particulate flow during emplacement of high-grade ignimbrite, *Bull. Volcanol., 54*, 504–520.

Branney, M. J., and B. P. Kokelaar (2002), *Pyroclastic density currents and the sedimentation of ignimbrites*, Mem. Geol. Soc. London, 152 pp.

Burtally, N., P. J. King, and M. R. Swift (2002), Spontaneous air-driven separation in vertically vibrated fine granular mixtures, *Science, 295*, 1877-1879.

Campbell, C. S. (1990), Rapid granular flows. *Annu. Rev. Fluid Mech., 22*, 57-92, doi: 10.1146/annurev.fl.22.010190.000421

Carslaw, H. S. and J. C. Jaeger (1959), *Conduction of Heat in Solids, 2nd ed.*, Oxford Univ. Press, New York.

Cassar, C., M. Nicolas, and O. Pouliquen (2005), Submarine granular flows down inclined planes, *Phys. Fluids, 17,* 103301, doi: 10.1063/1.2069864.

Chow, V. T. (1959), *Open-Channel Hydraulics*, 680 pp., McGraw-Hill, New York.

Cody, G. D., D. J. Goldfarb, G. V. J. Storch, and A. N. Norris (1996), Particle granular temperature in gas fluidized beds, *Powder Technol., 87*, 211-232.

Cole, P. D., E. S. Calder, R. S. J. Sparks, A. B. Clarke, T. H. Druitt, S. R. Young , R. A. Herd, C. L. Harford, and G. E. Norton (2002), Deposits from dome-collapse and fountain-collapse pyroclastic flows at Soufrière Hills Volcano, Montserrat, in *The Eruption of Soufrière Hills Volcano, Montserrat, From 1995 to 1999, Mem. Geol. Soc. London, vol. 21,* edited by T. H. Druitt and B. P. Kokelaar, pp. 231-262.

Courrech du Pont, S., P. Gondret, B. Perrin, and M. Rabaud (2003), Granular avalanches in Fluids, *Phys. Rev. Lett., 90*, 044301, doi: 10.1103/PhysRevLett.90.044301.

Davidson, J. F., and D. Harrison (1971), *Fluidization*, Academic Press, New York.

Denlinger, R. P. (1987), A model for generation of ash clouds by pyroclastic flows, with application to the 1980 eruptions at Mount St. Helens, Washington, *J. Geophys. Res., 92*, 10284-10298.

Denlinger, R. P. and R. M. Iverson (2001), Flow of variably fluidized granular masses across three-dimensional terrain 2. Numerical predictions and experimental tests, *J. Geophys. Res., 106*, 553-566. doi:10.1029/2000JB900330.

Doyle, E. E., H. E. Huppert, G. Lube, H. M. Mader, and R.S.J. Sparks (2007), Static and flowing regions in granular collapses down channels: Insights from a sedimenting shallow water model, *Phys. Fluids*, *19*, 106601, doi: 10.1063/1.2773738.

Dressler, R. F. (1954), Comparison of theories and experiments for the hydraulic dam-break wave, *Int. Assoc. Sci. Hydrol., Proc. vol. 3 (38)*, pp. 319-328.

Druitt, T. H. (1998), Pyroclastic density currents, in *The physics of Explosive Volcanic Eruptions*, edited by J. S. Gilbert, and R. S. J. Sparks, *Geol. Soc. London Spec. Pub., 145*, 145-182.

Druitt, T. H., E. S. Calder, P. D. Cole, R. P. Hoblitt, S. C. Loughlin, G. E. Norton, L. J. Ritchie, R. S. J. Sparks, and B. Voight (2002), Small volume, highly mobile pyroclastic flows formed by rapid sedimentation from pyroclastic surges at Soufrière Hills Volcano, Montserrat: An important volcanic hazard, in *The Eruption of Soufrière Hills Volcano, Montserrat, From 1995 to 1999, Mem. Geol. Soc. London, vol. 21*, edited by T. H. Druitt and B. P. Kokelaar, pp. 263– 279.

Druitt, T. H., G. Avard, G. Bruni, P. Lettieri, and F. Maez (2007), Gas retention in fine-grained pyroclastic flow materials at high temperatures, *Bull. Volcanol., 69*, 881-901.

Druitt, T. H., and R.S.J. Sparks (1982), A proximal ignimbrite breccias facies on Santorini, Greece, *J. Volcanol. Geotherm. Res., 13*, 147-171.

Dufek, J., and G.W. Bergantz (2007a), Dynamics and deposits generated by the Kos Plateau Tuff eruption: Controls of basal particle loss on pyroclastic flow transport, *Geochem. Geophys. Geosyst., 8*, Q12007, doi: 10.1029/2007GC001741.

Dufek, J., and G.W. Bergantz (2007b), Suspended load and bed-load transport of particle-laden gravity currents: the role of particle-bed interaction, *Theoret. Comput. Fluid Dyn.*, doi: 10.1007/s00162-007-0041-6.

Dufek, J., J. Wexler, and M. Manga (2009), Transport capacity of pyroclastic density currents: Experiments and models of substrate-flow interaction, *J. Geophys. Res., 114*, B11203, doi: 10.1029/2008JB006216.

Duran, J. (1999), Sands, Powders and Grains: An Introduction to the Physics of Granular Materials, Springer-Verlag, New-York.

Eames, I., and M. A. Gilbertson (2000), Aerated granular flow over a horizontal rigid surface, *J. Fluid Mech., 424*, 169-195.

Einstein, A. (1906), Eine neue bestimmung der moleküldimensionen, *Ann. Phys.* 324(2), 289-306.

Fan, L. S., and C. Zhu (1998), *Principles of gas-solid flows*, Cambridge University Press, 557 pp.

Fisher, R. V. (1966), Mechanism of deposition from pyroclastic flow, *Am. J. Sci., 264*, 350-363.

Fischer, R. V. (1995), Decoupling of pyroclastic currents: hazards assessments, *J. Volcanol. Geotherm. Res., 66*, 257-263.

Forterre, Y., and O. Pouliquen (2008), Flows of dense granular media, *Ann. Rev. Fluid Mech., 40*, 1-24.

Freundt, A., and M. Bursik (1998), Pyroclastic flow transport mechanisms, in *From magma to tephra, Modelling physical processes of explosive volcanic eruptions*, edited by A. Freundt and M. Rosi, Elsevier, pp. 173-245.

Freundt, A., S. Carey and C.J.N. Wilson (2000), Ignimbrites and block-and-ash flow deposits, in *Encyclopedia of volcanoes*, edited by H. Sigurdsson et al., Academic Press, NY-London, 581-600.

Gabet, E., and S.M. Mudd (2006), The mobilization of debris flows from shallow landslides, *Geomorphology, 74*, 207-218, doi: 10.1016/j.geomorph.2005.08.013.

GDR MiDi group (2004), On dense granular flows, *Eur. Phys. J. E, 14*, 341-365.

Geldart, D. (1973), Types of gas fluidization, *Powder Technol., 7*, 285-292.

Geldart, D., and A.C.Y. Wong (1985), Fluidization of powders showing degrees of cohesiveness-II. Experiments on rates of deaeration, *Chem. Eng. Sci.*, 40, 653-661.

George, D. L. and R. M. Iverson (2011) A two-phase debris-flow model that includes coupled evolution of volume fractions, granular dilatancy, and pore-fluid pressure, in Debris-flow hazard mitigation: Mechanics, prediction and assessment, *edited by D. Genevois D. L. Hamilton and A. Prestininzi, Padua, Italy.*

Gibilaro, L. (2001), *Fluidization-dynamics*, Buttereorth-Heinemann

Gilbertson, M.A., D.E. Jessop, and A.J. Hogg (2008), The effects of gas flow on granular currents, *Phil. Trans. Roy. Soc. A, 366*, 2191-2203, doi: 10.1098/rsta.2007.0021

Girolami, L., O. Roche, T. H. Druitt, and T. Corpetti (2010), Velocity fields and depositional processes in laboratory ash flows, *Bull. Volcanol.*, in press.

Girolami, L., T. H. Druitt, O. Roche, and Z. Khrabrykh (2008), Propagation and hindered settling of laboratory ash flows, *J. Geophys. Res., 113*, B02202, doi:10.1029/2007JB005074.

Graf, W. H., and M. S. Altinakar (2000), *Hydraulique fluviale*, Presses polytechniques et universitaires romandes, Lausanne, 627 pp.

Goldhirsch, I. (2003), Rapid granular flows, *Annu. Rev. Fluid Mech, 22*, 267 - 293, doi:10.1146/annurev.fluid.35.101101.161114

Goren, L., E. Aharonov, D. Sparks and R. Toussaint (2010), Pore pressure evolution in deforming granular material: a general formulation and the infinitely stiff approximation, *J. Geophys. Res. 115*, B09216, doi:10.1029/2009JB007191.

Goren, L., E. Aharonov, D. Sparks and R. Toussaint (2011), The mechanical coupling of fluid-filled granular material under shear, *Pure Appl. Geophys. 168*, 2289–2323, doi:10.1007/s00024-011-0320-4

Hauser, A. 2002. Rock avalanche and Resulting Debris Flow in Estero Parraguirre and Río Colorado, Región Metropolitana, Chile, in *J. Catastrophic landslides: Effects, occurrence, and mechanisms*, edited by S. Evans and DeGraff, Geological Society of America Reviews in Engineering Geology, V. XV, 135-148.

Hogg, A. J., and D. Pritchard (2004), The effects of hydraulic resistance on dam-break and other shallow inertial flows, *J. Fluid Mech., 501*, 179-212.

Hogg, A. J., and A. W. Woods (2001), The transition from inertia- to bottom drag-dominated motion of turbulent gravity currents, *J. Fluid Mech.*, *449*, 201-224.

Hopfinger, E.J. (1983), Snow avalanche motion and related phenomena, *Ann. Rev. Fluid Mech.*, *15*, 47-76.

Huang, Q., H. Zhang, and J. Zhu (2009), Experimental study on fluidization of fine powders in rotating drums with various wall friction and baffled rotating drums, *Chem. Eng. Sci.*, *64*, 2234-2244, doi: 10.1016/j.ces.2009.01.047.

Hummel, N. (2008), Modelling and interpretation of microseismic signatures related to nonlinear pore pressure diffusion in porous media, Diploma thesis, Geophysikalisches Institut Universität Karlsruhe (TH), Karlsruhe, Germany.

Hungr, O., G. C. Morgan and R. Kellerhals (1984), Quantitative analysis of debris torrents hazards for design of remedial measures, *Can. Geothecnical J*., 21, 663 – 667.

Hunt, M. L., R. Zenit, C. S. Campbell, and C. E. Brennen (2002), Revisiting the 1954 suspension experiments of R. A. Bagnold, *J. Fluid Mech.*, *452*, 1-24.

Huppert, H. E. (2006), Gravity currents: a personal perspective, *J. Fluid Mech.*, *554*, 299-322.

Hutchinson, J.N. (1986), A sliding-consolidation model for flow slides, *Can. Geotech. J.*, *23*, 115-126, doi: 10.1139/t86-021.

Hutter, K., Y. Wang and S. P. Pudasaini. (2005), The Savage-Hutter avalanche model: how far can it be pushed?. *Philos. Trans. R. Soc. London, Ser. A. 363*, 1507-1528. doi:10.1098/rsta.2005.1594

Ilstad, T., J.G. Marr, A. Elverhøi, and C.A. Harbitz (2004), Laboratory studies of subaqueous debris flows by measurements of pore-fluid pressure and total stress, *Marine Geol.*, *213*, 403-414, doi: 10.1016/j.margeo.2004.10.016.

Ishida, M., H. Hatano and T. Shirai (1980), The flow of solid particles in an aerated inclined channel, *Powder Technol.*, *27*, 7-12.

Iverson, R. M. (1997), The physics of debris flows, *Rev. Geophys.*, *35*, 245-296.

Iverson, R. M. (2000), Landslide triggering by rain infiltration, *Water Resour. Res. 36*, 1897-1910. doi:10.1029/2000WR900090

Iverson, R.M. (2005), Regulation of landslide motion by dilatancy and pore pressure feedback, *J. Geophys. Res.*, *110*, F02015, doi: 10.1029/2004JF000268.

Iverson, R. M. and R. G. LaHusen (1989), Dynamic pore-pressure fluctuations in rapidly shearing granular materials, *Science*, *246*, 796-799.

Iverson, R.M., and R.P. Denlinger (2001), Flow of variably fluidized granular masses across three-dimensional terrain 1. Coulomb mixture theory, *J. Geophys. Res.*, *106*, 537-552.

Iverson, R. M., M. Logan and R. P. Denlinger (2004), Granular avalanches across irregular three-dimensional terrain: 2. Experimental tests, *J. Geophys. Res.*, *109*, F01015, doi:10.1029/2003JF000084.

Iverson, R. M., M. E. Reid and R. G. LaHusen (1997), Debris-flow mobilization from landslides, *Annu. Rev. Earth Planet. Sci.*, *25*, 85–138, doi:10.1146/annurev.earth.25.1.85.

Iverson, R.M., M.E. Reid, N.R. Iverson, R.G. LaHusen, M. Logan, J.E. Mann, and D.L. Brien (2000), Acute sensitivity of landslide rates to initial soil porosity, *Science*, *290*, 513-516.

Iverson, R.M., M.E. Reid, and R.G. LaHusen (1997), Debris-flow mobilization from landslides, *Ann. Rev. Earth Planet. Sci.*, *25*, 85-138.

Iverson, R. M., M. Logan, R. G. LaHusen and M. Berti, (2010), The perfect debris flow? Aggregated results from 28 large-scale experiments: *J. Geophys. Res., v. 115*, F03005, doi: 10.1029/2009JF001514.

Jain, N., J. M. Ottino and R. M. Lueptow (2004), Effect of interstitial fluid on granular flowing layer. *J. Fluid. Mech. 508*, 23-44, doi: 10.1017/S0022112004008869.

Jánosi, I. M., D. Jan, K. G. Szabó, and T. Tél (2004), Turbulent drag reduction in dam-break flows, *Experim. Fluids*, *37*, 219-229.

Johnson, P.C., and R. Jackson (1987), Frictional-collisional constitutive relations for granular materials, with application to plane shearing, *J. Fluid Mech.*, *176*, 67-93.

Johnson, P.C., P. Nott, and R. Jackson (1990), Frictional-collisional equations of motion for particulate flows and their application to chutes, *J. Fluid Mech.*, 210, 501-535.

Jop, P., Y. Forterre, and O. Pouliquen (2006), A constitutive law for dense granular flows, *Nature*, *441*, 727-730.

Kelfoun, K., P. Palacio, D. Barba, and P. Samaniego (2007), Pyroclastic flow simulation and frictional behavior: confrontation with a well constrained eruption at Tungurahua volcano (Ecuador), *Bull. Volcanol.*, in press.

Kerswell, R. R. (2005), Dam break with Coulomb friction: a model for granular slumping ?, *Phys. Fluids*, *17*, 057101, doi: 10.1063/1.1870592.

Krieger, I. M. and T. J. Dougherty (1959), A mechanism for non-Newtonian flow in suspensions of rigid particles, *Trans. Soc. Rheol* 3, 137.

Lajeunesse, E., J. B. Monnier, and G. M. Homsy (2005), Granular slumping on a horizontal surface, *Phys. Fluids*, *17*, 103302, doi: 10.1063/1.2087687.

Larrieu, E., L. Staron, and E. J. Hinch (2006), Raining into shallow water as a description of the collapse of a column of grains, J. *Fluid Mech.*, *554*, 259-270.

Lauber, G., and W. H. Hager (1998), Experiments to dam break wave: horizontal channel, *J. Hydraul. Res.*, *36*, 291-307.

Leal, J. G. A. B., R. M. L. Ferreira, and A. H. Cardoso (2006), Dam-break wave-front celerity, *J. Hydraul. Eng.*, *132*, 69-76.

Levine, A. H., and S.W. Kieffer (1991), Hydraulics of the August 7, 1980, pyroclastic flow at Mount St. Helens, Washington, *Geology*, *19*, 1121-1124.

Liang, Y., J. D. Price, D. A. Wark and E. B. Watson (2001), Nonlinear pressure diffusion in a porous medium: Approximate solutions with applications to permeability measurements using transient pulse decay method, *J. Geophys. Res*., *106*, 529– 535, doi: 10.1029/2000JB900344-

Lorences, M. J., G. S. Patience, F. V. Díez and J. Coca (2003), Fines effects on collapsing fluidized beds, *Powder Technol*., *131*, 234-240, doi:10.1016/S0032-5910(03)00004-4.

Lube, G., H. E. Huppert, R. S. J. Sparks, and M. A. Hallworth (2004), Axisymmetric collapses of granular columns, *J. Fluid Mech.*, *508*, 175-199.

Lube, G., H. E. Huppert, R. S. J. Sparks, and A. Freundt (2005), Collapses of two-dimensional granular columns, *Phys. Rev. E*, *72*, 041301, doi: 10.1103/PhysRevE.72.041301.

Lucas, A., A. Mangeney (2007), Mobility and topographic effects for large Valles Marineris landslides on Mars. *Geophys. Res. Lett*. 34, L10201. doi:10.1029/2007GL029835.

Major, J.J. (2000), Gravity-driven consolidation of granular slurries - implications for debris-flow deposition and deposit characteristics, J. Sedim Res., *70*, 64-83.

Major, J.J., and R.M. Iverson (1999), Debris-flow deposition: effects of pore-fluid pressure and friction concentrated at flow margins, *Geol. Soc. Am. Bull.*, *111*, 1424-1434.

Major, J. J., R.M. Iverosn, D. F. McTigue, S. Macias and B.K. Fiedorowicz (1997), Geotechnical properties of debris-flow sediments and slurries, *in Debris-Flow Hazards Mitigation: Mechanics, Prediction, and Assessment*: American Society of Civil Engineers, Proceedings of First International Conference, August 7–9, San Francisco, California, p. 249–259.

Mangeney, A., F. Bouchut, N. Thomas, J.-P. Vilotte, and M. O. Bristeau (2007), Numerical modeling of self-channeling granular flows and their levée-channel deposits, *J. Geophys. Res.*, *112*, F02017, doi: 10.1029/2006JF000469.

McArdell, B.W., P. Bartelt, and J. Kowalski (2007), Field observations of basal forces and fluid pore pressure in a debris flow, *Geophys. Res. Lett.*, *34*, L07406, doi: 10.1029/2006GL029183.
McClung D. and P. Schaerer (1993), *The avalanche handbook*, The Mountaineers.
McElwaine, J.N., and K. Nishimura (2001), Ping-pong ball avalanche experiments, *Spec. Pub. Int. Assoc. Sedim.*, *31*, 135-148.
McElwaine, J.N. (2005), Rotational flow in gravity current heads, *Phil. Trans. Roy. Soc. A*, *363*, 1603-1623, doi: 10.1098/rsta.2005.1597.
McElwaine, J.N., and B. Turnbull (2005), Air pressure data from the Vallée de la Sionne avalanches of 2004, *J. Geophys. Res.*, *110*, F03010, doi: 10.1029/2004JF000237.
McEwen, A. S., and M. C. Malin (1989), Dynamics of Mount St. Helens' 1980 pyroclastic flows, rockslide-avalanche, lahars, and blast, *J. Volcanol. Geotherm. Res.*, *37*, 205-231.
Meruane C., A. Tamburrino, and O. Roche (2010), On the role of the ambient fluid on gravitational granular flow dynamics, *J. Fluid Mech.*, in press.
Montgomery, D.R., K.M. Schmidt, W.E. Dietrich, and J. McKean (2009), Instrumental record of debris flow initiation during natural rainfall: Implications for modeling slope stability, *J. Geophys. Res.*, *114*, F01031, doi: 10.1029/2008JF001078.

Montserrat, S., A. Tamburrino, Y. Niño, and O. Roche (2007), Kinematics and pore pressure dynamics in aerated granular flows, *Proc. 32nd Int. Assoc. Hydraulic Res. Congress*.
Naef, D., D. Rickenmann, P. Rutschmann, and B.W. McArdell (2006), Comparison of flow resistance relations for debris flows using a one-dimensional finite element simulation model, *Nat. Haz. Earth Syst. Sci.*, *6*, 155-165.
Neri, A., T. Esposti Ongaro, G. Menconi, M. De Michieli Vitturi, C. Cavazzoni, G. Erbacci, and P. J. Baxter (2007), 4D simulation of explosive eruption dynamics at Vesuvius, *Geophys. Res. Lett.*, *34*, L04309, doi:10.1029/2006GL028597.
Nishimura, K., F. Sandersen, K. Kristensen, and K. Lied (1995), Measurements of powder snow avalanche, *Surv. Geophys.*, *16*, 649-660.
Okada, Y., and H. Ochiai (2008), Flow characteristics of 2-phase granular mass flows from model flume tests, *Eng. Geol.*, *97*, 1-14, doi: 10.1016/j.enggeo.2007.10.004.
Okada, Y., K. Sassa, and H. Fukuoka (2004), Excess pore pressure and grain crushing of sands by means of undrained and naturally drained ring-shear tests, *Eng. Geol.*, *75*, 325-343, doi: 10.1016/j.enggeo.2004.07.001.
Okura, Y., H. Kitahara, H. Ochiai, T. Sammori, and A. Kawanami (2002), Landslide fluidization process by flume experiments, *Eng. Geol.*, *66*, 65-78.
Patankar, S. (1980), *Numerical Heat Transfer and Fluid Flow*, Hemisphere Publishing Corporation.
Pittari, A., and R.A.F. Cas (2004), Sole marks at the base of the late Pleistocene Abrigo Ignimbrite, Tenerife: implications for transport and depositional processes at the base of pyroclastic flows, *Bull. Volcanol.*, *66*, 356-363, doi: 10.1007/s00445-003-0317-7.
Pouliquen, O. (1999), Scaling laws in granular flows down rough inclined planes, *Phys. Fluids*, *11*, 542-548.
Pudasaini, S. P., Y. Wang and K. Hutter (2005), Modeling debris flows down general channels. *Nat. Hazards Earth Syst. Sci.*, *5*, 799-819, doi:10.5194/nhess-5-799-2005
Rastello, M., and E.J. Hopfinger (2004), Sediment-entraining suspension clouds: a model of powder-snow avalanches, *J. Fluid Mech.*, *509*, 181-206.
Richardson J. F. and W. N. Zaki (1954) Sedimentation and fluidization: part I. *Trans. Inst. Chem. Eng. 32*, 35–52
Rhodes, M. J. (1998), *Introduction to Particle Technology*, John Wiley and Sons, Chichester.

Richard, P., M. Nicodemi, R. Delannay, P. Ribiиre, and D. Bideau (2005), Slow relaxation and compaction of granular systems, *Nat. Mater.* 4(2), 121-128.

Rickenmann, D. (1999), Empirical relationships for debris flows, *Nat. Hazards*, 19, 47-77.

Ritter, A. (1892), Die Fortpflanzung der Wasserwellen. *Z. Vereines Deutsch. Ing.*, *36*, 947–954.

Roche, O. (2012), Depositional processes and gas pore pressure in pyroclastic flows: an experimental perspective, *Bull Volcanol*, in press, doi:10.1007/s00445-012-0639-4

Roche, O., M. Gilbertson, J. C. Phillips, and R. S. J. Sparks (2002), Experiments on deaerating granular flows and implications for pyroclastic flow mobility, *Geophys. Res. Lett.*, *29*(*16*), doi: 10.1029/2002GL014819.

Roche, O., M. Gilbertson, J. C. Phillips, and R. S. J. Sparks (2004), Experimental study of gas-fluidized granular flows with implications for pyroclastic flow emplacement, *J. Geophys. Res.*, *109*, B10201, doi: 10.1029/2003JB002916.

Roche, O., M. A. Gilbertson, J. C. Phillips, and R. S. J. Sparks (2005), Inviscid behavior of fines-rich pyroclastic flows inferred from experiments on gas-particle mixtures, *Earth Planet. Sci. Lett.*, *240*, 401-414.

Roche, O., M. Attali, A. Mangeney and A. Lucas (2011), On the run-out distance of geophysical gravitational flows: Insight from fluidized granular collapse experiments, *Earth Planet. Sci. Lett.*, *311*, 375-385, doi:10.1016/j.epsl.2011.09.023

Roche, O., S. Montserrat, Y. Niño, and A. Tamburrino (2008), Experimental observations of water-like behavior of initially fluidized, dam break granular flows and their relevance for the propagation of ash-rich pyroclastic flows, *J. Geophys. Res.*, *113*, B12203, doi: 10.1029/2008JB005664.

Roche, O., S. Montserrat, Y. Niño and A. Tamburrino (2010), Pore fluid pressure and internal kinematics of gravitational laboratory air-particle flows: insights into the emplacement dynamics of pyroclastic flows, *J. Geophys. Res*, *115*, B09206, doi:10.1029/2009JB007133.

Salm, B. (1993), Flow, flow transition and runout distances of flowing avalanches, *Annals Glaciol.*, *18*, p. 221-226.

Saucedo, R., J. L. Macias, M. F. Sheridan, M. I. Bursik, J. C. Komorowski (2005), Modeling of pyroclastic flows of Colima Volcano, Mexico: implications for hazard assessment, *J. Volcanol. Geotherm. Res.*, *139*,103–115.

Savage, S. B. (1984), The mechanics of rapid granular flows, *Adv. Applied Mech.*, *24*, 289-366.

Savage, S. B., and K. Hutter (1989), The motion of a finite mass of granular material down a rough incline, *J. Fluid Mech.*, *199*, 177-215.

Savage, S. B. and R. M. Iverson (2003), Surge dynamics coupled to pore-pressure evolution in debris flows, in *Debris-flow hazard mitigation: Mechanics, prediction and assessment*, edited by D. Rickenman and C. L. Chen, Millpress *Rotterdam*, ISBN 90 7701778X.

Sheridan, M. F., A. J. Stinton, A. Patra, E. B. Pitman, A. Bauer, and C. C. Nichita (2005), Evaluating Titan2D mass-flow model using the 1963 Little Tahoma Peak avalanches, Mount Rainier, Washington, *J. Volcanol. Geotherm. Res.*, *139*, 89-102.

Snieder, R., and A. van den Beukel (2004), The liquefaction cycle and the role of drainage in liquefaction, *Gran. Matt.*, *6*, 1-9, doi: 10.1007/s10035-003-0151-9.

Sparks, R. S. J. (1976), Grain size variations in ignimbrites and implications for the transport of pyroclastic flows, *Sedimentology*, *23*, 147–188.

Sparks, R. S. J. (1978), Gas release rates from pyroclastic flows: a assessment of the role of fluidisation in their emplacement, *Bull. Volcanol.*, *41*, 1-9.

Sparks, R. S. J., and L. Wilson (1976), A model for the formation of ignimbrite by gravitational column collapse, *J. Geol. Soc. London*, *132*, 441–451.

Sparks, R.S.J., M.C. Gardeweg, E.S. Calder, and S.J. Matthews (1997), Erosion by pyroclastic flows on Lascar Volcano, Chile, *Bull. Volcanol.*, *58*, 557-565.

Suzuki-Kamata, K. (1988), The ground layer of Ata pyroclastic flow deposit, southwestern Japan - evidence for the capture of lithic fragments, *Bull. Volcanol., 50*, 119-129.

Takahashi, T., and H. Tsujimoto (2000), A mechanical model for Merapi-type pyroclastic flow, *J. Volcanol. Geotherm. Res., 98*, 91–115.

Turnbull, B., and J.N. McElwaine (2007), A comparison of powder snow avalanches at Vallée de la Sionne with plume theories, *J. Glaciol.*, *53*, 30-40.

Turnbull, B., and J.N. McElwaine (2008), Experiments on the non-Boussinesq flow of self-igniting suspension currents on a steep open slope, *J. Geophys. Res.*, *113*, F01003, doi: 10.1029/2007JF000753.

Turnbull, B., and J.N. McElwaine (2009), Potential flow models of suspension current air pressure, *Annals Glaciol.*, in press.

Valentine, G.A., and K. H., Wohletz (1989), Environmental hazards of pyroclastic flows determined by numerical models, *Geology*, *17*, 641–644.

Versteg, H. and W. Malalasekera (1995), *An introduction to computational fluid dynamics*. *The finite volume method*, Longman Group. Ltd.

Vollmöller, P. (2004), A shock-capturing wave-propagation method for dry and saturated granular flows. *J. Comput. Phys. 199*, 150–174, doi:10.1016/j.jcp.2004.02.008

Wadge, G., P. Jackson, and S. M. Bower (1998), Computer simulations of pyroclastic flows from dome collapse, *Geophys. Res. Lett.*, *25* (19), 3677–3680.

Whitham, G. B. (1955), The effects of hydraulic resistance in the dam-break problem, *Proc. Roy. Soc. London. Ser. A, Mathematical and Physical Sciences*, *227*, 399-407.

White, F.M. (2003), *Fluid Mechanics*, 5th edition, McGraw-Hill, 866 pp.

Wilson, C. J. N. (1980), The role of fluidization in the emplacement of pyroclastic flows: an experimental approach, *J. Volcanol. Geotherm. Res.*, *8*, 231-249.

Wilson, C. J. N. (1984), The role of fluidization in the emplacement of pyroclastic flows, 2: experimental results and their interpretation, *J. Volcanol. Geotherm. Res.*, *20*, 55-84.

Wilson, C. J. N. (1986), Pyroclastic flows and ignimbrites, *Sci. Prog. Oxf.*, *70*, 171-207.

Wilson, L. and J. W. Head (1981) Morphology and rheology of pyroclastic flows and their deposits, and guidelines for future observations, *in The 1980 eruptions of Mount St Helens, Washington*, edited by P. W. Lipmanm and D. R. Mullineaux, US. Geol. Surv., Prof Paper 1250, 513-524.

Yilmaz, O., R. C. Nolen-Hoeksema and A. Nur (1994), Pore pressure profiles in fractured and compliant rocks, *Geophys. Prospect.*, *42*, 693-714, doi:10.1111/j.1365-2478.1994.tb00236.x

Zenit, R. (2005), Computer simulations of the collapse of a granular column, *Phys. Fluids*, *17*, 031703, doi:10.1063/1.1862240.